Magnetic fine structure in the solar photosphere: observations and MHD simulations

Dissertation
zur Erlangung des Doktorgrades
der Mathematisch-Naturwissenschaftlichen Fakultäten
der Georg-August-Universität zu Göttingen

vorgelegt von
Sanja Danilović
aus Ivanjica/Serbien

Göttingen 2009

Bibliografische Information der Deutschen Nationalbibliothek

Die Deutsche Nationalbibliothek verzeichnet diese Publikation in der Deutschen Nationalbibliografie; detaillierte bibliografische Daten sind im Internet über `http://dnb.d-nb.de` abrufbar.

D7
Referent: Prof. Dr. Franz Kneer
Korreferent: Prof. Dr. Sami K. Solanki
Tag der mündlichen Prüfung: 4 Juli 2009

ISBN 978-3-942171-34-2

uni-edition GmbH 2010
http://www.uni-edition.de

Printed in Germany

Contents

Summary

The fine structure of the magnetic field in the solar photosphere is the result of the complex interactions between the magnetic field and convection. Although the spatial resolution of the instruments used in the study of the photospheric magnetic field has improved significantly, a sizeable fraction of the magnetic features remain unresolved even in observations with the currently highest resolution. Magnetohydrodynamic numerical models of the solar surface layers can provide insight into the processes that take place at length scales and depths not accessible to observations. Owing to the integration of the necessary physical mechanisms in the models, they have reached a level of realism and accuracy that enables a quantitative comparison with observations. In this thesis, the spectropolarimetric signals synthesized from 3D radiative magneto-hydrodynamic simulations are compared with observational data obtained with the Spectropolarimeter (SP) onboard *Hinode* satellite. Questions related to the characteristics of the granulation and the internetwork magnetic field are addressed.

- The consistency of the synthesized and observed granulation contrast is verified. The true contrast of solar granulation is determined to be 14-15% at 630 nm. The theoretical point spread function (PSF) for the Hinode/SP instrument is obtained through forward modelling. The PSF takes into account the effects of the optical system and a slight defocus of the observed images.

- The origin of the magnetic field and the amount of the flux present in the quiet Sun is considered. Particular emphasis is placed on the role of surface dynamo action. For this, simulation runs with different magnetic Reynolds numbers (R_m) are used and compared with observations at different heliocentric angles and with different levels of noise. It is found that the average field strength distribution of a run with higher R_m can be reproduced by scaling the results from the run with lower R_m. Taking into account this property of the dynamo simulations, an extrapolation is performed which allows the observational data to be quantitatively reproduced. As a result, the mean magnetic flux density is obtained. At the optical depth $\tau_{630} = 1$ level, the mean field strength implied by our analysis is about 170 G, which drops to 70 G at $\tau_{630} = 0.1$.

- Recent Hinode/SP observations indicate a magnetic field intensification coupled with the appearance of bright points in continuum intensity maps at locations where strong downflows are seen. A comparison between the magnetic field intensification in numerical simulations and the observational results is made. Three cases of magnetic field intensification are presented in detail. The differences in their

observational signatures are discussed. One of the events agrees very well with observation performed by Hinode/SP.

- Magnetic reconnection is an important source of thermal and kinetic energy input into the solar atmosphere. In order to extract the observable features of the process, an example of flux cancellation and magnetic reconnection in the upper photosphere, found in the 3D MHD simulations, is presented in detail. The signatures of magnetic reconnection in Fe I 630.1 nm and 630.2 nm and Fe II 5197.58 Å and 4923.92 Å lines are computed. The relatively subtle variations of the polarization signals in the Fe I 630.1 nm and 630.2 nm lines, mainly due to the changes of magnetic field polarity along the line of sight are not resolvable by Hinode/SP. However, the much stronger signature in Fe II lines, produced by the temperature increase and strong downflow in the regions where magnetic energy dissipates, could be detectable with current instruments.

1 Introduction

The Sun shows radiative output variability on a wide range of temporal and spatial scales. While variations on time scales of minutes to hours are due to solar oscillations and granulation, variations on longer time scales are driven by the evolution of the magnetic field. The radiative energy output of the Sun is modulated in phase with the solar cycle. The change is particularly high in UV, EUV and radio wavelengths. It covers a range from a factor of 2 to 10 between the solar activity minimum and maximum. The soft X-ray flux changes by a factor of order 100 (Solanki et al. 2006). The total solar irradiance[1] (TSI) shows the change of the order of 0.1% in phase with the solar cycle. The increase in TSI during the solar activity maximum is the result of the presence of the bright magnetic field elements that cover much larger fraction of the solar surface than dark sunspots. Models that take into account the evolution the magnetic field in the solar photosphere are able to reproduce the observed TSI changes on scales from days to the period of the solar cycle (Wenzler et al. 2005, 2006). The same is true for the solar irradiance at different wavelength ranges (Krivova et al. (2003, 2006), Unruh et al. (2008), see also the Appendix).

1.1 Photospheric magnetic field

The structure of the magnetic field in the solar photosphere and the physical processes that occur within are a result of "magneto-convection" - the interaction of convective flows with the magnetic field embedded in the plasma. Depending on the amount of magnetic flux per unit area, different regimes of magnetoconvetion can be distinguished. These regimes can be associated to the different regions on the solar surface (Fig. 1.1).

Regions with the smallest magnetic flux per unit area are known as the *internetwork*. The magnetic field is organized in intermittent structures. It is carried by the convective flows and concentrated in the downflow regions between the convection cells. This process is called flux expulsion (Parker 1963, Weiss 1966). The strength of the magnetic field accumulated in this way is of the order of a few hundred Gauss. Flows are able to compress the field so that the magnetic energy density $B^2/8\pi$ approaches the kinetic energy density $\rho v^2/2$ of the flow. One of the mechanisms responsible for the further intensification to kG is referred to as convective intensification (Grossmann-Doerth et al. 1998). It occurs due to the presence of magnetic field, which reduces heat transport by convection. The material inside the flux concentration radiates more than it receives, cools down and starts to sink. In order to maintain total pressure equilibrium, the reduced gas

[1]The total solar irradiance is the total amount of solar energy integrated over all wavelengths received at the top of the Earth's atmosphere per unit time and area.

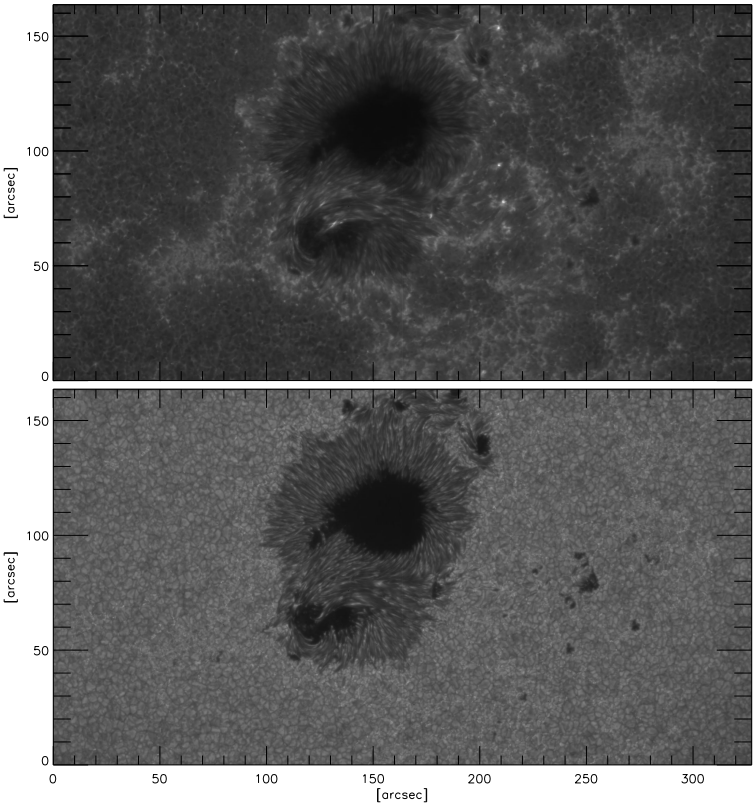

Figure 1.1: Different regimes of magnetoconvetion. G band (lower panel) and Ca II H (upper panel) filtergrams taken with Broadband Filter Imager onboard Hinode satellite.

pressure inside the flux concentration is compensated by enhanced magnetic pressure due to contraction of the magnetic concentration.

The mechanism that amplifies, but also generates the magnetic field is the surface dynamo (Petrovay & Szakaly 1993, Cattaneo 1999, Vögler & Schüssler 2007). The estimated orders of magnitude of the kinetic and magnetic Reynolds numbers [2] in the solar surface layers indicate that this mechanism may be at work. Due to the high value of R_e, the flow in the solar convection zone is turbulent, and the same holds for the magnetic field since R_m is high. Random stretching of magnetic field lines by turbulent motions amplifies the magnetic energy (Batchelor 1950). When R_m exceeds a critical threshold, $R_m > R_m^C$, stretching dominates over dissipation and dynamo action occurs. The contribution of this process to quiet Sun magnetism is still a matter of debate as will be explained in the next section.

Once kG magnetic concentrations are formed they may appear bright (photospheric bright points) or dark (pore) in the continuum intensity. It depends on whether the vertical cooling is compensated or not by the lateral heating due to horizontal radiative exchange (Spruit 1976, Bercik et al. 2003, Vögler et al. 2005). The formed magnetic concentrations are mostly vertically oriented because of the buoyancy force that results from the density deficit within the concentration. Owing to back-reaction of Lorentz force, the kG magnetic concentration are less susceptible to the bending or distortion by the convective flows. However, they can be transported horizontally by the flow (to some degree similar to a solid body immersed in a fluid) and organized into the *network* on the mesogranular (5" – 10") and supergranular scales (20" – 40") (Simon & Leighton 1964, Berger et al. 1998).

It has been suggested that the magnetic concentrations decay through the process of the interchange instability (Parker 1975). As a result of the perturbation by the surrounding granules, the concentration is deformed until the point of fragmentation. The smaller fragments are then prone to faster dispersal. Another way of decay is through cancellation with a magnetic element of opposite polarity. When cancellation occurs the magnetic field lines are reconnected which is accompanied by the energy release appearing e.g. in the form of small flare-like brightening seen in extreme ultraviolet images (Innes et al. 2009).

The next regime of the magneto-convection is related to *facular/plage* regions. With the higher average magnetic field strength, the properties of convection are strongly affected by the magnetic field. The granulation becomes "abnormal" (Dunn & Zirker 1973), with smaller granules that have longer lifetimes than in the quiet Sun (Title et al. 1989). The flux concentrations are organized in thin, bright ribbons ("filigree" in H_α). The downflow is suppressed within these features (Solanki 1986), as reproduced by numerical simulation (Vögler et al. 2005) and the brightness is a consequence of the lateral inflow of radiative flux as mentioned previously.

At the top of the hierarchy of the photospheric structures are the *sunspots* with the

[2]The kinetic and magnetic Reynolds numbers are dimensionless parameters characterizing convection and dynamo action. The magnetic Reynolds number is defined as $R_m = UL/\eta$ (U and L are typical velocity and length scales and η the magnetic diffusivity). It gives the relative strengths of advection over diffusion. Similarly, the kinetic Reynolds number is $R_e = UL/\nu$ where ν is the kinematic viscosity. They are of order of $R_m = 10^6$ and $R_e = 10^{12}$ near the solar surface (Ossendrijver 2003).

highest magnetic flux per unit surface. Since they follow Hale's polarity law [3] and Joy's law [4] and their origin is connected to the global dynamo (Ossendrijver 2003). The fine surface structure of the sunspots, on the other hand, seems to be a result of magneto-convection (Schüssler & Vögler 2006, Rempel et al. 2009). In sunspot umbrae, the convection is strongly modified by the presence of the magnetic field and its efficiency to transport energy significantly reduced. Owing to the strong external magnetic field, the convective cells have a form of small narrow upflowing plumes. As they reach the surface layers, they create a "gap" in the magnetic field at the surface. As a result of the plasma expanding and piling up at the solar surface, cusplike configurations outlined by a dark lane appear in the brightness images. They correspond to the observed bright umbral dots. A similar explanation is given for the bright filaments in the sunspot penumbrae. In this case, the upflowing plumes become elongated because of the presence of an inclined magnetic field which deflects the upflow in the outward direction.

1.2 The internetwork field

Magnetic signatures in the interior of supergranular cells were first found by Livingston & Harvey (1971). Since then, the magnetic field found in the quiet sun has been divided into the network and internetwork field. Although instruments that offer higher sensitivity and spatial resolution appeared in the meantime, the nature of the internetwork field is still uncertain. The main questions are: (1) how much magnetic flux is contained in the internetwork, (2) is the field intrinsically weak or strong there and (3) what is its origin?

There are several suggestions about the origin of the internetwork field. One is that the internetwork field is the remnant of pre-existing bipolar magnetic regions produced by the global solar dynamo. This would imply that internetwork would show some signed magnetic flux, but observations do not support this (Khomenko et al. 2003, 2005a). Also, the fact that quiet Sun fields do not seem to vary as much as the active regions during the solar cycle (Trujillo Bueno et al. 2004) is an argument against this proposal. On the other hand, the magnetic flux from the decaying regions which gets dragged down by the convection may emerge again. Such an effect has been identified in MHD simulations carried out by Ploner et al. (2001), suggesting that such recycling may take place. Also, the emergence of the field generated in the deeper layers may contribute to the internetwork field. This suggestion is supported by the work by Harvey (1993) and Hagenaar (2001) who showed that the emergence frequency of bipolar regions on the solar surface strongly increases with decreasing flux per region, a trend that is independent of the phase of the cycle. The smallest of the bipolar regions tend not to follow Hale's polarity law, but seem to emerge randomly oriented. Finally, the surface dynamo mentioned in the previous section could also be the mechanism responsible for the existence of the internetwork field.

There are several techniques with which the magnetic field in the quiet Sun has been studied. "Proxy-magnetometry" is one of them. It relies on the signature that the magnetic

[3] Hale's polarity law says that sunspots appear in the bipolar pairs with opposite east-west orientations of polarity in the northern and southern hemisphere. The east-west orientation of sunspot pairs reverses in both hemisphere during the minimum of the 11-year sunspot number cycle.

[4] The axis of a sunspot pair is tilted with respect to east-west direction, with the leading spot being closer to the equator.

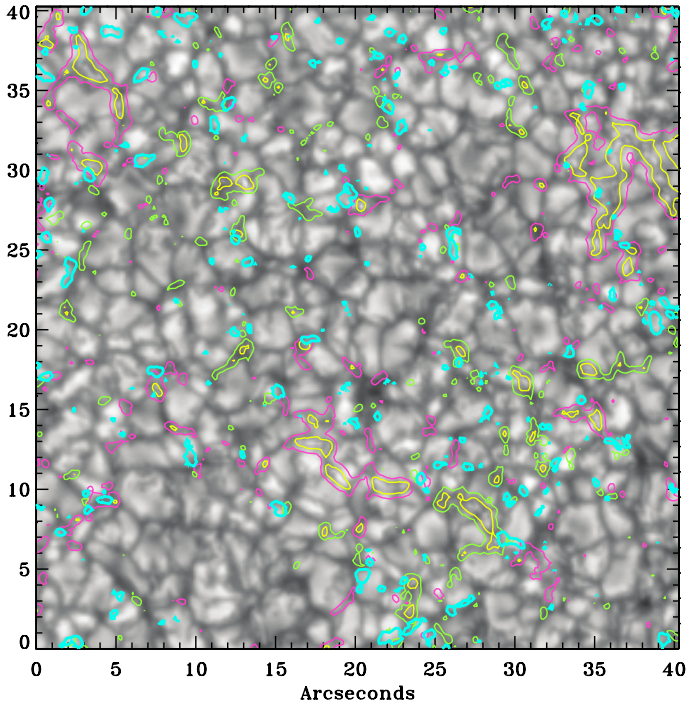

Figure 1.2: Continuum intensity with contours of apparent magnetic flux density superimposed. Red and green contours show, respectively, the positive and negative vertical field. Yellow contours are for strong vertical field elements. Blue contours mark the position of the horizontal field (from Lites et al. (2008)).

field leaves in intensity maps. The most often used diagnostic is the Fraunhofer G band around 430.8 nm, which is dominated by CH molecular lines. The brightening in the intensity maps is caused by a depletion of CH molecules in the radiatively heated magnetic flux concentrations (Schüssler et al. 2003). Thus, the kG field is required to form a bright point, but it is not a sufficient condition (Berger & Title 2001, Ishikawa et al. 2007). Extensive research has been done regarding the characteristics and dynamic of these bright points (de Wijn et al. 2009). The disadvantage of proxy-magnetometry methods is that the features observed are 'unstable' - they live shorter than the associated field. Also, they give an information just on kG fields (and only qualitatively), so the existence of sub-kG fields would be missed.

The standard diagnostic tool used in the study of the magnetic field relies on its effect on the polarization state of solar radiation, via Zeeman and Hanle effects. The two effects are complementary. The Zeeman effect provides information on both, strong and weak magnetic field, as well as its orientation, but it suffers from the cancellation effect if

magnetic elements with opposite polarities reside in the resolution element. The Hanle effect, on the other hand, is sensitive only to low field strengths, but it can be used to measure the hidden field (turbulent field), i.e. the field tangled on the spatial scales smaller than the resolution element.

The results based on the Hanle effect depend on the adopted distribution of angle and field strength and on the definition of the reference (zero field) case (Trujillo Bueno et al. 2006). The mean magnetic field strength retrieved from the Hanle-based measurements range from roughly 10 G to 60 G (de Wijn et al. 2009). The zero-field reference case depends on the model atmosphere and on the free parameters used, such as microturbulent and macroturbulent velocities, collision rates, etc. This can lead to underestimation of the zero-field scattering polarization amplitudes and to lower values of the mean magnetic field strength obtained in this way. By using more than one spectral line, the defining the zero-field reference case can be circumvented (Stenflo et al. 1998). The other way to solve the problem is to perform 3D radiative transfer calculations in realistic model atmospheres from numerical simulations (Trujillo Bueno et al. 2004). Then, the remaining input needed is the field distribution. In order to fit the observed polarization amplitude of the Sr I 4607 Å line Trujillo Bueno et al. (2004) assumed several field distributions. Using a single-value isotropic microturbulent field distribution they inferred that the mean strength of the internetwork field is $\langle B \rangle \approx 60$ G. On the other hand, by assuming an exponential probability distribution function (PDF) for the field strength suggested by the results of numerical simulation (Cattaneo 1999, Vögler et al. 2005), they obtained $\langle B \rangle \approx 130$ G.

In the case of the Zeeman effect studies, most of the recent results have been obtained using the spectral lines of Fe I at 630 nm and 1.56 μm. The results appear contradictory. The infrared Fe I lines at 1.56 μm reveal mostly weak fields with an exponential distribution (Lin 1995, Lin & Rimmele 1999, Khomenko et al. 2003), while the visible Fe I lines at 630 nm suggest that the characteristic field strength is in the kG range (Domínguez Cerdeña et al. 2003, Lites 2002, Socas-Navarro & Sánchez Almeida 2002). A predominance of the weaker field is suggested also by the observations in spectral lines that show hyperfine structure (López Ariste et al. 2002, Asensio Ramos et al. 2007). There are also cases when the visible lines gave predominantly weaker field (Rezaei et al. 2007a, Martínez González et al. 2008). Reasons for the disagreement could be: (1) the effect of the noise in the observational data (Bellot Rubio & Collados 2003), (2) different seeing conditions (Khomenko et al. 2005b), (3) inability of the inversion methods when applied to the 6301 & 6302 lines to give a unique information of the parameters retrieved (Martínez González et al. 2006) or (4) different Zeeman sensitivity in the two spectral regions (Socas-Navarro & Sánchez Almeida 2003). The observations give also different amounts of the mean unsigned flux density present in the internetwork regions. The retrieved values cover the range from a few Gauss to tens of Gauss (Sánchez Almeida et al. 2003, Sánchez Almeida 2008), which is significantly smaller than some of the Hanle-based estimates.

Recently, observations obtained with the Solar Optical telescope (Tsuneta et al. 2008a) on board of Hinode (Kosugi et al. 2007) offered the opportunity for the solar photosphere to be studied for the first time with the spatial resolution better then 0.3″ (without any obstructions coming from the terrestrial atmosphere). These observations strongly suggest that the internetwork field is mostly horizontal (Orozco Suárez et al. 2007b,c, Lites et al.

2008). The horizontal, loop-like magnetic features have a wide range of sizes, from the order of 1″ to 15″ (Martínez González et al. 2007, Harvey et al. 2007, Centeno et al. 2007, Ishikawa et al. 2008). The ones with the sizes smaller than the average size of the granular pattern are very dynamic (Ishikawa et al. 2008, Ishikawa & Tsuneta 2009). These horizontal features appear in the internetwork as well as in the plage regions with no significant difference in the magnetic field strength or the rate of occurrence. Their lifetimes range from a minute to about ten minutes, comparable to the lifetime of granules. They seems to first appear inside the granule, then move to the intergranular lanes where they finally disappear. The distribution of the azimuth of the horizontal fields seems to be uniform, which means that these features have no preferred orientation. Some of these characteristics (the size, abundance, weak magnetic field, no preferred orientation) is consistent with the structure of the magnetic field in surface dynamo simulations (Schüssler & Vögler 2008). But there is no obvious observational signature that would distinguish between different scenarios that can produce these horizontal fields. Flux emergence (Cheung et al. 2008) or flux expulsion by the granular flows, without any field being generated by the local dynamo action (Steiner et al. 2008) could also explain the existence of these features.

1.3 Numerical simulations vs. observations

The rapidly evolving numerical simulations of solar magnetohydrodynamic (MHD) processes have become an important tool in solar physics research. Although the introduction of the necessary physics (radiative transfer, partial ionization, open and transmitting boundaries etc.) made them comparable to the observations ("realistic"), they are still far from the solar conditions. The real solar values of magnetic and hydrodynamic Reynolds numbers (i.e. actual diffusivities) are still unreachable by the simulations since it is impossible to simultaneously resolve the diffusive length scales (of the order of centimeters for the viscous scale) and extend to the spatial sizes of the structures of interest (several megameters or more). It is thus also impossible to include all the processes relevant for the appearance and evolution of the magnetic field on the solar surface (e.g. the global dynamo, surface dynamo, flux emergence).

Nevertheless, realistic MHD simulations prove to be useful guides for the analysis and interpretation of observations. They can be used to study the complex interaction between magnetic field and convection at length scales and depths not accessible to observations. The physical processes responsible for various observational signatures can be explained on the basis of simulations (Carlsson et al. 2004, Keller et al. 2004, Shelyag et al. 2004). The simulations can also be used for testing different diagnostic techniques (Khomenko & Collados 2007, Orozco Suárez et al. 2007a). The simulations can help in realizing how, e.g., the limited spectral and spatial resolution, different instrumental effects or noise affect the observations (Khomenko et al. 2005b). In this way the simulations can provide help to determine what kind of instrumentation would improve our knowledge of the relevant processes. On the other hand, observational results provide the basis for the validation of the numerical codes and can stimulate their further development.

The important part in the comparison of the realistic MHD simulations with observations is taking properly into account the instrumental effects. This is done in the terms

of the realistic Point Spread Function (PSF). The PSF describes the way the instrument causes the radiation emitted by an object to be redistributed on the image plane. Even a perfect optical telescope induces image degradation due to diffraction at the finite aperture stop. Additional degradation effects, due to the instrumental stray light and imperfections are not easy to account for. In the case of the ground-based telescopes, it is particularly difficult to take into account the terrestrial atmosphere effects. Thus the usual way of degrading synthetic maps from simulations to account for observational limitations of ground-based telescopes depends strongly on assumptions about the nature of atmospheric seeing and straylight (Nordlund 1984, Schüssler et al. 2003, Rybák et al. 2006, Langangen et al. 2007).

1.4 Aim and outline of the thesis

As emphasized in the preceding discussion, the comparison of the realistic MHD simulations with observations is important for our general understanding of solar magnetism. This thesis presents an investigation in this direction. Results obtained with the realistic MURaM code (Vögler 2003, Vögler et al. 2005) are compared with the observations which are carried out with the spectropolarimeter (SP) (Lites et al. 2001) of the Solar Optical telescope (Tsuneta et al. 2008a) onboard of Hinode (Kosugi et al. 2007). The thesis study focuses on both (1) global characteristic of the granulation and the internetwork magnetic field and (2) on the processes behind the formation and cancellation of magnetic fields on granular scales. It is organized as follows:

• Chapter 2 contains a short description of the MHD simulations and observations used. The spectral lines chosen for this study are presented, as well as proxies employed.

• Chapter 3 describes the process of obtaining the realistic PSF for the Hinode/SP which is used in the subsequent chapters. The result gives the constraint for the granulation contrast - the root-mean-square of the normalized continuum intensity fluctuations.

• Chapter 4 shows the comparison of the synthesized polarization signals obtained from different simulation runs with the observations of the quiet Sun regions. Observations at different heliocentric angles with different noise levels are used. The possible role of the surface dynamo in the internetwork magnetism is discussed.

• Chapter 5 considers the formation of the kG flux concentrations in MHD simulations. Three different examples are given and differences are discussed. Also the quantitative comparison with observations is shown.

• Chapter 6 presents a study of flux cancellation site. Possible observational signatures of the process and the effects of spatial smearing are considered.

2 Method

This chapter contains a short description of the MHD simulations and observations used. A brief summary of basics related to the magneto-hydrodynamical (MHD) code is given in Sect. 2.1. Full description of the MHD code is given in Vögler (2003) (see also Shelyag 2004, Cheung 2006). Then the Radiative Transfer Equation (RTE) in the presence of a magnetic field will be presented (Sect. 2.2). The notation of del Toro Iniesta (2003) (see also Landi Degl'Innocenti 1992) is followed. The lines of iron lines selected for spectral synthesis are listed in Sect. 2.3. A short description of the instrument is given in Sect. 2.4. Finally, the description of the magnetic field proxies that are used throughout the thesis is given in Sect. 2.5.

2.1 The MURaM simulations

The MURaM (MPS/University of Chicago Radiative MHD) code has been developed by the magneto-hydrodynamic (MHD) simulation groups at the Max-Planck-Institut für Sonnensystemforschung in Katlenburg-Lindau by Vögler A., Shelyag S., Schüssler M. and at the University of Chicago by Cattaneo T., Emonet Th., Linde T (Vögler 2003, 2004, Vögler et al. 2004, 2005). It studies the interaction between convective flows and magnetic fields in the uppermost layers of the convective zone and the photosphere of the Sun. The evolution of the primary variables (ρ the density, ρ **v** the momentum, **B** the magnetic field and e the total energy density per unit volume) is obtained by solving the MHD equations on a three-dimensional, equidistant cartesian grid. The MHD equations solved by MURaM consist of: the equation of continuity,

$$\frac{\partial \rho}{\partial t} + \nabla \cdot (\rho\, \mathbf{v}) = 0, \tag{2.1}$$

the equation of motion

$$\frac{\partial \rho\, \mathbf{v}}{\partial t} + \nabla \cdot \left[\rho\, \mathbf{v}\mathbf{v} + (p + \frac{|\mathbf{B}|^2}{8\pi})\underline{I} + \frac{\mathbf{B}\mathbf{B}}{4\pi}\right] = \rho\, \mathbf{g} + \nabla \cdot \underline{\tau} \tag{2.2}$$

(where p is the gas pressure, g is the gravitational acceleration, $\underline{I}$ represents the 3×3 identity matrix and $\underline{\tau}$ the viscous stress tensor), the induction equation

$$\frac{\partial \mathbf{B}}{\partial t} + \nabla \times (\mathbf{v} \times \mathbf{B}) - \nabla \cdot (\eta \nabla \times \mathbf{B}) \tag{2.3}$$

($\eta = c^2/4\pi\sigma$ is the magnetic diffusivity, c the speed of light and σ the electrical conductivity) and the energy equation

$$\frac{\partial e}{\partial t}+\nabla\cdot\left[\mathbf{v}\left(e+p+\frac{|\mathbf{B}|^2}{8\pi}\right)-\frac{1}{4\pi}\mathbf{B}(\mathbf{v}\cdot\mathbf{B})\right] = \frac{1}{4\pi}\nabla\cdot(\mathbf{B}\times\eta\nabla\times\mathbf{B})+\nabla\cdot(\mathbf{v}\cdot\underline{\tau})+\nabla\cdot(K\nabla T)+\rho(\mathbf{g}\cdot\mathbf{v})+Q_{rad} \tag{2.4}$$

(T is the temperature and K the thermal conductivity). The total energy density per volume is the sum of internal, kinetic and magnetic energy densities: $e = \rho e_{int} + 1/2\rho v^2 + B^2/8\pi$. The radiative heating rate Q_{rad} is calculated as

$$Q_{rad} = \int_\nu\int_\Omega \rho\,\kappa_\nu(I_\nu - S_\nu)d\Omega\,d\nu, \tag{2.5}$$

where I_ν is the specific intensity, S_ν source function and κ_ν is the monochromatic opacity. When the assumption of the local thermodynamic equilibrium (LTE) is applied, as it is done in the MURaM code, the source function becomes the Planck function. The radiative heating rate is obtained by solving the radiative transfer equation (RTE)

$$\frac{dI_\nu}{d\tau} = \kappa_\nu\rho(S_\nu - I_\nu) \tag{2.6}$$

non-locally for 24 ray directions (3 per octant) and over frequency. The frequency integration is done in an approximate way, by using a binning method or pseudo line-blanketing (Nordlund 1982, Vögler 2003). The spectrum is rearranged into the 4 noncontiguous subsets (bins) so that the continuum and lines opacities of similar values are assigned to the same subset, represented by bin-averaged opacities. The RTE is solved for each of them.

The system of MHD equations Eq. (2.1), Eq. (2.2) Eq. (2.3) and Eq. (2.4) is closed with an equation of state which describes the relation between the thermodynamical quantities of the fluid T and p, as functions of ρ and e_{int}. The look-up tables were made by solving the Saha-Boltzmann equations for the first ionization of the 11 most abundant elements. This way, the partial ionization of the plasma is taken into account, which, together with the treatment of the radiative transfer, guarantees that the MURaM simulations meet the requirements of realistic solar simulations of the upper convection zone and the photosphere.

The size of the simulation domain and grid cell size is adjusted depending on the requirements of the study. The bottom boundary is open, i.e. the material is allowed to freely enter or leave the computational domain. In the regions of outflow, the flow below the boundary is assumed to be that obtained by extrapolating from within the computation domain. In inflow regions the velocity is assumed to be vertical. The imposed uniform pressure at the bottom boundary is continually adjusted so that the mass within the domain is kept constant and the energy per unit mass is adjusted so that the time averaged energy flux associated with the radiation leaving the box matches the level observed on the Sun. The magnetic field at the bottom boundary is assumed to be vertical. The top boundary can be either open or closed. The magnetic field there is either vertical or matched to a potential field above. The initial magnetic field also depends on the study. The MURaM code is used for study of the magneto-convective structure formation in the quiet Sun and plage region (Vögler et al. 2005, Shelyag et al. 2004), the surface dynamo (Vögler & Schüssler 2007), flux emergence (Cheung et al. 2007, 2008), magneto-convection in pores and sunspots (Cameron et al. 2007, Schüssler & Vögler 2006, Rempel et al. 2009). In this thesis, only a few runs are used, as noted in each chapter.

2.2 Radiative transfer

The radiative transfer equation (RTE) for polarized light in a plane-parallel atmosphere can be written in the form

$$\frac{d\mathbf{I}}{d\tau} = \mathbf{K}(\mathbf{I} - \mathbf{S}), \tag{2.7}$$

where $\mathbf{I} = (I, Q, U, V)^\dagger$ is the Stokes vector that gives a full description of the polarization state of light. The K is the 4x4 propagation matrix and the S is the source function vector that, in local thermodynamic equilibrium conditions (LTE) conditions, becomes $S = (B_\lambda(T), 0, 0, 0)^\dagger$. The propagation matrix K consists of (e.g. del Toro Iniesta (2003)):

$$K = \begin{pmatrix} \eta_I & \eta_Q & \eta_U & \eta_V \\ \eta_Q & \eta_I & \rho_V & -\rho_U \\ \eta_U & -\rho_V & \eta_I & \rho_Q \\ \eta_V & \rho_U & -\rho_Q & \eta_I \end{pmatrix} \tag{2.8}$$

where

$$\begin{aligned}
\eta_I &= 1 + \tfrac{\eta_0}{2}\Big[\phi_p \sin^2\gamma + \tfrac{\phi_b+\phi_r}{2}(1+\cos^2\gamma)\Big], \\
\eta_Q &= \tfrac{\eta_0}{2}\Big[\phi_p + \tfrac{\phi_b+\phi_r}{2}\Big]\sin^2\gamma\ \cos 2\chi, \\
\eta_U &= \tfrac{\eta_0}{2}\Big[\phi_p + \tfrac{\phi_b+\phi_r}{2}\Big]\sin^2\gamma\ \sin 2\chi, \\
\eta_V &= \tfrac{\eta_0}{2}[\phi_r - \phi_b]\cos\gamma \\
\rho_Q &= \tfrac{\eta_0}{2}\Big[\psi_p - \tfrac{\psi_b+\psi_r}{2}\Big]\sin^2\gamma\ \cos 2\chi, \\
\rho_U &= \tfrac{\eta_0}{2}\Big[\psi_p - \tfrac{\psi_b+\psi_r}{2}\Big]\sin^2\gamma\ sin2\chi, \\
\rho_V &= \tfrac{\eta_0}{2}[\psi_r - \psi_b]\cos\gamma.
\end{aligned} \tag{2.9}$$

The p, b, r indices stand for the π and σ components of a Zeeman multiplet, and η_0 is the ratio between the line and continuum absorption coefficients. The absorption $\phi_{p,b,r}$ and dispersion profiles $\psi_{p,b,r}$ represent the sums:

$$\begin{aligned}
\eta_k &= \eta_0 \textstyle\sum_M S^k_M H(a, v) \\
\rho_k &= \eta_0 \textstyle\sum_M S^k_M 2F(a, v),
\end{aligned} \tag{2.10}$$

where $k = p, b, r$, S_{M^k} the strength of each component, and H and F Voigt and Faraday-Voigt function. The remaining parameter v is

$$v = \frac{\lambda - \lambda_0}{\triangle\lambda_D} + \frac{e\lambda_0^2 B}{4\pi mc^2 \triangle\lambda_D}(g_l M_l - g_u M_u) + \frac{\lambda_0 v_{LOS}}{c\triangle\lambda_D} \tag{2.11}$$

with v_{LOS} being a bulk velocity along the line of sight, and g and M are the Landé factors and magnetic quantum numbers of the Zeeman split states of the lower and upper levels of the transition.

2.2.1 Milne-Eddington approximation

The Milne-Eddington (M-E) approximation assumes that the propagation matrix is constant throughout the atmosphere, and the source function varies linearly with the optical depth $\mathbf{S} = (S_0 + S_1\tau, 0, 0, 0)\dagger$. In this case the RTE has an analytical solution (Unno 1956, Rachkovsky 1962, 1967):

$$\begin{aligned} I &= S_0 + \triangle^{-1}[\eta_I(\eta_I^2 + \rho_Q^2 + \rho_U^2 + \rho_V^2)]S_1, \\ Q &= -\triangle^{-1}[\eta_I^2\eta_Q + \eta_I(\eta_V\rho_U - \eta_U\rho_V) + \rho_Q\Pi]S_1, \\ U &= -\triangle^{-1}[\eta_I^2\eta_U + \eta_I(\eta_Q\rho_V - \eta_V\rho_Q) + \rho_U\Pi]S_1, \\ V &= -\triangle^{-1}[\eta_I^2\eta_V + \eta_I(\eta_U\rho_Q - \eta_Q\rho_U) + \rho_V\Pi]S_1, \end{aligned} \tag{2.12}$$

where

$$\begin{aligned} \triangle &= \eta_I^2(\eta_I^2 - \eta_Q^2 - \eta_U^2 - \eta_V^2 + \rho_Q^2 + \rho_U^2 + \rho_V^2) - \Pi^2, \\ \Pi &= \eta_Q\rho_Q + \eta_U\rho_U + \eta_V\rho_V. \end{aligned} \tag{2.13}$$

2.2.2 SPINOR

SPINOR (Stokes-Profiles-INversion-O-Routines; Frutiger et al. (2000)) is an inversion code developed at the ETH Zürich and Max Planck Institut für Aeronomie (Solanki 1987, Solanki & Bruls 1994, Berdyugina et al. 2000). It consists of two modules: the STOPRO, which syntheses spectral lines (atomic and molecular) under local thermodynamic equilibrium (LTE), and INVERT, which uses the Levenberg-Marquardt algorithm (Press et al. 1992) to fit the spectral lines by modifying the initial model atmosphere. SPINOR takes into account the depth dependence of all important physical parameters for the formation of spectral lines. The RTE can be solved using two different methods. The first method is based on the Diagonal Element Lambda Operator (DELO) introduced by Rees et al. (1989), the other is based on a Hermitian strategy as presented by Bellot Rubio et al. (1998). The continuum absorption coefficient is calculated using the MULTI 2.2 opacity package (Carlsson 1986), which takes into account Rayleigh scattering by H and H_2, Thompson scattering by free electrons and bound-free transitions for 16 elements. To obtain the broadening by collisions with the neutral perturbers, the ABO theory is employed (Barklem & O'Mara 1997, Barklem et al. 1998). The SPINOR can be used in

Table 2.1: The atomic parameters for the synthesized lines taken from the VALD database. From left to right: the central (laboratory) wavelength, the excitation potential of the lower level of the line in eV (χ_l) , the oscillator strength of the line (log gf) and g_{eff} the effective Lande factor.

ion	λ [Å]	transition	χ_l	log gf	g_{eff}
Fe I	4918.993	z^7F_3 - e^7D_3	2.865	−0.370	1.69
Fe I	4920.502	z^7F_5 - e^7D_4	2.833	0.060	1.18
Fe II	4923.927	a^6S_5 - z^6P_4	2.891	−1.32	1.69
Fe I	4924.769	a^3P_2 - y^3D_2	2.279	−2.241	1.33
Fe I	4925.281	y^5D_4 - g^5F_4	4.103	−2.12	1.34
Fe I	4927.417	a^1H_5 - w^3F_4	3.573	−1.99	2.26
Fe II	5197.577	$a^4G_{2.5}$ - $z^4F_{1.5}$	3.23046	−2.10	1.667
Fe I	6301.501	z^5P_2 - e^5D_2	3.654	−0.718	1.67
Fe I	6302.494	z^5P_1 - e^5D_0	3.686	−1.203	2.49

different modes: for multi-component inversion (Mathew et al. 2003, Riethmüller et al. 2008), with assumption of flux tube model configuration (Frutiger & Solanki 2001), with discontinuities in physical parameters along the line of sight (Borrero et al. 2006) or for obtaining disk-integrated spectra (Frutiger et al. 2005).

2.3 Selected spectral lines of iron

The atomic parameters of the chosen iron lines are given in Table 2.1. The Fe I 630.15 nm and 639.25 nm lines are the lines in which the spectropolarimeter onboard Hinode is operating. The characteristics of other lines are discussed in Chapter 6. Figure 2.1 shows the height of formation for most of them. The heights are calculated as a centroid of the contribution functions (CF) to the line depressions at the wavelengths of the line minima.

2.4 Spectropolarimeter onboard Hinode satellite

The Hinode (Solar-B before launch; Kosugi et al. 2007) satellite was launched on 22 September 2006. The main objective of the Hinode mission is to help understand the generation, transport, and dissipation of solar magnetic energy with a set of three coordinated telescopes. Owing to the Sun-synchronous polar orbit, Hinode is able to continuously observe the solar atmospheric structures. Hinode mission is performing simultaneous observations of the photosphere, the chromosphere, the transition region, and the corona to understand how the changing photospheric and chromospheric magnetic fields results in a dynamic response of the coronal plasma. For this purpose, Hinode carries the X-ray Telescope (XRT; Golub et al. 2007), the EUV Imaging Spectrometer (EIS; Culhane et al. 2006), and the Solar Optical Telescope (SOT).

The Solar Optical Telescope (SOT; Tsuneta et al. 2008a) consists of the Optical Telescope Assembly (OTA) and the Focal Plane Package (FPP). The OTA is a 50-cm Gregorian telescope, and the FPP includes the narrowband filtergraph (NFI) and the broadband

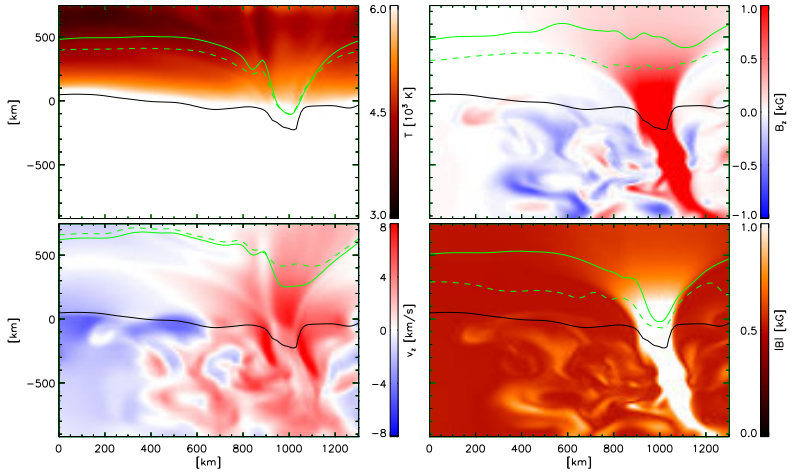

Figure 2.1: The height of formation of selected iron lines: Fe I 630.15 nm (solid, left upper panel), Fe I 630.25 nm (dashed, left upper panel), Fe II 492.39 nm (solid,right upper panel), Fe II 519.76 nm (dashed,right upper panel), Fe I 491.9 nm (solid,left lower panel), Fe I 492.05 nm (dashed,left lower panel), Fe I 492.48 nm (solid,left lower panel) and Fe I 492.53 nm (dashed,right lower panel). Panels show vertical cut through the magnetic feature: temperature, vertical components of magnetic field, vertical component of velocity, magnetic field strength (*clockwise*). Black line marks the optical depth unity level.

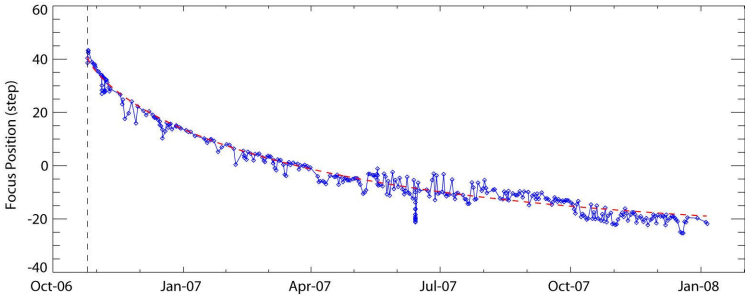

Figure 2.2: G-band focus position history. Gradual drift of the focus is caused by shrinkage due to dehydration of the frame structure that holds primary and secondary mirror. Courtesy of Y. Katsukawa.

filtergraph (BFI), plus the Stokes Spectro-Polarimeter (SP). The 50-cm diameter SOT can obtain a continuous, seeing-free series of images with spatial resolution of $0.2'' - 0.3''$. The Broadband Filter Imager (BFI) and NFI observations cover the region from the low photosphere through the chromosphere (spectral range from 388.3 nm for CN band to 668.4 nm for the continuum images in red). The Spectro-Polarimeter (SP) provides the line profiles in all Stokes parameters, with the high spectral resolution of 2.15 pm in two magnetically sensitive lines at 630.2 nm. Two facts are relevant for the study presented in Chapter 3. First, the SOT has a single focusing (reimaging) mechanism at the entrance of the FPP (Suematsu et al. 2008). Second, there is a large focus change due to a dehydration shrinkage of the main frame that hold primary and secondary mirror (Suematsu et al. 2008). Figure 2.2 shows the gradual drift of the focus at the G-band spectral range during the fist period of the Hinode operation. Within a year it changed for at least 40 steps.

The SP (Lites et al. 2001) operates exclusively at the photospheric Fe I 630 nm lines. It contains a rotating, low-order crystalline quartz retarder for polarization modulation (one polarization modulator for two instruments; the narrowband filter instrument should have also made polarimetric measurements at the wavelengths of 517, 525 mm) and a reflecting Littrow spectrograph design. After the polarization modulator, the light is reflected by the tip-tilt minor, the beam dividing prism, and the slit scan mirror, oriented to introduce minimal crosstalk. The reimaging lens forms an image of the Sun onto the spectrograph slit. The slit scan mechanism can displace the solar image on the slit by up to $\pm 160''$ (on the Sun) in increments of $0.16''$ so that $0.16'' \times 164''$ rectangle on the Sun can be sampled in order to build up vector magnetic field maps. The light dispersed from the 79 line/mm grating is directed by an off-axis paraboloid collimator towards the detector. Polarization analysis is accomplished by a modified Savart plate beam splitter. The two orthogonal polarization beams are separated and directed towards a CCD detector with two active areas, one for each beam from the beam splitter. Each of the square pixels of the CCD, being 12μm $\times 12\mu$m to match the width of the spectrograph slit, sample 2.0pm of spectrum and $0.16''$ along the slit. A spectral range of 0.22 nm is sufficient to measure the Doppler shifted spectral profiles of both 630 nm Fe I lines, so the data transmitted by the instrument comprise only about 120 of the 224 spectral pixels for each polarization image. The additional spectral range on the detector is present to allow for alignment tolerances of the spectrograph optics during launch/release, for curvature of the spectral field, and for orbital and solar rotational Doppler shifts (Lites et al. 2001). The SP CCD camera records images and transmits them in digital form to the FPP 'smart memory' at a 10 Hz rate (the rate of polarization modulator). The polarization states that are there temporally encoded and accumulated the over several modulation cycles until the target S/N ratio is achieved (typically S/N = 1000 in the spectral continuum).

The four basic SP observing modes are:

- Standard Mode - Exposure time is 4.8 sec, or three full rotations of the modulator. The slit steps are $0.16''$ and a $160'' \times 164''$ map is obtained in approximately 83 minutes. This mode is most useful for maps of the vector magnetic field of active regions.

- Fast Map Mode - The mode bins 2×2 pixels, both along the slit and perpendicular to it, resulting in spatial samples $0.32'' \times 0.32''$. A $160'' \times 164''$ fast map will require approximately 28 minutes.

- Dynamics Mode - The data is collected at reduced S/N, and on at least 2/3 of the full 160″ slit length with the scan step of 0.16″. This mode is used for recording very rapid changes in the photosphere at small scales.
- Deep Magnetogram Mode - This mode permits the polarization signal to be integrated over many rotations of the modulator so that a high S/N is obtained. The mode is suitable for observing a very weak polarization signal in the internetwork regions.

The row data obtained with SP are corrected for dark current, flat-field, instrumental cross-talk and orbital drift along the wavelength axes (Ichimoto et al. 2008) by using the IDL routine `sp_prep` of the `SolarSoft`[1] package.

2.5 Magnetic field proxies

The `sp_prep` procedure gives, among other parameters, magnetic field proxies: apparent longitudinal (B^L_{app}) and transversal (B^T_{app}) magnetic flux density. It calculates the wavelength-integrated Stokes V (V_{tot}),

$$V_{tot} = sgn(V_b)\frac{\left|\int_{\lambda_b}^{\lambda_0} V(\lambda)d\lambda\right| + \left|\int_{\lambda_0}^{\lambda_r} V(\lambda)d\lambda\right|}{I_c \int_{\lambda_b}^{\lambda_r} d\lambda}, \tag{2.14}$$

where $sgn(V_b)$ is the sign of the blue peak, λ_0 is the line center, and $\lambda_{r,b} = \lambda_0 \pm 30\,\mathrm{pm}$. The wavelength-integrated Stokes Q (Q_{tot}) is obtained as

$$Q_{tot} = \frac{\int Q(\lambda) Q_{mask}(\lambda) d\lambda}{I_c \int Q_{mask}(\lambda) d\lambda} \tag{2.15}$$

where I_c is the local continuum intensity and Q_{mask} is average Stokes Q profile. Its purpose is to reduce the contribution of noise. The Q_{mask} is calculated in the following way (Lites et al. 2008): (1) the 'preferred-frame azimuth' ϕ_r for the magnetic field for each pixel is determined with a least-squares minimization procedure following Auer et al. (1977) (see also Lites et al. 1999), (2) the measured Stokes Q, U are then rotated to the preferred azimuth so that Stokes U becomes 0, (3) the sum of the resulting Q profiles over the Hinode/SP quiet Sun map gives the Q_{mask}.

The V_{tot} and Q_{tot} are calibrated into a measure of apparent flux densities, theoretically, under the M-E assumption. A set of theoretical Stokes profiles are synthesized to which the spectral mask of equation Eq. (2.15) is applied. The calculations take the following parameters for the M-E synthesis: $\eta_0 = 8$, $\triangle\lambda_D = 3.5$ pm, $a = 0.3$, $S_0 = 0.25 I_c$, and $\mu S_1 = 0.75 I_c$, where a is the damping parameter relative to the Doppler width $\triangle\lambda_D$. The magnetic field was assumed to be perpendicular to the LOS. These parameters are typical of the results of M-E inversions of the internetwork fields.

This calibration is tailored to retrieve the field value from weak and noisy internetwork signals. It assumes that the magnetic structures are spatially resolved (fill the resolution element) and does not take into account the magnetic field variations over the height

[1] http://www.lmsal.com/solarsoft/

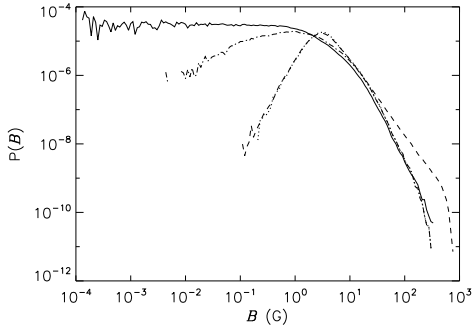

Figure 2.3: The probability distribution functions (PDF) for the magnetic field strengths and derived field proxies: Hinode SP 'normal mode' map B^L_{app} (dashed line), MURaM simulation B_{ave} (see text, solid line), MURaM synthetic B^L_{app} (B derived from Stokes V, dot-dashed), and B^L_{app} including a noise level of 1.1×10^{-3} (dotted). The PDF of the synthetic observations appear peaked although we have a monotonic distribution of vertical field strengths.

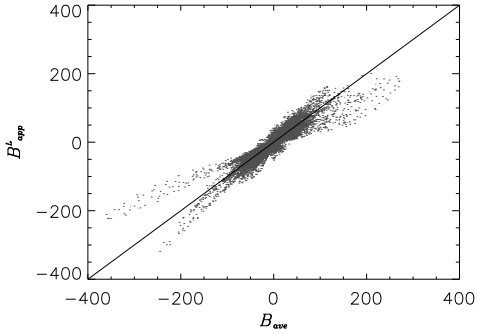

Figure 2.4: B^L_{app} derived from MURaM dynamo run versus B_{ave}, the actual vertical magnetic field strength averaged over $\log\tau \in [-3.5, .1]$. The linear Pearson correlation for the two quantities is $r = 0.92$. Note the large scatter.

range where lines are formed. Consequences of the latter assumption are studied in the next section[2], when B^L_{app}, obtained from Stokes V profiles synthesized from simulations, is compared with the vertical component of the actual magnetic field. The continuation of the study is given in Chapter 4.

[2]The material given here is published in Pietarila et al. (2008) and Pietarila Graham et al. (2009).

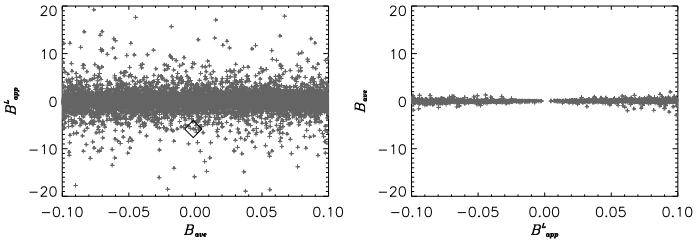

Figure 2.5: **(Left)** B^L_{app} versus B_{ave} for $B_{ave} < 0.1\,\mathrm{G}$ **(Right)** B_{ave} versus B^L_{app} for $B^L_{app} < 0.1\,\mathrm{G}$ (B^L_{app} computed from noiseless V-profiles). These plots indicate the bias that strong Stokes V signal can be associated with a pixel with weak averaged magnetic field, but seldomly *vice-versa.*

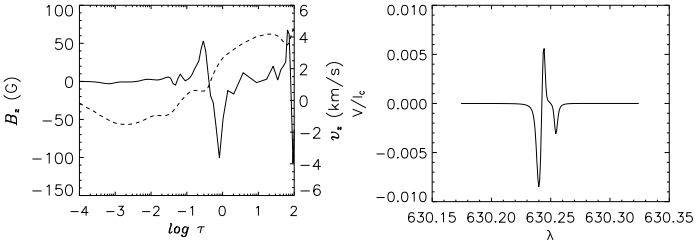

Figure 2.6: **(Left)** B_z (solid line) and v_z (dashed line) versus optical depth, $\tau_{500\,nm}$, and **(Right)** Stokes V profile for the pixel indicated by a diamond in Fig. 2.5 ($B^L_{app} = -5.9\,\mathrm{G}$ and $B_{ave} = -1.6 \cdot 10^{-3}\,\mathrm{G}$). At $\log\tau = 0$ the positive and negative contributions to B_{ave} have nearly cancelled (integrating downward). The Stokes V signal is stronger than that which would result from a uniform $1.6 \cdot 10^{-3}\,\mathrm{G}$ field, but it is asymmetric. Strong gradients lead to asymmetric profiles but also to $|B^L_{app}| \gg |B_{ave}|$.

2.5.1 PDFs

A marked difference exists between the PDFs inferred from Zeeman polarimetry (e.g., Khomenko et al. 2005a, Lites et al. 2008) and the PDFs from numerical computations (e.g., Socas-Navarro & Sánchez Almeida 2003, Vögler & Schüssler 2007). For example, in Fig. 2.3 we present the PDFs from the Hinode "normal mode" map magnetogram (apparent vertical magnetic flux density, dashed line) and of MURaM simulation dynamo run (average vertical magnetic field, solid line). The polarimetric observation peaks at $B^L_{app} \approx 3\,\mathrm{G}$ while the simulation possesses a monotonic distribution without a distinct maximum: there exists a greater amount of weak vertical field than indicated by the observations. The observation also shows greater intermittency (the distribution has an enhanced strong signal (field) tail when compared to a Gaussian) than the simulation. This can possibly be attributed to the much lower Reynolds number of the numerical simulation compared to the Sun as well as to the smaller simulation box: contributions

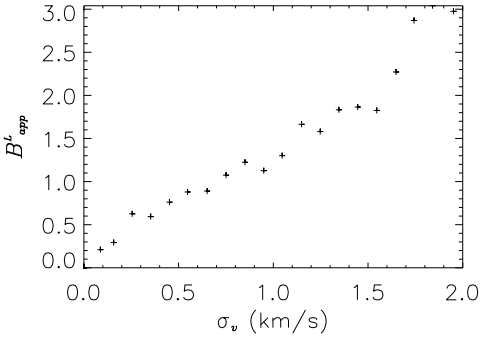

Figure 2.7: The average B^L_{app} versus standard deviation of the fluctuations of the vertical velocity along the (vertical) line-of-sight, σ_v, for all pixels with $|B_{ave}| < 0.1$ G. Pixels are binned by σ_v before averaging. With strong velocity differences between different heights in the atmosphere, the total Stokes V signal increases as the Doppler-shifted absorption from positively and negatively oriented fields show less cancellation.

from dynamo action in the deeper layers and supergranular network flux concentrations are absent. To address the qualitative difference (peaked versus monotonic) between simulations and observations, we ask what PDF of Zeeman-based observational signatures would result if PDF(B_z) monotonically decreasing with increasing vertical field strength (instead of possessing a peak). Our approach is to assume the distribution of the field strengths from turbulent MURaM simulations and examine the consequences of such a distribution on Stokes V observations.

Though noise, resolution, and other instrumental factors are important in any real observation, we first address the question assuming a 'perfect' instrument. Using the synthetic profiles from dynamo run, we calculate V_{tot} with Eq. (2.14) and determine B^L_{app} following Lites et al. (2008). In Fig. 2.4, the derived B^L_{app} signal versus B_{ave}, the vertical magnetic field strength averaged over the height range corresponding to $\log\tau \in [-3.5, .1]$, is shown. This quantity was selected for its linear Pearson correlation with B^L_{app} of $r = 0.92$ and its coefficient of linearity, $B^L_{app} \approx 1.0 B_{ave}$, which is consistent with the calibration of Lites et al. (2008). This height range also encompasses most of the formation height of the Fe I lines at 6301 and 6302 Å. Though B^L_{app} and B_{ave} are well correlated, there is a large scatter. We also note, that changing the range to $\log\tau \in [-2, .1]$ does not significantly affect the correlation, r. This indicates that most of the Stokes V signal is generated in deeper layers (Orozco Suárez et al. 2007a).

In Fig. 2.3, we present a comparison between the PDFs of B^L_{app} as derived from the synthetic Stokes V profiles (dash-dotted line) and B_{ave} (solid line). PDF(B_{ave}) monotonically decreases with the field strength, while PDF(B^L_{app}) shows a peak near 1 G and a strong decline towards smaller field strengths. The PDFs for maximum Stokes V amplitude and total circular polarization are qualitatively similar to that shown for B^L_{app}. The PDFs for the vertical magnetic field from different volumes and 2D cross sections from all simulation runs, chosen either by height or by optical depth, show similar PDFs to

that shown for B_{ave}. This means that the monotonically decreasing distribution is a robust feature of the vertical magnetic field when sampled by geometrical height, optical depth, or by averaging over the vertical direction. The difference between observations and simulations is caused by the radiative transfer, that produces circular polarization from longitudinal magnetic field.

The above result shows that caution is needed when interpreting the distribution of the Stokes V signal in order to avoid a drastic underestimation of the occurrence of weak field. This caution naturally extends to moments of the distribution such as mean vertical flux density or mean vertical magnetic energy density. For example, B^L_{app} and B_{ave} are very well correlated, but their averages, $\left\langle |B^L_{app}| \right\rangle = 6.9\,\mathrm{G}$ and $\langle |B_{ave}| \rangle = 5.5\,\mathrm{G}$, differ significantly. We see that an over estimation of 26% results from assuming the vertical magnetic field to have the same distribution as the signal derived from Stokes V, even in the absence of noise (note that this is close to the 20% loss found in Sánchez Almeida et al. 2003).

To understand in more detail how radiative transfer contributes to a peaked PDF, we examine a few selected $V-$profiles. Pixels with weak B_{ave} must be generating strong B^L_{app} signals for PDF(B^L_{app}) to become peaked. Indeed, Fig. 2.5 shows this is the case. There are many pixels for which $|B_{ave}| < 0.1\,\mathrm{G}$ while $|B^L_{app}| > 5\,\mathrm{G}$. On the other hand, we see that when $|B^L_{app}| < 0.1\,\mathrm{G}$, $|B_{ave}|$ is always less than 4 G. In Fig. 2.6, we examine one case of how weak B_{ave} can be associated with strong B^L_{app}. For $\tau \in [0.1, 1]$, the vertical magnetic field takes on values of tens of Gauss. In this region, there are also strong gradients (and direction reversals) for both the magnetic and velocity fields. In this case, because of the magnetic field reversal, B_{ave} is nearly zero. However, because of the velocity gradient, the contributions to the Stokes$-V$ profile from the positive and negative magnetic polarities are Doppler-shifted with respect to each other. For this reason, the Stokes V signal is not cancelled. This is further illustrated in Fig. 2.7 where we plot the mean B^L_{app} for all pixels with $|B_{ave}| < 0.1\,\mathrm{G}$ versus the strength of the vertical velocity fluctuations. There is a clear trend of the stronger signal with increased Doppler shifts between the different heights in the atmosphere. We conclude that the Doppler shifts of the absorption profiles are responsible for the peaked PDF from our noiseless synthetic B^L_{app}. In effect, $|V_{tot}|$ is a combination of the vertical mean of B_z and the vertical mean of $|B_z|$ (depending on $v_z(z)$) and, consequently, the PDF of B^L_{app} does not correspond to PDF(B_z) from any geometrical height, optical depth, or volume. Such a failing of B^L_{app} to accurately represent B_z cannot be captured using the Milne-Eddington approximation (used to calibrate B^L_{app}), which has no gradients by definition.

To examine the effect of noise on the PDF, we consider synthetic Stokes V profiles with noise added at a polarization precision of 1.1×10^{-3} (similar to that of the Hinode observations). The PDF of this noisy synthetic observation is shown as a dotted line in Fig. 2.3 and closely resembles the observational PDF for signals weaker than a few Gauss. Note that, the noise accentuates the peak in the PDF even further. By examining Eq. (2.14) for V_{tot} (B^L_{app} is a nearly-linear function of V_{tot}), we see that by taking the absolute value of the blue and red lobes separately the effect of noise becomes the sum of two non-negative measurement errors. That is,

$$V_{tot}^{measured} = V_{tot}^{true} + |\epsilon_b| + |\epsilon_r|\,, \tag{2.16}$$

where ϵ_b and ϵ_r are the measurement noise in the blue and red lobes (e.g., $\epsilon_b \equiv \sum_{i=1}^{N_b} \epsilon_i/N$ where ϵ_i are the random variables associated with the measurement noise in each wavelength bin). Assuming these two random variables, ϵ_b and ϵ_r have Gaussian distributions, their separate PDFs for their absolute values will peak at zero. However, the PDF of the sum of their absolute values will peak at a non-zero value due to reduced likelihood that $|\epsilon_b|$ and $|\epsilon_r|$ are small simultaneously: the PDF of the sum of two independent random variables is the convolution of their individual PDFs,

$$P(\epsilon) = \frac{2}{\pi\sigma_b\sigma_r} \int_0^{\epsilon} e^{-(\epsilon-\xi)^2/2\sigma_b^2} e^{-\xi^2/2\sigma_r^2} d\xi \tag{2.17}$$

for ϵ_b,ϵ_r Gaussian and $\epsilon = |\epsilon_b|+|\epsilon_r|$. Because we take the absolute values, the individual PDFs are zero for negative values (this sets the limits of integration for Eq. (2.17)). Hence, their convolution is zero at zero and peaks instead for some finite positive value. Assuming ϵ_b and ϵ_r have identical identical standard deviation $\sigma = \sqrt{2}\cdot 2.4\,\mathrm{G}$ (taken from Lites et al. 2008), it can be shown that the peak in the PDF for B^L_{app}, Eq. (2.17), is given by the solution of

$$\frac{B}{\sigma^2} \int_0^{B/2} e^{-\xi^2} d\xi - e^{-B^2/4} = 0. \tag{2.18}$$

This predicts a peak in the PDF at $B^L_{app} \approx 3\,\mathrm{G}$, close to that seen in the actual observation. Consequently, adding noise leads to a further decrease of the number of pixels with very weak field and thus accentuates the maximum of the PDF. This indicates that a monotonic PDF(B_z) is qualitatively consistent with observations.

3 Granulation Contrast

3.1 Introduction

The root-mean-square of the normalized continuum intensity fluctuations, within an area on the solar disk, is determined mainly by the intensity variation between the bright granules and the darker intergranular lanes, and thus is usually referred to as the *granulation contrast.* It is a key property of solar surface convection because it is connected with the temperature difference between rising (granules) and descending gas masses (intergranules), and thus related to the efficacy of the convective energy transport.

Reliable measurements of the granulation contrast are notoriously difficult, since the observed contrast suffers significantly from image degradation by the optical system and, most importantly in the case of ground-based telescopes, by seeing and straylight effects due to the terrestrial atmosphere. To deduce the 'true granulation contrast' from measurements, we need to deconvolve the observed images by considering the modulation transfer through the optical setup (telescope, instruments, detector, etc.), in addition to through the terrestrial atmosphere. The quantitative effects of the latter are poorly understood and it is therefore unsurprising that the reconstructed values of the granulation contrast, documented in the literature, cover a broad range (see, e.g., Table 2 in Sánchez Cuberes et al. 2000). This remains true even if additional constraints, such as measurements of the intensity profile across the lunar limb during a partial eclipse, are used to derive the effective point-spread function (e.g., Levy 1971, Deubner & Mattig 1975, Nordlund 1984, Sánchez Cuberes et al. 2000).

In the case of balloon-borne stratospheric observations, the influence of the atmosphere is negligible. Even under these conditions, however, the scatter of the reconstructed contrast values is large (Bahng & Schwarzschild 1961, Pravdyuk et al. 1974, Altrock 1976, Edmonds & Hinkle 1977, Wittmann & Mehltretter 1977, Schmidt et al. 1979, Wittmann 1981), presumably because the proper consideration of the instrumental effects is nontrivial (Durrant et al. 1983).

Although the range of contrast values derived from observations is quite wide, the values predicted by 3D radiative HD/MHD simulations are significantly higher (e.g. Stein & Nordlund 2000, Vögler et al. 2005, Wedemeyer-Böhm 2007). This is unsurprising, since the horizontal resolution of such simulations (10–40 km) is far better than what can be achieved observationally at present. To compare the observed contrast values with predictions from simulations, the synthetic images derived from simulations must be degraded in the same way as the observations, taking into account the effects of the optical system and, in the case of ground-based telescopes, the terrestrial atmosphere. This procedure is prone to the same uncertainties as the deconvolution of observations; the result depends

strongly on assumptions about the nature of atmospheric seeing and straylight (Nordlund 1984, Schüssler et al. 2003, Rybák et al. 2006) and we are unable to infer if the simulation predictions are consistent with observations, or otherwise. However, the good agreement between observed and simulated spatially averaged spectral line bisectors indicates that the simulated intensity contrasts are probably close to actual values (Asplund et al. 2000).

A new era has begun with the launch of the 50-cm Solar Optical Telescope (SOT, Tsuneta et al. 2008a) on the *Hinode* satellite (Kosugi et al. 2007). The good performance and low straylight level of the spectropolarimeter (SP, Lites et al. 2001) and complete absence of atmospheric effects, enable a far more reliable determination of the granulation contrast at 630 nm, the wavelength at which the SP operates. In this chapter, we compare the intensity contrast of a *Hinode* SP continuum map of the quiet Sun with predictions of MHD simulation.

3.2 Observations and simulation data

We determine the observed contrast from a map of the continuum intensity at 630 nm wavelength obtained on Jan. 16, 2007 (12:10:10 – 13:36:49 UT), using the scan mode of the *Hinode* SP with an exposure time of 4.8 s per slit position. The map covers a field of 163" × 164" of 'quiet' Sun, close to disk center. The slit width, the sampling step size, and the CCD pixel pitch all correspond to 0.16". The data were reduced using standard routines that correct for various instrumental effects. After reduction, we find an rms contrast of the continuum intensity of 7.0%.

The 3D MHD simulation snapshot that we consider represents the saturated (statistically stationary) state of the dynamo run C of Vögler & Schüssler (2007). The computational box contains $648 \times 648 \times 140$ cells; it corresponds to a physical size on the Sun of 4.86×4.86 Mm^2 in the horizontal and 1.4 Mm in the vertical direction, the latter ranging from about 900 km below to 500 km above continuum optical depth unity at 630 nm ($\tau_{630} = 1$). The simulation has been run with non-grey radiative transfer using the *MURaM* code (Vögler 2003, Vögler et al. 2005). With a horizontal grid-cell size of 7.5 km, this simulation had one of the highest resolutions achieved so far. The snapshot that we use, has an average unsigned vertical magnetic field of about 7 G at $\tau_{630} = 0.1$, which we consider as a reasonable representation of the 'quiet' Sun. The corresponding original (unsmeared) continuum image at 630 nm shows an rms contrast (standard deviation divided by mean value) of 14.4%. The particular choice of snapshot was not critical for the results presented here. Considering a number of other snapshots and simulations of different spatial resolution or amount of magnetic flux in the simulation box, we found contrast values that were typically between 14% and 15%.

3.3 Modeling of the system PSF

The difference between the observed and original contrast of the simulation amounts to more than a factor of two (7.0% vs. 14.4%). Since there is no atmospheric distortion of the image, we investigate whether instrumental effects alone can account for this significant degradation.

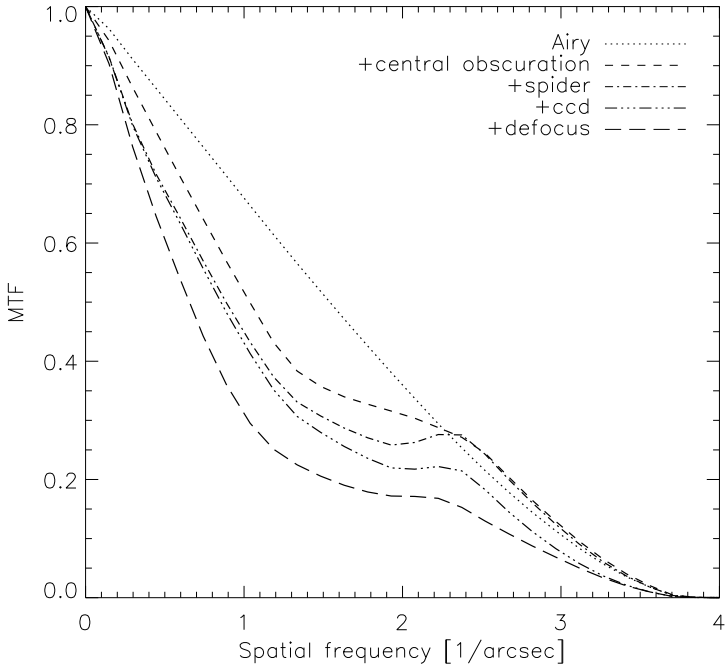

Figure 3.1: Change of the Modulation Transfer Function when the effects of the different parts of the optical system are sequentially taken into account: telescope aperture ('Airy'), central obscuration, secondary mirror and spider, sampling (CCD), and a defocus of 1.5 mm (about 9 steps of the focus mechanism).

The intrinsic resolution of the simulated images considered here (equivalent to 0.01" pixel size) is considerably better than the resolution of the 50-cm *Hinode* SOT; the degradation of the synthetic image based on the simulation result can therefore be modeled by applying an effective point-spread function (PSF). We convolved our simulated intensity maps in the 2D spatial domain with different PSFs, which represented a more and more realistic optical systems. To this end, we modeled the telescope and the transfer optical path down to the spectrograph entrance slit using the commercial optical design software ZEMAX[1]. While the telescope was modeled with the nominal SOT surface parameters, the transfer (refocussing) path was modeled in paraxial approximation, which, however, has no influence on the final results of our calculations. ZEMAX calculates the PSF as the Fourier transform of the wavefront in the exit pupil of the system.

We describe the contrast degradation by the optical system using the Modulation

[1] www.zemax.com

Transfer Function (MTF), which is the Fourier transform of the point-spread function. In this way, the various effects can be considered step by step, as indicated below. Figure 3.1 shows the corresponding change of the system MTF.

Telecope aperture: The *Hinode* SOT is an $f/9.1$ Gregory system with an aperture of 50 cm, which corresponds to a cut-off at $1/0.26$". Higher spatial wave numbers are not transmitted by the system, while low to intermediate wave numbers are transmitted with relatively high contrast.

Central obscuration and spider: Important contributors to the contrast reduction are the central obstruction of the telescope by the secondary mirror, which produces a linear obscuration of $0.344 = 17.2\,\mathrm{cm}/50\,\mathrm{cm}$, and the diffraction by the three spider elements, which are of 4 cm width each, holding the secondary. The effect of the central obstruction is that the highest spatial wave numbers are largely unaffected, while the intermediate wave numbers are significantly damped. The spider structure adds to this damping.

Spatial sampling: Since the data considered here are obtained using the spectropolarimeter, we have to consider the sampling and integration effects of the slit and the CCD detector. The sampling and the integration effects of the detector are approximated by powers of sinc functions (Boreman 2001).

Defocus: Low-order optical aberrations damp the MTF at low spatial wave numbers. Since the *Hinode* Focal Plane Package (FPP) is a complex system, it is difficult to model in detail all relevant contributions from optical, optomechanical, and electronic parts of the system. We therefore consider only the effect of a defocus in the plane of the SP slit. It turns out that a small amount of defocus can reduce significantly the intensity contrast, while leaving the fine-scale resolution of the system unaffected. The focus of the *Hinode* science instruments is controlled by means of a common reimaging lens that can be shifted in a range of ±25 mm, with a step of 0.17 mm.

In addition, we investigated the effect of the (lossy) JPEG compression which was applied to the images. The change of the rms contrast turned out to be negligible, even for high compression factors.

3.4 Degradation of the simulation data

To compare with the *Hinode* result, we convolved the intensity maps calculated from the simulation with the different PSFs resulting from modeling the *Hinode* SOT as described in the previous section. After convolution, the degraded images were binned to represent the sampling and integration effects of the finite slit width, step size of the spatial sampling, and the pixel size.

Figure 3.2 shows the evolution of the histogram of intensity values in the simulation image as the various effects of the optical system are introduced. The rms contrast values for the various steps are listed in Table 3.1. The basic telescope effects (primary aperture, obscuration, and spider) reduce the rms contrast to 8.7%, presumably since the small-scale intensity structure in the intergranular lanes is lost. There is almost no further contrast degradation due to sampling and rebinning (CCD), which indicates that the remaining contrast is determined mainly by spatial scales that are significantly larger than the critical sampling limit of the diffraction pattern. Once the fine detail in the granular lanes is no longer resolved, the contrast is dominated by the intensity differences between the

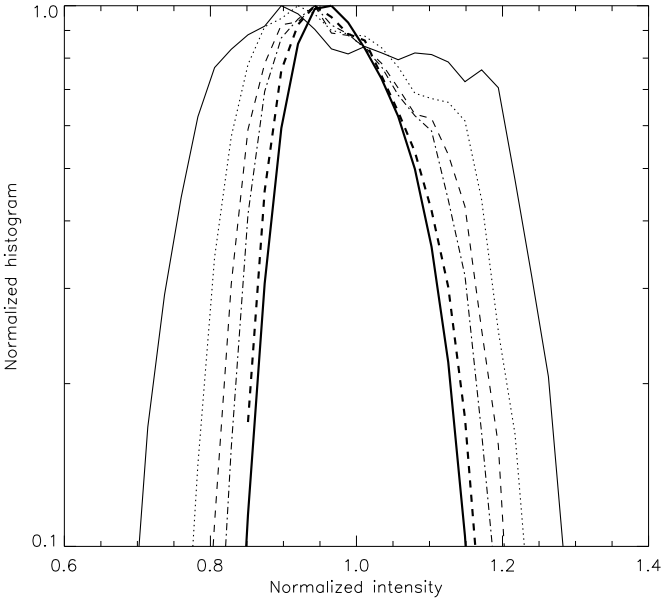

Figure 3.2: Normalized histograms of the continuum-intensity values at 630 nm, obtained for 35 equal bins between 0.6 and 1.4 of the mean intensity. Shown are results for the original synthetic image from the simulation snapshot (outermost, solid curve) and for the degraded images corresponding to the MTFs shown in Fig. 6.16 (same line styles as used there). The two thick inner curves represent the degraded synthetic image assuming a defocus of 1.5 mm (thick dashed curve) and the continuum map observed with *Hinode* SP (thick solid curve).

granules and the average intensity of the intergranular lanes, which is almost unaffected by the integrating effect of the detector pixels. Similar values of the contrast reduction up to this step were obtained by Orozco Suárez et al. (2007c).

The difference between the rms contrast degraded so far (8.5%) and the observed contrast (7.0%) is still significant. Another factor that contributes to contrast degradation is a slight defocus of the SP, which affects mainly the low to intermediate spatial wave numbers. We have no direct information about the amount of defocus for the dataset considered here; we, however, obtained empirical evidence about the effect of defocus on the intensity contrast using a number of SP datasets for different focus positions, taken only an hour earlier than the map analyzed here. Apart from the exposure time of 1.6 s per slit position and the smaller size of the maps, all other observational parameters are the same. For every focus position, a map that covers a field of $3.2" \times 82"$ was generated. The corresponding contrast values given in Fig. 3.3 confirm the rather sensitive dependence

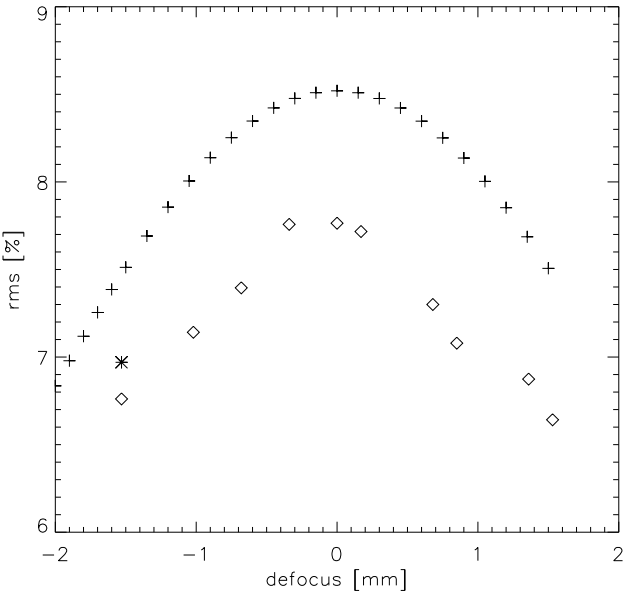

Figure 3.3: Intensity contrast as a function of telescope defocus. Shown are results for a SP data set used taken on Jan. 16, 2007, 10:54:14–11:06:52 UT (diamonds) and the contrast values for the degraded simulation image (crosses). The value for the large map used to compare with the simulation is indicated by the asterisk, assuming that the location of the optimal focus was the same as for the other dataset. This also gives an indication of the observational uncertainty.

Table 3.1: Values of the rms intensity contrast after applying the PSFs corresponding to the MTFs shown in Fig. 3.1.

effects taken into account	rms [%]
none	14.4
Airy	10.9
+ central obscuration	9.6
+ spider	8.7
+ CCD	8.5
+ defocus (1.5 mm)	7.5

on focus position. The figure also shows the dependence of the contrast of the simulation image on the defocus value. The large observational map with a contrast of 7.0% (indicated by the asterisk) was taken with a defocus of 8-9 steps (1.36 mm – 1.53 mm) from the optimal position in Fig. 3.3. The degraded simulation image corresponding to about this defocus value (1.5 mm) has a contrast of 7.5%.

As an illustration of the image degradation, Fig. 3.4 shows the original continuum image from the simulation (top panel, the periodic simulation box is drawn fourfold for the sake of better visibility) and the final degraded image (middle). A subset of the observational map of the same size is shown in the bottom panel, using the same color scale.

The remaining deviation of 0.5% from the observed value of about 7%, and the general shift between the curves for simulation and observation in Fig. 3.3, can be ascribed to various degrading factors that are not included in our analysis. These include the effects of straylight, of all other low-order optical aberrations apart from defocus, and of the readout electronics (such as transfer efficiency and pixel-to-pixel crosstalk), which reduce the contrast, but are difficult to model reliably. To illustrate the extreme sensitivity of the granulation contrast to low-order aberrations and straylight we calculated, as an example, in ZEMAX the effect of astigmatism and coma, which were equally distributed in such a way that the total system shows an rms wave-front error of 0.044 wavelengths. This corresponds to the number given by Suematsu et al. (2008) and represents a system with a remarkable Strehl ratio of 0.93. This small effect is nevertheless sufficient to reduce further the contrast from 8.5% to 8.1% in optimal focus position. If no further degrading effects are present, a straylight level of only 4.7% would be sufficient to bring the contrast down to the observed value of 7.8% (for optimal focus), and to 7.0% for the presumptive defocus value of the dataset studied here, respectively.

3.5 Conclusion

We find that consideration of the basic optical properties of the *Hinode* SOT/SP system and a slight defocus are sufficient to bring the degraded contrast of a 3D radiative MHD simulation and the observed rms continuum contrast at 630 nm, almost into agreement. The remaining discrepancy can be ascribed to the combined, minor effects of straylight, other low-order optical aberrations, and instrument electronics. Hence, Hinode SP data are consistent with a granulation contrast at 630 nm of 14-15%, as predicted by the simulations.

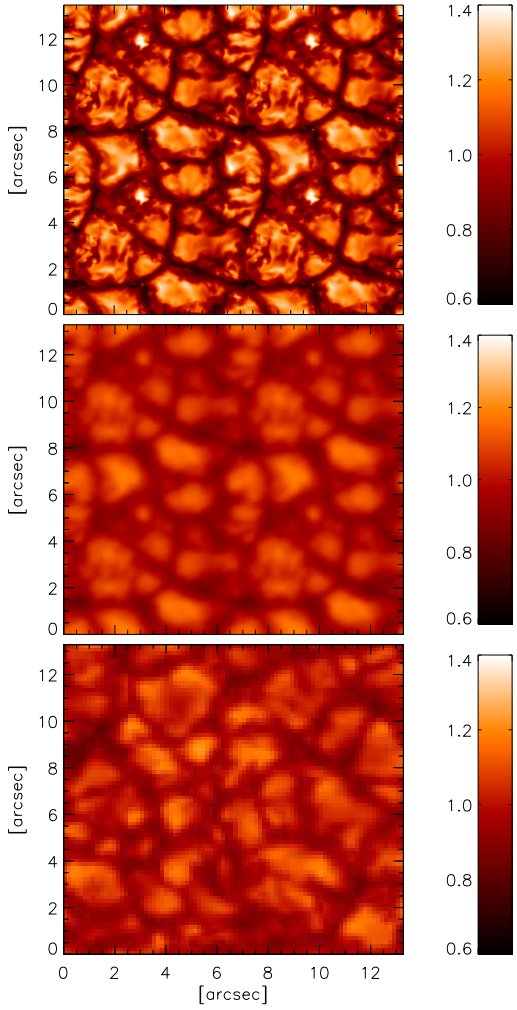

Figure 3.4: Continuum images at 630 nm from the simulation snapshot with original resolution *(top)* and after degrading *(middle)*, in comparison with a detail of the observed Hinode/SP map of the same size *(bottom)*. The periodic simulation box is shown fourfold for better visibility.

4 Quiet Sun Magnetism

4.1 Introduction

The origin of the small scale magnetic flux found in the quiet Sun is uncertain (de Wijn et al. 2009). The estimated order of magnitude for the magnetic Reynolds number of the granulation flow indicates that a substantial part of the magnetic field in the quiet Sun could be generated locally through dynamo action driven by near-surface convective flows (Petrovay & Szakaly 1993, Cattaneo 1999, Vögler & Schüssler 2007). The simulations imply that magnetic field could be organized in mixed polarity structures down to very small spatial scales. The simulations exhibit a mostly horizontal field in the photospheric layers in the form of low lying loops connecting nearby opposite polarities (Schüssler & Vögler 2008).

Substantial observational evidence has been gathered that internetwork flux is dominated by strongly inclined, almost horizontal magnetic fields (Orozco Suárez et al. 2007b,c, Lites et al. 2008). Several authors report on loop-like horizontal field structures of different sizes (Martin 1988, Martínez González et al. 2007, Harvey et al. 2007, Centeno et al. 2007, Ishikawa et al. 2008). Not all of them are necessarily related to local dynamo action. Such structures could appear due to small-scale flux emergence (Cheung et al. 2008) or flux expulsion of a pre-existing field by granular flows (Steiner et al. 2008). Also, the observed ratio of the horizontal and vertical magnetic flux densities (Lites et al. 2008) could be explained with (Schüssler & Vögler 2008) or without local dynamo action (Steiner et al. 2008).

Another open question concerns the amount of magnetic flux contained in the internetwork. The observations give a wide range of values depending on the spatial resolution and the diagnostic technique used (e.g, Domínguez Cerdeña et al. (2003), Khomenko et al. (2003), Berdyugina & Fluri (2004), Asensio Ramos et al. (2007)). From many results obtained (de Wijn et al. 2009), we mention here only a few which directly concern the work presented in this chapter. Comparing the center-to-limb observations of the scattering polarization in the Sr I 4607 Å line with the signal synthesized from the 3D hydrodynamical simulations, Trujillo Bueno et al. (2004) inferred that the mean strength of the internetwork field is $\langle B \rangle \sim 100$ G, with the assumption that the magnetic field is tangled at subresolution scales and that it fills the whole resolution element. Khomenko et al. (2005a), on the other hand, compared the observed Stokes V amplitudes of the visible and infrared Fe I lines with the profiles synthesized from 3D radiative MHD simulations, and concluded that $\langle B \rangle \sim 20$ G. Sánchez Almeida et al. (2003) used Boussinesq 3D simulations of local dynamo action to suggest that a snapshot with average magnetic flux density of 50 G can reproduce both the observed Hanle and Zeeman signals. However,

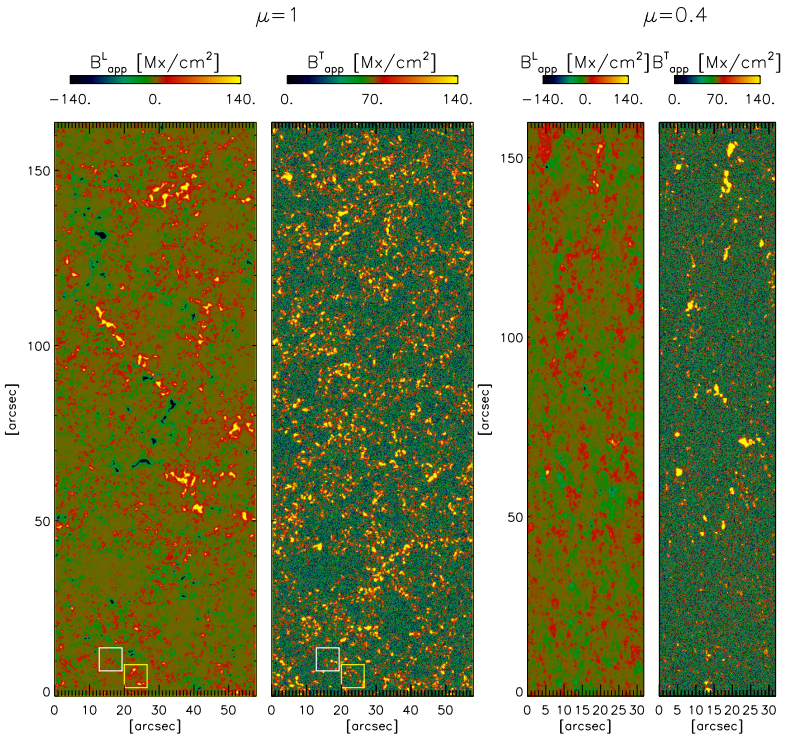

Figure 4.1: Maps of longitudinal (B^L_{app}) and transversal (B^T_{app}) apparent flux density for data set I (left) and III (right) from Table 4.2. The small squares indicate the sizes of the MHD snapshots. They also mark the position of the regions to which synthesized maps are compared (Figures 4.4 and 4.5)

the simulations used by these authors are somewhat idealized and the solar atmospheric structure is arbitrarily introduced for comparison with the observational data.

In this chapter, we use the radiative MHD simulations of the solar photosphere to obtain insight into the role of the local dynamo action for the quiet Sun magnetism by comparing the synthesized polarization signals with the ones observed with the spectropolarimeter (Lites et al. 2001) of the Solar Optical telescope (Tsuneta et al. 2008a) on board of the Hinode satellite (Kosugi et al. 2007).

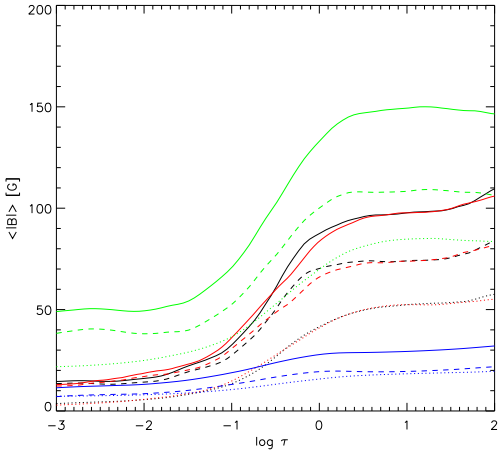

Figure 4.2: A comparison of the averaged total (solid), horizontal (dashed) and vertical (dotted) mean magnetic field strength as a function of the optical depth. Snapshots from different runs are indicated by different colors: blue: mixed polarity, red: dynamo G, black: dynamo C multiplied by factor of 1.5 and green: dynamo C with background unipolar field.

4.2 Observations

We consider three data sets obtained with the spectropolarimeter (SP) on board Hinode. Details are given in Table 4.2. Data sets I and II were recorded around disc center, while data set III was obtained closer to the limb. Data sets I and III are obtained in the scan mode of the *Hinode* SP, with an exposure time of 9.6 s per slit position. They cover 'quiet' Sun regions at the disk center and the region near the south solar pole, respectively. In the case of data set III, we use a 32″ wide stripe perpendicular to the scan direction that corresponds to $\mu = 0.4$ (μ being the cosine of the heliocentric angle). Corrections for various instrumental effects are made using the procedure sp_prep, included in the SolarSoft[1] package. The procedure gives longitudinal and transversal magnetic flux density maps (Lites et al. 2008) shown in Fig 4.1. The rms continuum contrast values for data sets I and III are 7.5% and 5.1% respectively.

Data set II is a time series recorded with fixed slit position. It consists of 103 scans at solar disk center, each with an exposure time of 9.6 s. After applying a temporal running mean, the effective exposure time becomes 67.2 s, which gives a significantly lower level of noise. This data set has previously been used by Lites et al. (2008) and Orozco Suárez et al. (2007c).

[1] http://www.lmsal.com/solarsoft/

Table 4.1: The simulation parameters. The size of computational domain and vertical δz and horizontal δx grid spacing.

Run	$height/width$ $[Mm]$	$\delta z/\delta x$ $[km]$	R_m
mixed polarity	1.4/6.0	14/20.8	~ 300
dynamo C	1.4/4.86	10/7.5	~ 2600
dynamo G	1.4/4.86	7/5	~ 5200

4.3 Simulation data

We use 3D radiative MHD simulations of a layer containing the solar surface, carried out with the MURAM code (Vögler 2003, Vögler et al. 2005). Non-grey LTE radiative transfer and partial ionization are taken into account. We compare snapshots from several simulation runs. The basic characteristics of the computational domains are given in Table 4.1. In all runs, the height of the simulation box is 1400 km, of which roughly 500 km is above the level of optical depth $\tau = 1$. Side boundaries are periodic, whereas the bottom boundary is open permitting free in and outflow of matter. The magnetic field is vertical at the top and bottom boundaries (Vögler et al. 2005).

The first run, from here on called the 'mixed polarity' run, simulates the decay of the magnetic field in a mixed polarity region. In this case, local dynamo action (Vögler & Schüssler 2007) does not occur since the magnetic Reynolds number is below the threshold for dynamo action. The run starts with a vertical magnetic field of $\langle|B|\rangle = 200$ G, in a checkerboard-like 2×2 pattern, with opposite polarities in adjacent parts. The field is concentrated and redistributed by the convective motions; the opposite polarities are pushed together which results in a cancellation and almost exponential decrease of the mean magnetic field strength. The snapshots with $\langle|B|\rangle = 35$ G and $\langle|B|\rangle = 20$ G at $\tau = 0.1$ are used in our study. The same snapshots were used by Khomenko et al. (2005a,b).

The second and third group of snapshots are taken from the runs where the magnetic Reynolds number of the flow is sufficiently high for small-scale dynamo action to take place. A seed field of $|B_0| = 10$ mG is amplified exponentially in time until the saturation level is reached. In the dynamo run C, described in Vögler & Schüssler (2007), the mean magnetic field strength at this phase is $\langle|B|\rangle = 23$ G at $\tau = 0.1$. In the case of the dynamo run G, the higher magnetic Reynolds number leads to a saturation level of the magnetic energy which is a factor of ~ 1.7 higher than in run C. Figure 4.2 shows the mean magnetic field strength (averaged over surfaces of constant τ) as a function of the optical depth for of the snapshots from each run. The field in the snapshot from dynamo C run is multiplied by a factor 1.5, in order to illustrate the similarity of the optical depth profiles in the dynamo runs. The dashed lines show the optical depth profiles of the horizontal magnetic field, i.e., $\langle B_{hor}\rangle = \langle \sqrt{B_x^2 + B_y^2}\rangle$ and the dotted lines represent the average vertical field $\langle|B_{vert}|\rangle$. Both runs show a significantly larger $\langle B_{hor}\rangle$ than $\langle|B_{vert}|\rangle$. Their ratio reaches values between 2 and 4 in the optical depth interval $0.2 < \tau < 0.1$ for the snapshots shown. The mixed polarity snapshot, on the other hand, has a $\langle B_{hor}\rangle$ and $\langle|B_{vert}|\rangle$ of similar magnitude over all heights.

Table 4.2: Details of the three Hinode/SP data sets used. The last three columns, from left to right, give the mean values of the transversal (with respect to the line of sight), unsigned longitudinal, and signed longitudinal magnetic flux density, respectively.

	date [dd/mm/yy]	time UT	FOCUS	μ	size [arcsec]	exposure time [s]	noise $10^{-3} I_c$	$\langle B^T_{app} \rangle$ Mx/cm^2	$\langle \lvert B^L_{app} \rvert \rangle$ Mx/cm^2	$\langle B^L_{app} \rangle$ Mx/cm^2
set I	10/09/07	08:00:00	2031	1	58×164	9.6	0.8	56.7	9.7	1.6
set II	27/02/07	00:20:09	2048	1	0.16×164	67.2	0.25	54.6	11.0	1.7
set III	09/09/07	13:05:05	2029	0.4	160×32	9.6	1	53.5	6.8	0.3

Table 4.3: Mean apparent magnetic flux densities from observations and simulations. The values in parentheses are the mean values at the original resolution of the simulations, before spatial smearing, and addition of noise.

Run	$\langle B^T_{app} \rangle$	$\langle \lvert B^L_{app} \rvert \rangle$	$\langle B^L_{app} \rangle$	$\langle B^T_{app} \rangle / \langle \lvert B^L_{app} \rvert \rangle$
observations	55	6	-2	9.2
mixed polarity (30 G)	39 (24)	13 (19)	−0.2 (−0.3)	3.0 (1.2)
mixed polarity (20 G)	37 (15)	6.5 (9.0)	−0.6 (−0.3)	5.7 (1.8)
dynamo C	36-37 (21-28)	2.7-3.0 (6.4-7.8)	−0.1 – 0.0 (−0.2 – 0.0)	12-13 (3.3-3.6)
dynamo C (+uni. field)	45-51 (51-65)	9-15 (18-27)	9-14 (9-16)	3.4-5 (2.4-2.8)
dynamo G	39 (39)	3.0 (9.6)	0.1 (0.1)	13 (4.1)
noise	36	2.3	0.0	
dynamo C ($mf = 3$)	51-60 (70-81)	5.3-6.0 (19-24)	−0.1 – 0.0 (−0.1 – 0.0)	9.6-10 (3.4-3.7)
dynamo G ($mf = 2$)	52 (77)	4.7 (19)	0.2 (0.2)	11 (4.0)

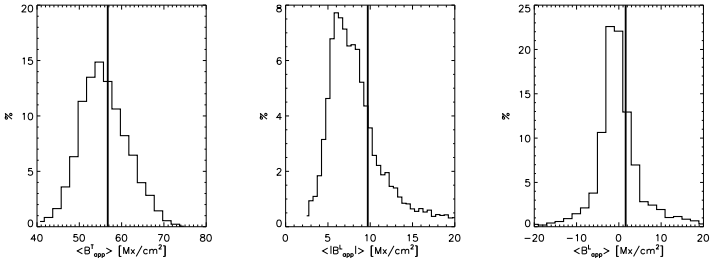

Figure 4.3: Histograms of the mean horizontal (left), the unsigned vertical (middle) and the signed vertical (right) magnetic flux density calculated for $7'' \times 7''$ size regions covered by dataset I. The vertical lines mark the mean values for the whole field of view.

The last group of snapshots is taken from a simulation run that continues dynamo run C with a superposed unipolar vertical field. The mean magnetic field strength profiles with the optical depth of a representative snapshot in this group are shown in Figure 4.2 by green lines. The mean vertical field strength increased to around 36 G at $\tau = 0.1$ and the strength of the horizontal field to around 50 G at $\tau = 0.1$.

4.4 Spectral synthesis

The physical parameters of every pixel are used as an input for the LTE radiative transfer code SPINOR (Frutiger et al. 2000), to synthesize the Stokes profiles for the heliocentric angles $\theta = 0^o$ and 66^o (corresponding to $\mu = 1$ and $\mu = 0.4$, respectively). The spectral range that contains the Fe I lines 630.15 and 630.25 nm is sampled in steps of 7.5 mÅ. The Fe abundance used in the synthesis has been taken from Thevenin (1989) and the values of the oscillator strengths, from the VALD database (Piskunov et al. 1995). We then applied a realistic point spread function PSF (Danilovic et al. 2008) to the maps of synthesized Stokes profiles. The PSF takes into account the basic optical properties of the Hinode SOT/SP system and a small defocus. Applying an ideal PSF without defocus reduces the original rms contrast values of the simulated continuum map from 14.5% to 8.5 % ($\theta = 0^o$) and 11.2% to 5.5% ($\theta = 66^o$), respectively. For the comparison with the observations at $\theta = 0^o$, we used a defocus of -1.5 mm, which degrades the continuum contrast of the simulation to the observed value of 7.5%. A value of -0.75 mm is used for the synthesized data at $\theta = 66^o$ in order to match the continuum contrast of 5.1% deduced from dataset III. The difference in the focus of the SOT between data sets I and III amounts to approximately 2 steps of the SOT focus mechanism. Taking into account that there is an uncertainty of one focus step in the focusing mechanism, the amounts of defocus obtained from reproducing the observed data sets seem plausible.

The appropriate PSF is applied to the 2D maps at each wavelength position for every Stokes parameter and then rebinned to the pixel size of the Hinode/SP detector. To take into account the spectral resolution of the spectropolarimeter, the profiles are convolved with a Gaussian function of 25 mÅ FWHM and resampled to a wavelength spacing of

21.5 mÅ. Next, a noise level corresponding to the observations is added, and finally the procedure by Lites et al. (2008) is used to calculate the longitudinal and transversal apparent magnetic flux densities, B^L_{app} and B^T_{app}.

4.5 Results

The results are organized as follows: (1) snapshots from the different simulation runs are compared with the disc center observations in terms of the mean values of B^L_{app} and B^T_{app}, (2) the spatial distributions of the magnetic features in the observed and in the synthesized maps are compared, (3) a comparison in terms of the probability distribution functions (PDFs) from the simulations and the low-noise data set II is presented. Finally we compare the synthesized and observed signal at a heliocentric angle of $\theta = 66^o$.

4.5.1 Comparison with the observations at disc center

Before comparing the observational signals with the ones synthesized from the simulations, one has to take into account the proportion of the solar surface covered by the observations of data set I and the one comprised by the simulations. The small squares in Fig 4.1 indicate the actual size of the simulation snapshots. In order to take into account this proportion, we divide the region covered by the observations into subdomains of $7'' \times 7''$ size. For each of these we calculate the mean transversal $\langle B^T_{app} \rangle$, the mean unsigned longitudinal $\langle |B^L_{app}| \rangle$ and the mean signed longitudinal $\langle B^L_{app} \rangle$ apparent magnetic flux densities. The histograms of these quantities are shown in Fig 4.3. By considering the contribution of each subdomain separately, we can exclude the contribution of the network, which is visible in the B^L_{app} map of Fig 4.1 as yellow and black patches. The maxima of the distributions give an estimate of the typical magnetic flux density value in the internetwork regions. The network extends the wings of the histograms towards higher values of $\langle B^T_{app} \rangle$ and $\langle |B^L_{app}| \rangle$. Consequently, when the whole observed region is taken into account, the mean values (marked by the vertical lines in Fig 4.3) are higher than the values retrieved from the maxima. The mean values over the whole FOV are in agreement with the values obtained by Lites et al. (2008) and show a ratio of $\langle B^T_{app} \rangle / \langle |B^L_{app}| \rangle = 5.8$.

The values retrieved from the distribution maxima are presented in the first row of Table 4.3. The other data are the results obtained from the synthesized Stokes profiles from the simulation snapshots. The mean apparent flux density values calculated from the snapshots at their original resolution are shown in the parenthesis. They roughly correspond to the mean vertical and horizontal field strengths near the optical depth level of $\tau = 0.1$ (cf. Figure 4.2). Thus, the ratio $\langle B^T_{app} \rangle / \langle B^L_{app} \rangle$ obtained from the simulations at the original resolution reflects the ratio of the underlying magnetic fields. The values are ~ 1 for the mixed-polarity run and ~ 3 for the dynamo snapshots. The apparent flux densities obtained after the application of spatial smearing and addition of noise are given outside the parentheses. For the dynamo snapshots, the $\langle |B^L_{app}| \rangle$ is considerably reduced compared to the noise-free, unsmeared case owing to the presence of mixed polarities on very small scales. On the other hand, the $\langle B^T_{app} \rangle$ are increased for all groups of snapshots, except for the dynamo C run with unipolar background field. This is the result of the noise which is added to the Stokes profiles in order to simulate the Hinode/SP observations.

Third row from the bottom in Table 4.3 gives $\langle B_{app} \rangle$ values determined from pure white noise with a standard deviation corresponding to the noise level of data set I. We calculated the mean values from 100 realizations. The value of $\langle B^T_{app} \rangle$ determined from the noise is almost as large as the values retreived from the snapshots, with the exception of the dynamo C run with a unipolar background field. This means that hardly any signal of B^T_{app} remained above the noise after spatial smearing and introduction of noise. Dynamo C run with a unipolar field is special because it has a much higher mean field (cf. Figure 4.2). The more magnetic flux is introduced, the more field can be tangled by the turbulent flows, hence noticeably more horizontal field is generated.

The last two rows of the Table 4.3 show the results of the attempt to estimate how much field the dynamo simulations would have to contain, so that the observed $\langle B_{app} \rangle$ values would be reproduced. Multiplying the magnetic field strengths by factors $f = 2$ and $f = 3$ in the case of the dynamo run G and dynamo run C, respectively, gives a mean total magnetic field strength of ≈ 170 G and $66 - 67$ G at the levels of $\tau = 1$ and $\tau = 0.1$, respectively. The strength of the mean vertical magnetic field at the same levels becomes 84 G and 27 G, respectively. The average mean field strength distribution of the run G can be reproduced by multiplying the run C result by a factor $\approx (E_{max}(G)/E_{max}(C))^{1/2}$. This suggests that such a simple scaling might be valid also somewhat into the R_m regime that is not covered by the simulations.

Figure 4.4 shows one snapshot from the dynamo run C with the field multiplied by a factor of 3, before and after the spatial smearing, together with a region on the Sun of the same size, outlined by the white square in Fig 4.1. Maps of the longitudinal and transversal magnetic flux density are shown with the outlined granular pattern (white lines mark the contours of normalized continuum intensity equal to 1.05). Vertical fields with the mixed polarities, on scales of less then an arcsec are smeared into the unipolar 'flux tube' or the 'flux sheet' shaped patches after the spatial smearing. The bundles of horizontal field, composed of loops of different sizes, are molded into the patches with higher B^T_{app} values. These can occur on the edges of the granules or between the patches with vertical field of opposite polarity that look like footpoints of the loop (see for instance the feature at $[4.5'', 2'']$). Similar features are visible in the Hinode maps (see also Ishikawa et al. (2008) or Lites et al. (2008)). At the position $[5'', 3.5'']$, a vertical field of $B^L_{app} \approx 20$ Mx/cm^2 is visible inside a granule. A similar case has been observed by Orozco Suárez et al. (2008).

Figure 4.5 shows another region on the Sun (outlined by the yellow square in Fig 4.1) compared with a snapshot from the dynamo run with a unipolar background field. No multiplication of the dynamo field has been carried out here. The maps based on the simulation show features which are very similar to the structures present in the weak network region, although the signal is weaker than in the observations. Small patches of horizontal field correspond to structures of small loops at original resolution between concentrations of the vertical flux.

4.5.2 Comparison with the data set II

Pietarila Graham et al. (2009) demonstrated how different effects can influence the PDF of magnetic field derived from Stokes V spectra, such that it differs from the PDF of the underlying magnetic field. In particular, the effect of noise leads to a PDF which has a

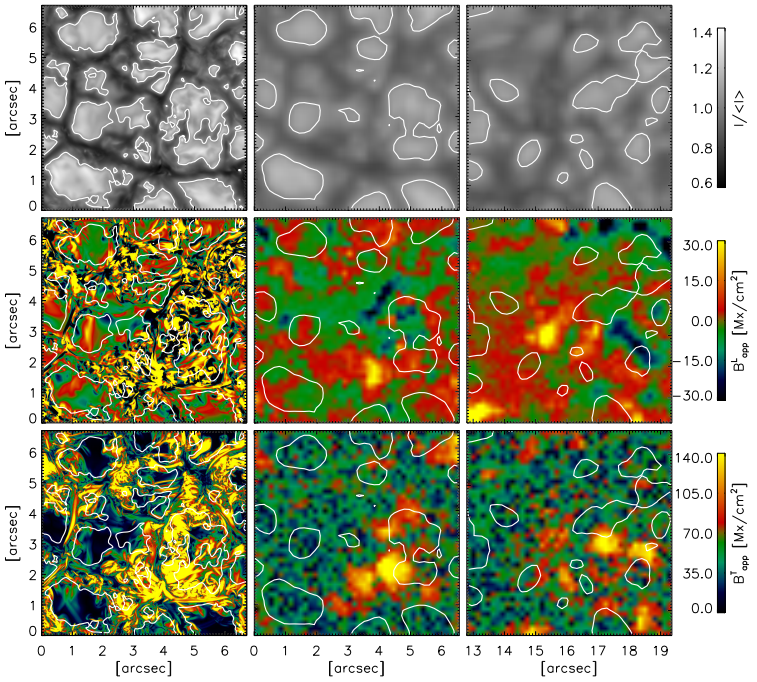

Figure 4.4: Comparison of a snapshot from dynamo run C with $f = 3$ at original (left column) and Hinode (middle column) resolution, with Hinode observations (right column). *From top to bottom*: normalized intensity, longitudinal and transversal apparent magnetic flux density. The plotted observed region is outlined by a white square in Fig 4.1.

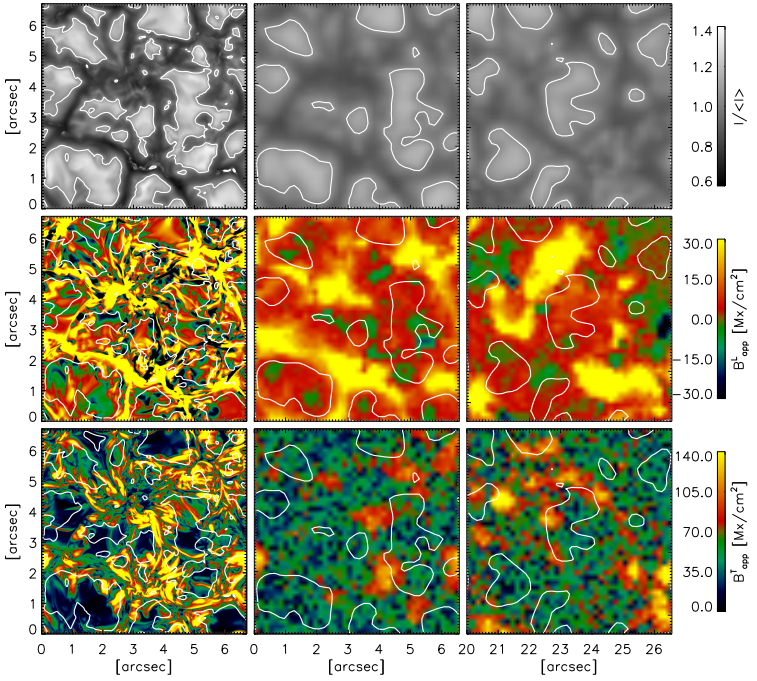

Figure 4.5: Comparison of a snapshot from the dynamo run C with a background unipolar field at original (left column) and Hinode (middle column) resolution, with Hinode observations (right column). *From top to bottom*: normalized intensity, longitudinal and transversal apparent magnetic flux density. The plotted observed region is outlined by a yellow square in Fig 4.1.

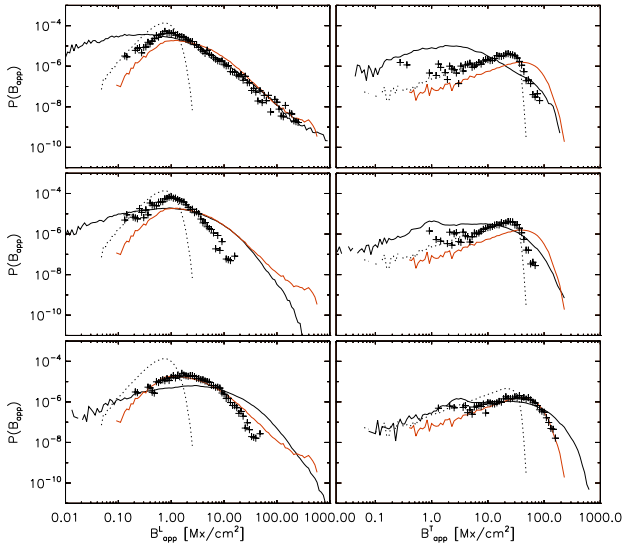

Figure 4.6: Probability distribution function (PDFs) for the longitudinal (left column) and transversal (right column) apparent magnetic flux density. PDFs from synthetic B_{app} at original (solid) and Hinode (crosses) resolution are compared with the observed PDFs of B_{app} (red solid line). *From top to bottom*: mixed polarity snapshot (20 G), snapshot from the dynamo run C and the same snapshot with the field multiplied by a factor 3. Also shown are the PDFs of pure white noise with a standard deviation of 3×10^{-4} (dotted lines).

peak at the position that corresponds to the level of noise introduced. Here we compare the PDFs of the B^L_{app} and B^T_{app} determined form the synthesized Stokes profiles with the observed ones. Figure 4.6 shows PDFs computed for a snapshot from the dynamo run C, with and without multiplication by a factor of 3, together with the mixed polarity (20 G) snapshot. Overplotted are the results calculated from pure noise with a standard deviation corresponding to the noise level of the observations.

The figure shows that all the PDFs from the snapshots at Hinode resolution are strongly influenced by the noise at the smallest field strengths, similar to the PDF based on the Hinode data. The noise-induced maxima lie at approximately $B^L_{app} \sim 1$ G and $B^T_{app} \sim 20$ G. On the other hand, the tails of the distributions are different. After the spatial smearing, only the mixed-polarity simulation snapshot retains a considerable amount of the strong vertical field that matches the network fields shown by the observations. The signature of the horizontal field is lost in the noise for both, the mixed-polarity snapshots and also for the snapshot from the dynamo run C. Only a small percentage of the pixels show a B^T_{app} signal above the noise level. However, if one multiplies the original field values by a factor 3, the PDF (in the bottom row of the Fig. 4.6) of the B^T_{app} agrees well with the

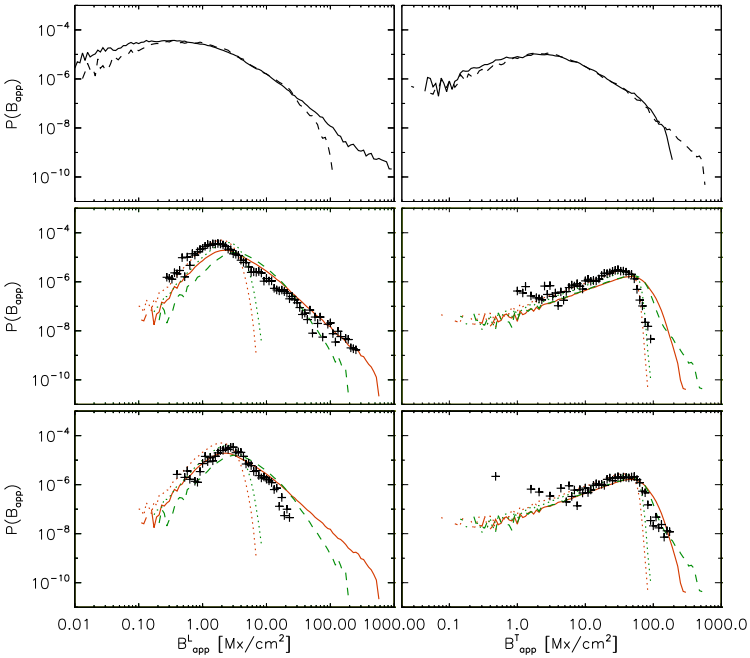

Figure 4.7: PDFs for the longitudinal (left column) and transversal (right column) apparent magnetic flux density. Top panels show the B_{app} synthesized from mixed-polarity run (20 G) at original resolution for the heliocentric angles $\theta = 0^o$ (solid) and $\theta = 66^o$ (dashed). Comparison of synthetic B_{app} at Hinode resolution (crosses) with observations at heliocentric angles $\theta = 0^o$ and $\theta = 66^o$ is shown in middle and bottom rows respectively. Red solid line marks the observational B_{app} at $\theta = 0^o$ and green dashed line, the observations at $\theta = 66^o$. In the same colors, in dotted lines, the PDFs of the corresponding noise are shown.

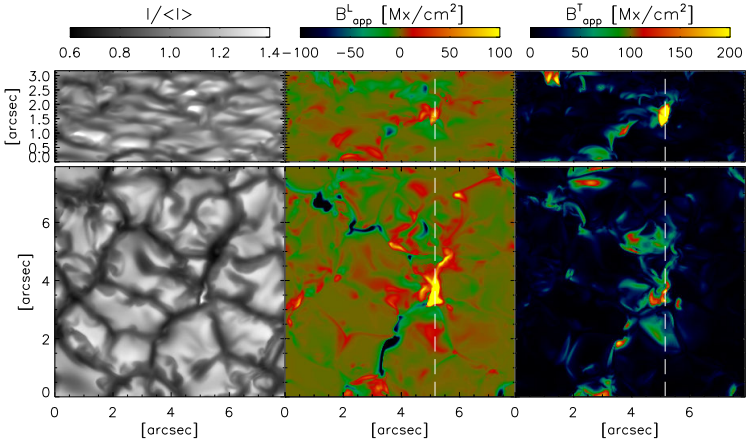

Figure 4.8: Apparent flux densities at the disc center (lower panels) and at $\mu = 0.4$ (upper panels) for a mixed-polarity (20 G) snapshot. From left to right: normalized continuum intensity, longitudinal and transversal apparent flux density.

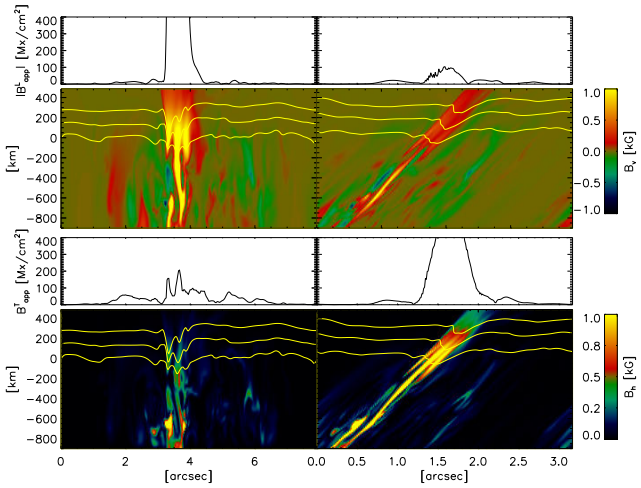

Figure 4.9: Vertical cut through the strong vertical field feature in Fig 4.8 (position is marked by the white dashed lines). Longitudinal (second row) and transversal (bottom row) field at disc center (left panels) and at $\mu = 0.4$ (right panels) and corresponding values of the longitudinal (top row) and transversal (third row) apparent flux density as determined from synthetic Stokes profiles.

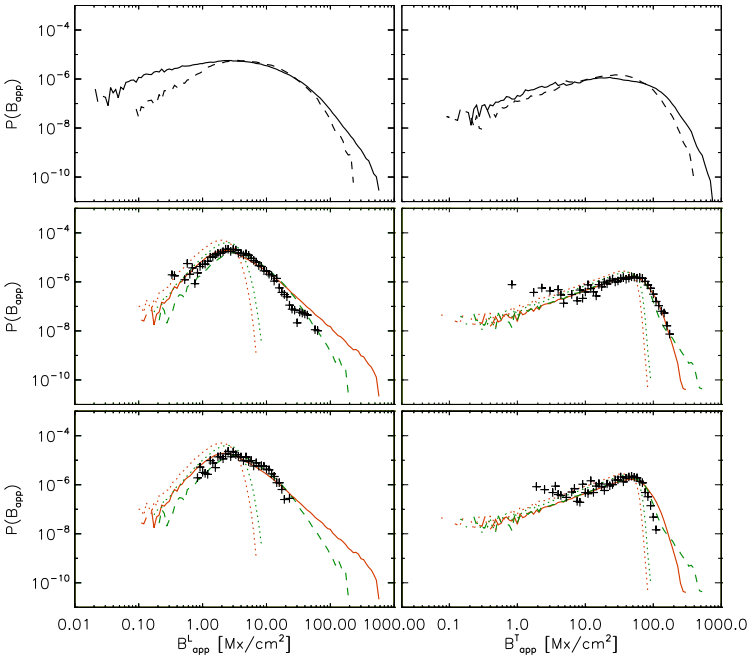

Figure 4.10: The same as in Fig 4.7, but for a snapshot from the dynamo run C with $f = 3$.

observed one. There are a small discrepancies at the smallest signals which is result of the poor sampling (a consequence of the very small region covered by the simulations). The synthesized distribution of B^L_{app} follows the observed distribution up to approximately 10 Mx/cm^2 when the occurrence of pixels with signals higher than this starts to decrease rapidly. Pixels with B^L_{app} signals higher than 40 Mx/cm^2 are very rare for the maps resulting from dynamo run.

4.5.3 Comparison with observations at $\mu = 0.4$ ($\theta = 66^o$)

The change in the apparent magnetic flux density at different heliocentric angle is illustrated by using the examples from snapshots taken from the mixed-polarity run (20G) and the dynamo run C. The magnetic field strength in the dynamo snapshot is multiplied by a factor of 3 in keeping with the findings from the previous sections.

Figure 4.7 shows the PDFs of the field proxies (B^L_{app} and B^T_{app}), for the mixed polarity snapshot at the heliocentric angles $\theta = 0^o$ and $\theta = 66^o$. The top panels show the PDFs obtained at the original resolution. The distribution at $\theta = 0^o$ indicates more frequent occurrence of the weak signals, $B_{app} \leq 1$ Mx/cm^2 compared to the distribution at $\theta = 66^o$. These signals originate in the regions above granules, where the field strengths are of or-

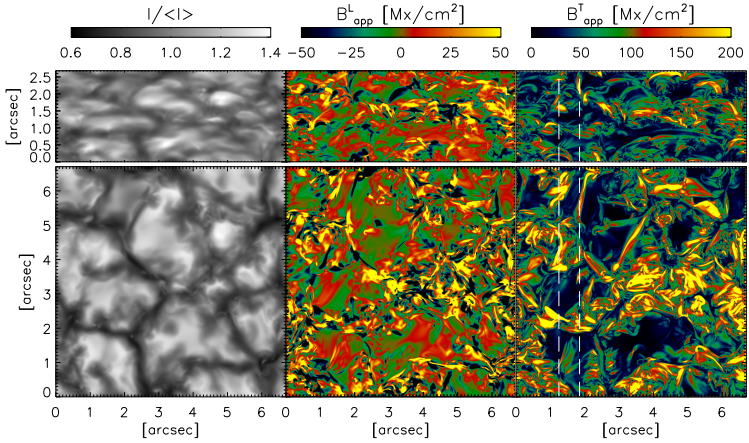

Figure 4.11: Apparent flux densities at disc center (lower panels) and at $\mu = 0.4$ (upper panels) for a snapshot from the dynamo run C ($f = 3$). From left to right: normalized continuum intensity, longitudinal and transversal apparent flux density.

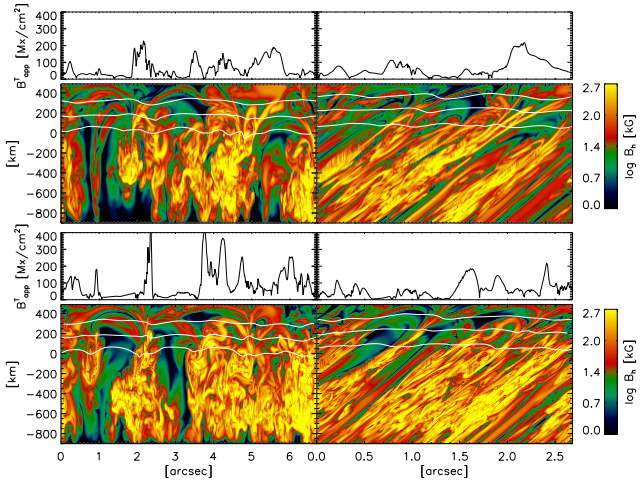

Figure 4.12: Vertical cuts through the the strong horizontal features in Fig 4.11 (position marked by the white dashed lines). Transversal (second and bottom row) field at the disc center (left panels) and at $\mu = 0.4$ (right panels) and corresponding values of the transversal (top and third row) apparent flux density as determined from synthetic Stokes profiles.

der of 1 G and less. The inclined view results in foreshortening of these regions and the contribution from the surrounding regions (with the higher magnetic fields strengths) to the magnetic field profile along the line of sight. Hence the occurrence of weak signals is lower at $\theta = 66^o$. The tails of the distributions, on the other hand, show a different behavior. The probability of occurrence of the $|B^L_{app}| > 100$ Mx/cm^2 signals decreases at $\theta = 66°$, while the probability of occurrence of $B^T_{app} > 100$ Mx/cm^2 signals increases. This effect results from the strong magnetic concentrations, as illustrated in Fig. 4.8 and Fig. 4.9. Figure 4.8 shows apparent magnetic flux density maps obtained from the synthesized Stokes profiles. The strong magnetic features located at $[5'', 3.5'']$ and $[1'', 7'']$ produce strong B^L_{app} signals at $\theta = 0^o$. Weak canopy-like structures are visible in B^T_{app} in their vicinity. At $\theta = 66^o$, these features are almost indistinguishable from the surroundings in the B^L_{app} map, but show strong B^T_{app} signals. The vertical cuts through one of them are shown in Fig. 4.9 at both heliocentric angles. The positions of the cuts are marked by the white dashed lines in Fig. 4.8. The change in the B_{app} occurs when a strong magnetic tube-like structure with a vertical field of kG strength is observed from the side. Projected on to the line of sight, the strong vertical component of magnetic field gives rise to a significant transversal component, leading to a strong B^T_{app} signal.

The lower panels of Fig. 4.7 present PDFs from the observations and from the mixed polarity (20 G) simulation snapshot at reduced resolution, for both heliocentric angles. The tails of the distributions towards large values obtained from the observations exhibit the same behavior as the distributions from the simulation at original resolution. The same is true at reduced resolution. The occurrence of the $B^T_{app} > 200$ Mx/cm^2 at $\theta = 66^o$ is significantly higher with respect to the case at $\theta = 0^o$. Hence the patches of the strong transverse field visible in the maps at $\theta = 66^o$ shown in Fig 4.1, mark the positions of the strong radially oriented field concentrations. Tsuneta et al. (2008b) report a similar effect.

The peaks at the low end of the PDFs at different heliocentric angles are displaced with respect to each other due to the difference in the noise level (shown in dotted lines) introduced to match the observations.

Figure 4.10 shows the PDFs of B^L_{app} and B^T_{app} derived from a dynamo run C snapshot (with $f = 3$). Although the ratio between the averaged horizontal and vertical field components is significantly higher than in the mixed-polarity case, the trend of the PDFs is not much different, except at the highest values. As discussed by Lites et al. (2008), a noticeable increase in $\langle|B^L_{app}|\rangle$ away from the disk center should be expected, but even at the original resolution and with no noise introduced no such effect is observed. There is a drop in both $\langle|B^L_{app}|\rangle$ and $\langle B^T_{app}\rangle$ by 20% and 30% respectively, from $\theta = 0^o$ to $\theta = 66^o$. The apparent field maps in Fig. 4.11 show that the transformation from strong B^T_{app} to strong $|B^L_{app}|$ signals does occur (for example in the case of the loop crossing the granule at $[3'', 4.5'']$), but more $|B^L_{app}|$ seems to be lost than is compensated by the projection of the horizontal field into the line of sight.

It was also suggested by Lites et al. (2008) that there should be a difference in the trend of $\langle B^T_{app}\rangle$ for the loops oriented east-west and the ones oriented north-south. If we separate the contributions of the pixels with field azimuth $\phi_r < 5^o$, and pixels with azimuth $\phi_r > 85^o$ we get a decrease in $\langle B^T_{app}\rangle$ of 34% in the first case and of 30% in the second, for this particular snapshot. Figure 4.12 shows cuts through a few of the loops oriented in both directions. The lower panels correspond to the position of the dashed line on the left in Fig. 4.11. The cut goes through several almost east-west oriented loops, at

$y \simeq 0.2'', 2.3'', 3.8''$ and $6''$ and one oriented north-south near $y \simeq 4''$. The cut marked by the right dashed line in Fig. 4.11 corresponds to the upper panels in Fig. 4.12 and goes through the two north-south oriented loops at around $y \simeq 2'', 6''$ and several small loops in the east-west direction. When observed from the side, the loops oriented along the cut leave a B^T_{app} signature that corresponds to the position of a small portion of the loop on the side towards the observer. The same is valid for the loops perpendicular to the cuts. Owing to the inclined line of sight, the strength of the horizontal component of the field is reduced. Only the location where the transversal field strength reaches a few hundred G at an optical depth range of $\tau = 0 - 0.01$, does a significant B^T_{app} signature appear.

The lower panels of Fig. 4.10 show the PDFs retrieved from the dynamo snapshot at Hinode resolution. Their trends correspond to the ones at original resolution. The synthesized PDF of the B^T_{app} signal follows the observations at both heliocentric angles up to $B^T_{app} \approx 200$ Mx/cm^2.

4.6 Discussion

In order to see whether traces of local dynamo action can be found in the quiet Sun we compare realistic MHD simulations with Hinode/SP data. We chose representative snapshots from several simulation runs. Taking into account the instrumental effects, we reduced the spatial resolution of simulations to match the Hinode observations. Then, magnetic proxies, the longitudinal and transversal apparent magnetic flux density introduced by Lites et al. (2008), are calculated from the synthesized Stokes profiles after reducing the spatial resolution to the Hinode value and adding an appropriate level of noise. The obtained values were compared with observations of the internetwork region, excluding the contribution of network. The mixed polarity simulations (which have a magnetic Reynolds number below the threshold for dynamo action) reproduce the observed vertical flux density, as was previously shown by Khomenko et al. (2005a). However, they do not contain enough horizontal field, to be consistent with the Hinode data. Simulations of surface dynamo give a ratio of the horizontal to the vertical flux density consistent with the observational results (Schüssler & Vögler 2008), but the overall amplitudes are too low. Computations with increasingly higher values of the magnetic Reynolds number give larger magnetic energies. The agreement with the data strongly supports the action of a local dynamo in the quiet Sun. A local dynamo simulation running in a region with additional unipolar flux reproduces many of the characteristics of a network region. This indicates that the network has a different source from internetwork, a conclusion supported by studies of ephemeral active regions (Harvey 1993, Hagenaar 2001).

A simple multiplication of the field in the simulation domain by a fixed factor brings the magnetic flux density from the dynamo snapshots at Hinode resolution close to the observed ones. The justification for this procedure comes from simulations with a highest magnetic Reynolds number that are feasible at the moment and on the basis of the comparison with the observation with a different level of noise. The retrieved mean magnetic field strength is of the order of 70 G at $\tau = 0.1$ and around 170 G at the solar surface. This is roughly in agreement with the estimations given by Trujillo Bueno et al. (2004) since the line they consider samples the middle photosphere. The comparison with simulations with higher magnetic Reynolds numbers, based on the cancellation coefficient (Pietarila

Graham et al. 2009) already indicates that the numbers presented here must be considered a lower limit.

The spatial distribution of the horizontal and vertical features after spatial smearing is consistent with the observations. The small scale mixed-polarity fields at the original resolution are molded into the unipolar structures with a weak vertical field. Bundles of low-lying loops are smeared into patches of horizontal field at the edges of granules, as observed (Lites et al. 2008, Ishikawa et al. 2008). One of the synthesized Hinode maps also displays a weak vertical field inside the granule as observed Orozco Suárez et al. (2008).

The interpretation of the results for the center-to-limb behavior is more difficult. We showed that the contribution of the surface dynamo dominates in the regions that show $|B^L_{app}| < 20-30$ Mx/cm^2 and $B^T_{app} < 200$ Mx/cm^2 at Hinode spatial resolution. Everything stronger than that could imply: (1) flux emergence with kG horizontal fields (Cheung et al. 2008) or (2) strong network fields.

We note that the conclusions drawn here are based on a very rough and simple assumption. The increase in the field strength by a factor of 2 or 3 would result in a change of physical parameters as well as the dynamics of the plasma since the strong field is much less susceptible to the influence of the turbulent motions. This is, however, one of the steps towards revealing the role of the surface dynamo in the quiet Sun magnetism until more realistic simulations, as well as higher resolution observation of the solar photosphere are available which could reveal the field configuration on smaller scales.

5 Magnetic Field Intensification

5.1 Introduction

Magnetic field is ubiquitously present in the solar photosphere (de Wijn et al. 2009). On the granular scales, it undergos continuous deformation and displacement. It is swept by the horizontal flows and concentrated in the intergranular lanes. Flows are able to compress the field so that the magnetic energy density $B^2/8\pi$ approaches the kinetic energy density $\rho v^2/2$ of flow (Parker 1963, Weiss 1966). This results in a magnetic field strength of a few hundred Gauss at the solar surface. Further intensification to kG strength is driven by the mechanism referred to as: *superadiabatic effect* (Parker 1978), *convective collapse* (Webb & Roberts 1978, Spruit & Zweibel 1979) or *convective intensification* (Grossmann-Doerth et al. 1998).

The first two concepts are a theoretical idealization of the process. The superadiabatic effect contains the basic idea. Parker (1978) pointed out that a thermally isolated dowflowing gas within the flux tube in a superadiabatically stratified environment will be accelerated, which would lead to evacuation of the flux tube. Because of the resulting pressure deficit, the gas inside the flux tube will then be pressed together (together with the frozen-in magnetic field field) by the surrounding gas, causing the magnetic pressure to increase until a balance of total pressure (magnetic + gas) is reached.

The convective collapse extents the concept to the convective instability. It starts with a flux tube in thermal and mechanical equilibrium with the surrounding hydrostatically superadiabaticly stratified plasma. Since external stratification is convectively unstable, any vertical motion within the flux tube can be amplified. Downward flow will grow in amplitude and drain the material from the flux tube. The process continues until a new equilibrium with a strong field is reached. Different aspects of the concept have been the subject of extensive research (see Schüssler 1990, Steiner 1999, for reviews).

The term convective intensification is used for magnetic field intensification in realistic MHD simulations, where the process occurs in its full complexity. It is driven by the thermal effect in the surface layer of the magnetic concentration. There, due to presence of magnetic field, heat transport by convection is reduced. The material inside the concentration radiates more than it receives. This leads to cooling of material which thus starts to sink and partial evacuation of the concentration occurs. Contraction of the magnetic concentration by the surroundings (result of the pressure imbalance) leads to increase in magnetic field strength. Thus, the simulations (Nordlund 1983, Grossmann-Doerth et al. 1998, Vögler et al. 2005, Cheung et al. 2008) bear out the basic properties described by idealized concepts, such as: the downflow, the evacuation of the magnetic structure, the field increase and, in some cases, establishment of a new equilibrium. The 3D MHD sim-

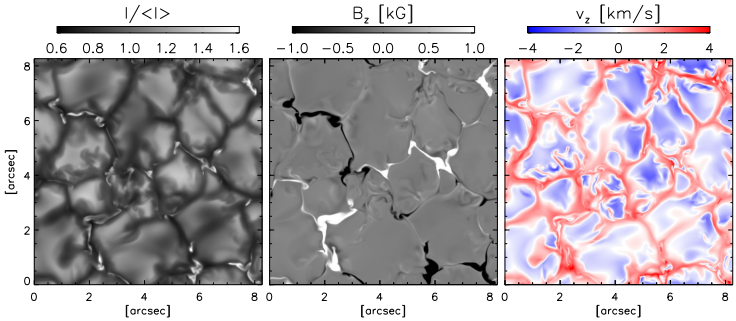

Figure 5.1: Maps of the whole simulation domain at $t = 140$ s. Normalized continuum intensity (left), vertical component of magnetic field (middle) and velocity (right) at a geometrical height roughly corresponding to the level of $\langle \tau_{500} \rangle = 1$.

ulation show that the strong magnetic concentrations form as the horizontal flows in the intergranular lanes advect the weak, nearly vertical field and concentrate it at the vertices of granular and mesogranular downflow lanes (Stein & Nordlund 1998, Stein &Nordlund 2006). Larger magnetic structures form at sites where a granule submerges and the surrounding field is pushed into the resulting dark region. Whether the formed concentration appears dark or bright in the continuum intensity depends on whether the vertical cooling is compensated or not by the lateral heating due to horizontal energy exchange (Bercik et al. 2003, Vögler et al. 2005). This formation scenario is consistent with the observations described by Muller (1983) and Muller & Roudier (1992). Their observations show that network bright points form in intergranular spaces, at the junction of converging granules as the magnetic field gets compressed by the converging granular flow.

The 2D simulations by Grossmann-Doerth et al. (1998) showed that magnetic flux concentration formed by the convective intensification can evolve in different ways. They present two possible outcomes. Depending on the initial magnetic flux, magnetic concentration can reach a stable state after the process, or can be dispersed due to an upflow that develops as high speed downflowing material rebounces from the dense bottom of the tube.

Observational evidence was found for both cases. Bello González et al. (2008) reported on the formation of a magnetic feature at the junction of intergranular lanes, without any significant upflow observed. Bellot Rubio et al. (2001), on the other hand, detected a strongly blueshifted Stokes V profile originating in an upward propagating shock, 13 minutes after the amplification of magnetic field. Socas-Navarro & Manso Sainz (2005) found that this type of Stokes V profiles is actually quite common.

Events that are interpreted as convective collapse were detected also with the spectropolarimeter (SP) (Lites et al. 2001) of the Solar Optical telescope (Tsuneta et al. 2008a) on board of Hinode (Kosugi et al. 2007). Both, Shimizu et al. (2008) and Nagata et al. (2008) show cases of high speed downflows followed by magnetic field intensification and bright point appearance. The event described by Nagata et al. (2008) shows stronger field strength and upflow in the final phase of evolution.

In this chapter we give three examples of magnetic field intensification from MURaM simulations and make detailed comparison with the results of Nagata et al. (2008) and Shimizu et al. (2008).

5.2 Simulation data and spectral synthesis

We use 3D radiative MHD simulations of a thin layer containing the solar surface carried out with the MURaM code (Vögler 2003, Vögler et al. 2005) in a $6 \times 6 \times 1.68$ Mm domain with non-grey radiative transfer included. Vertical and horizontal spatial resolution is 10 km and 14 km respectively. The bottom and top boundaries are open, permitting free in and outflow of matter. The initial magnetic field of $\langle |B| \rangle = 200$ G, is introduced in a checkerboard-like 2×2 pattern, with opposite polarity in adjacent parts. As the field is redistributed by convective motions, opposite polarities are pushed together and dissipated, so that the unsigned magnetic flux decreases with time. In this way, the run simulates the decay of the magnetic field in a mixed polarity region. Local dynamo action (Vögler & Schüssler 2007) does not occur since the magnetic Reynolds number is below the threshold for dynamo action. We examine a 30 min sequence of snapshots with an irregular cadence of approximately 90 s. The snapshots shown in this chapter have $\langle |B| \rangle \approx 150$ G at $\tau = 1$. The continuum image, magnetogram and vertical velocity map of a snapshot, to which the time instant $t = 140$ s is associated ($t = 0$ s is associated to the first snapshot considered in this chapter), is shown in Fig. 5.1.

In order to synthesize the Stokes profiles, the physical parameters from the simulation are used as an input for the 1D LTE radiative transfer code, SPINOR (Frutiger et al. 2000). A spectral range that contains Fe I lines 630.15 and 630.25 nm is sampled in steps of 7.5 mÅ. The Fe abundance used for the synthesis have been taken from Thevenin (1989) and the values of the oscillator strengths from the VALD database (Piskunov et al. 1995). Before comparing with Hinode/SP (Lites et al. 2001) observations, the synthetic line profiles have been treated to bring them to the same resolution as Hinode data. Firstly, a realistic point spread function PSF (Danilovic et al. 2008) has been applied to the synthesized Stokes profiles. The PSF takes into account the basic optical properties of the Hinode SOT/SP system and a slight defocus which brings the continuum contrast of the simulation to the observed value of 7.5%. Secondly, to take into account spectral resolution of the spectropolarimeter, profiles are convolved with a Gaussian function of 25 mÅ FWHM and resampled to a wavelength spacing of 21.5 mÅ. Thirdly, noise of $10^{-3} I_c$ is added. At the end, the convective blueshift is removed by fitting a mean Stokes I profile obtained by averaging over pixels with polarization signal amplitudes less then $10^{-3} I_c$. Finally, the procedure by Lites et al. (2008) is used to calculate the longitudinal apparent magnetic flux density (shown in Fig. 5.2).

5.3 Results

Fig. 5.2 shows a sequence of continuum maps and magnetograms of a 2.9×2.2 Mm subdomain of the simulation, over approximately 7 minutes. Shown are maps at the original resolution of the simulation (left-hand side) and at the spatial resolution of Hinode

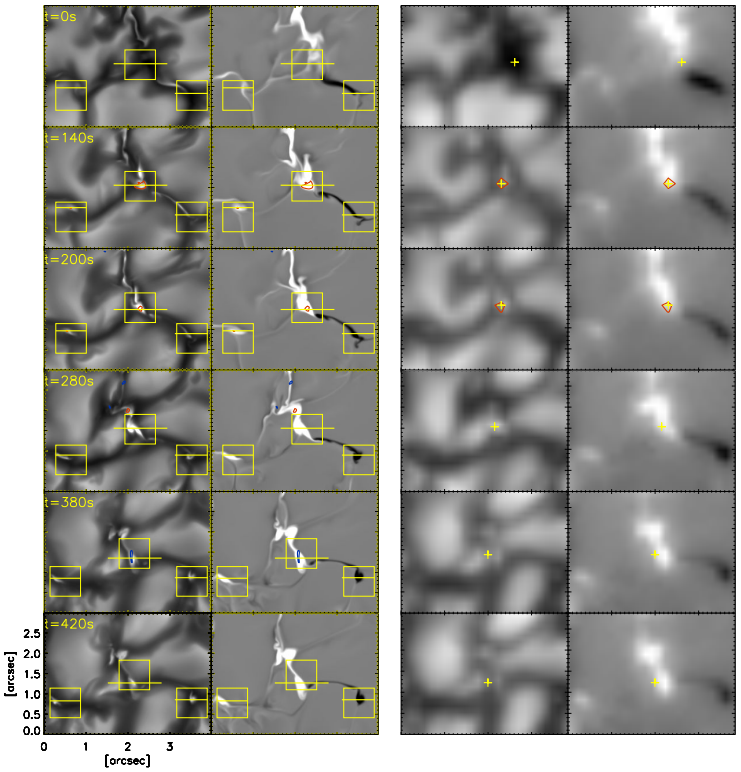

Figure 5.2: Sequence of synthetic continuum images and magnetograms of a $4'' \times 3''$ sized region. *Left-hand side*: original spatial resolution; red and blue contours delineate the downflow of 6 km/s at 80 km and upflow of 4 km/s at 400 km above $\tau = 1$, respectively; horizontal lines mark the positions of vertical cuts shown in Figs. 5.4 and 5.6; squares outline the regions enlarged in Fig. 5.3. Boxes corresponding to cases I, II and III at coordinates $[2'', 1.5'']$, $[0.5'', 1'']$ and $[3.5'', 1'']$, respectively. *Right-hand side*: Hinode spatial resolution; red contour marks the region with 0.01 pm of signal excess (see the text); yellow crosses mark the positions of pixels that are studied in detail in Fig. 5.9. Grey scales cover the range of 0.6-1.6 and 0.8-1.2 for normalized intensity at original and reduced resolution, respectively, ± 1000 G for the vertical component of magnetic field (original resolution) and ± 200 Mx/cm^2 for the apparent longitudinal magnetic flux density (Hinode resolution).

(right-hand side). During the period shown, three bright points appear near the coordinates [2″, 1.5″], [0.5″, 1″] and [3.5″, 1″], in the regions outlined by yellow squares. We refer to them here as cases I, II and III, respectively.

5.3.1 Horizontal flows

In all three cases, magnetic field is advected by the flow to the junction of multiple granules, where it is confined and concentrated. The evolution of magnetic concentrations is examined more closely in Fig. 5.3, where the regions outlined by yellow squares in Fig. 5.2, are enlarged. Horizontal velocities, at approximately 80 km above $\langle\tau\rangle = 1$, are represented by arrows in continuum maps and magnetograms. Regions with a strong vertical component of vorticity are also outlined.

Vortex flows around strong downflows are quite common for simulations (Nordlund 1986). They are formed at the vertices between multiple granules where flows converge and angular velocities with respect to the center of downflow increase due to angular momentum conservation. The lifetime of vortex flows depends on the behavior of the neighboring granules. In a 30 min run that we examined, they last from less then 90 s to approximately 10 min. The ones shown in Fig. 5.3 are short-lived. In case II, the swirling motion persists for at least 150 s, until the shape of neighboring granule is changed. The formed flux concentration is then squeezed between two granules and stretched into a flux-sheet-like feature. Later on, as the granules evolve, the magnetic feature is advected to the left and trapped again in the newly formed granular junction. In case III, a strong preexisting flux sheet is carried by the flow toward the junction of the granules. There, the field is caught in a vortex flow that lasts for at least 100 s. The flow becomes disturbed and then starts to swirl in the opposite direction. The vortex axes are inclined, in both cases II and III, with respect to the vertical direction. Also in both cases, there is a spatial and temporal coincidence between the existence of vortex flows and the formation of high speed downflows near the surface layer.

The vortices shown in Fig. 5.3 are less then 0.25″ in diameter, much smaller then the ones found in observations (Bonet et al. 2008). The size of the observed vortex flows is of order 1″ and the average lifetime is around 5 min. They seem to outline supergranulation and mesogranulation cells. As the authors of the observational study suggest, most vortices could have been missed because of the limited spatial resolution (Swedish Solar Telescope) and the method used (tracking the motion of bright points in G band). A short-lived vortex flow preceding formation of a network bright point has been observed by Roudier et al. (1997).

No vortex is detected during the formation of flux concentration in case I. In this case, a strong downflow, and later upflow develops inside the flux concentration. Its shape and contrast in the intensity map is greatly affected by the convective motions. Spatial and temporal fluctuations across the magnetic feature make it difficult to define its center. The bright points, visible in continuum maps, form in the regions with higher field strength and where fragments of flux concentration become narrow so that lateral heating becomes important.

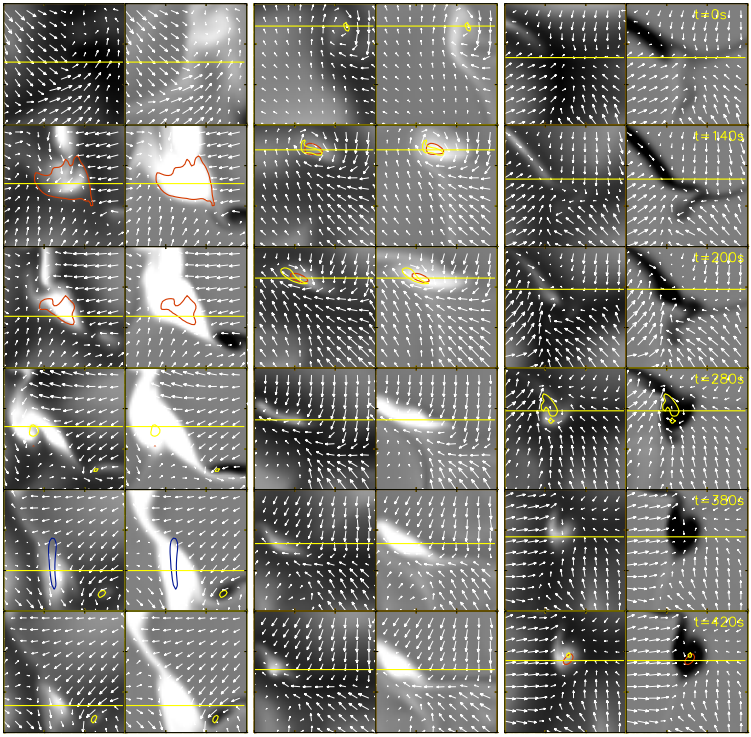

Figure 5.3: Enlargement of the regions outlined by yellow squares in Fig. 5.2. From left to right: cases I, II and III. Continuum images (left) and magnetograms (right) of $0.75'' \times 0.75''$ regions, with overplotted horizontal velocities at approximately 80 km above $\tau = 1$ (white arrows). Red contours outline locations of downflows of 5 km/s or larger and yellow contours the vertical component of vorticity exceeding $\pm 0.2 s^{-1}$ (cases I and II) or $\pm 0.1 s^{-1}$ (case III).

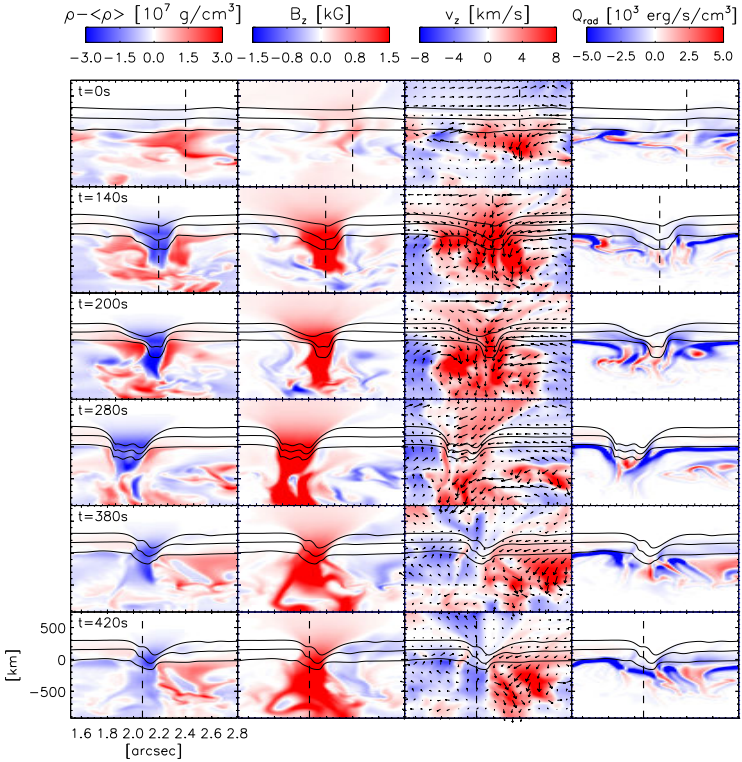

Figure 5.4: Time sequence of vertical cuts through the magnetic concentration corresponding to case I (positions of the cuts are marked by yellow horizontal lines (upper ones) in left-hand images in Fig. 5.2). The plotted cuts correspond to the same instants as sampled in Fig. 5.2. From left to right: density excess with respect to the mean density at every height, vertical component of magnetic field, vertical component of velocity (overplotted arrows show the components of the velocity field in the x-z plane), and radiative heating rate. Horizontal solid lines show levels of log $\tau = 0, -1$ and -2. Vertical dashed lines mark the position of the height profiles given in Fig. 5.5.

5.3.2 Field intensification

The evolution of the magnetic structures formed during the studied time interval can be followed in more detail by taking vertical slices through the regions marked by horizontal lines in Fig. 5.3. We will examine three cases.

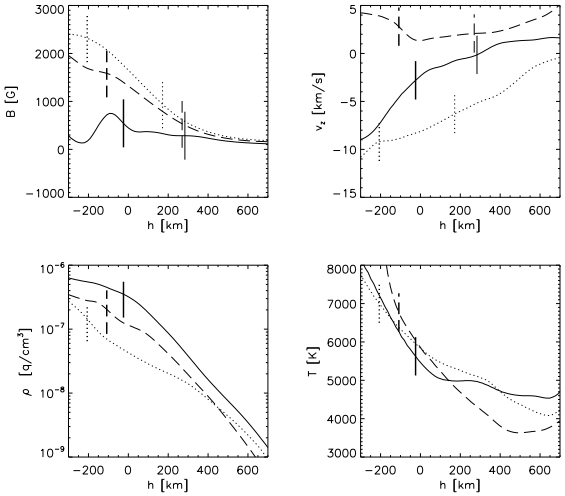

Figure 5.5: Height profiles of: magnetic field, vertical component of velocity, density and temperature in the flux concentration corresponding to the case I at the positions marked by dashed lines in Fig. 5.4. Different line styles correspond to different times: solid - $t = 0$ *s*, dotted - $t = 140$ *s*, dashed - $t = 420$ *s*. Thick vertical lines mark the positions of the optical depth $\tau_{500} = 1$ for each atmosphere. Thin vertical lines in the top two panels mark the positions of the height of formation of Fe I 630.25 nm line (see the text).

5.3.2.1 Case I

Vertical cuts through the regions corresponding to this case are given in Fig. 5.4. Shown are the density excess (relative to the mean density at each geometrical height), the vertical components of magnetic field and velocity, and the radiative heating rate. Cuts at the instant $t = 0$ show the fluctuation in density outlining the granulation structure, with less dense, hotter granule and cooler inergranular lane where magnetic field of few hundred G is accumulated and a downflow of a few km/s is present. The fluctuation in radiative heating rate is highest in the thin layer near optical depth unity, where upflowing granular material cools most strongly. The regions along the intergranular lane seems to undergo cooling in the layers above $\tau_{500} = 1$. In the next instant, 140 s later, a strong magnetic concentration has already formed. Variations in magnetic field strength, at a given geometrical height, are accompanied by variations in the gas pressure. Regions with increased field strength have lower density, which, in turn, shifts the level of optical depth unity downwards relative to neighboring regions with weaker field. The depression of the visible surface inside the magnetic structure gives rise to radiative heating through the sidewalls from the hot neighboring material. The downflow velocity is significantly increased from $t = 0$ to $t = 140$ and then, by $t = 280$ s, it is greatly diminished again inside the flux concentration. The diameter and the shape of the flux concentration continuously

evolves and does not reach a stationary state. At $t = 280$ s strong radiative heating is present inside the concentration. This is also the moment when continuum intensity is the highest as shown later (Fig. 5.9).

In the last two sets of snapshots, shown in Fig. 5.4, an upflow is visible inside the flux concentration, extending almost from the bottom of simulation domain. The upflowing material inside the concentration exhibits strong cooling at the surface. As the material refills the region inside the flux concentration, the level of optical depth unity shifts upwards and magnetic field strength decreases. However, the upflow does not lead to a complete dispersal of the field, as the further snapshots (not shown here) indicate.

The evolution of this flux concentration is further illustrated by the vertical profiles given in Fig. 5.5. Three phases before and after the field intensification are shown. The horizontal positions of the profiles are marked by vertical dashed lines in Fig. 5.4. The profiles of magnetic field strength, vertical component of velocity (downflows have negative values), density and temperature for each phase are shown together with the corresponding level of optical depth unity, marked by thick vertical lines. The level $h = 0$ corresponds to the level of the mean optical depth unity $\langle\tau_{500}\rangle = 1$ for the whole snapshot. Thin vertical lines in upper plots mark the position of the average height of formation of Fe I 630.25 nm line, which is defined by calculating the centroid of the contribution function (CF) for line intensity depression (Solanki & Bruls 1994), at the wavelength of the line minimum. The definition gives only a rough estimate of the heights sampled, since the lines are formed over a large portion of the photosphere and the CF are asymmetric in wavelength due to the presence of high velocity gradients.

The figure shows that, in the interval from $t = 0$ s to $t = 140$ s, the downflow extends to deeper layers and increases in amplitude, reaching 10 km/s at 200 km below the surface. The magnetic field strength increases from a few hundred to more than 2000 G at the level of $\tau_{500} = 1$. The significant reduction in density results in a shift of 200 km in the optical depth unity level. As a result of radiative heating the temperature gradient is flatter and the temperature is around 400 K higher at the layer of $\langle\tau_{500}\rangle = 1$, i.e. at equal geometrical height. The temperature difference at equal optical depth is even larger, exceeding 1000 K at $\tau_{500} = 1$. The estimated height of formation of Fe I 630.25 nm line shifts from roughly 300 km to 150 km above the surface when magnetic field concentration forms, which is in agreement with Khomenko & Collados (2007). This effect contributes to the increase of observed magnetic field strengths in the first two phases.

In the third phase, the upflow leads to density enhancement and a weakening of the magnetic field by a few hundred Gauss in the lower photosphere. The level of $\tau_{500} = 1$ shifts upward by 100 km. No discontinuity is visible in the vertical component of velocity, in contrast to the event studied by Grossmann-Doerth et al. (1998).

5.3.2.2 Cases II and III

Vertical cuts through the regions corresponding to these cases are shown in Fig. 5.6. The positions of the cuts are marked by horizontal lines in Fig. 5.3. The parameters shown are the same as in Fig. 5.4.

At $t = 0$, weak magnetic structures in the intergranular lanes are already present in both cases. Strong downflows along the magnetic field lines persist over the entire time interval shown. In case II, it is strongest at $t = 140$ s, just before the vortex flow becomes

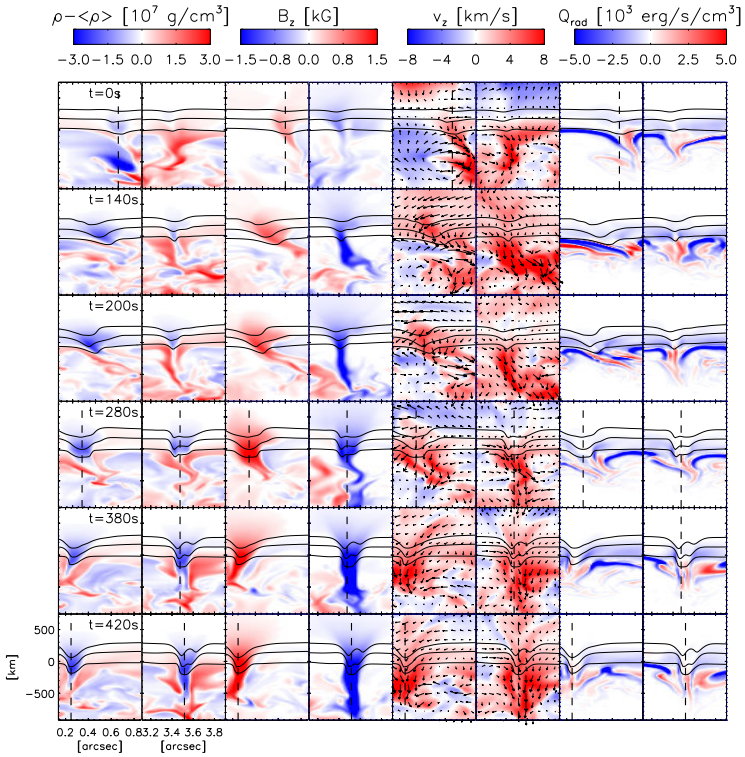

Figure 5.6: The same as Fig. 5.4 but for cases II and III. Each frame is subdivided into a left part displaying case II and a right part showing case III. Vertical lines mark the position of the height profiles given in Fig. 5.7 and Fig. 5.8.

deformed owing to evolution of the neighboring granule. Then it gets somewhat reduced at t=280s, as the structure is squeezed between the granules. Later, at $t = 380$ s, a strong downflow is present again in the newly formed granular junction, to which the flux concentration is carried to and where it is confined again. The rightmost columns show strong cooling of the layers above the level of $\tau_{500} = 1$ in both cases. At $t = 420$ s, the interior of the flux concentrations reaches radiative equilibrium. At that moment, the flux concentrations in both cases are almost vertical, with diameters of approximately 0.1″ at $\tau_{500} = 1$.

Figures 5.7 and 5.8 show height profiles along the positions marked by the dashed lines in Fig. 5.6. Since the flux concentrations are inclined, the choice of curved lines, along the axes of magnetic structures, would be more logical here. However, we are interested in what would be observed at the disc center and the observables (i.e. the Stokes profiles) depend on the vertical profiles of the physical parameters which are shown here.

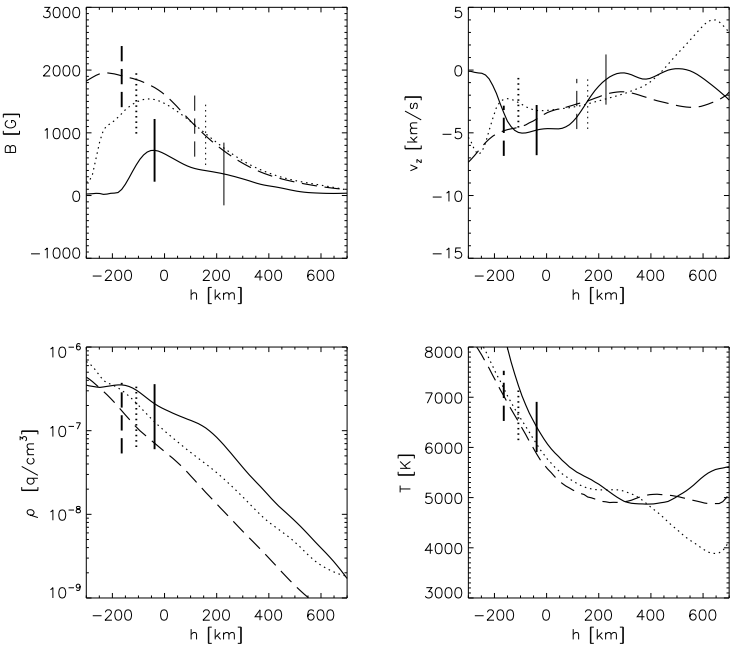

Figure 5.7: The same as Fig. 5.5 but for case II. Atmospheres marked by vertical lines in Fig. 5.6 are represented by: solid, dotted and dashed curves for $t = 0, 280, 420$ s, respectively.

In the case II, we choose to show profiles at instants t = 0, 280 and 420 s (solid, dotted, dashed respectively). For the case III, profiles at the last three instants from Fig. 5.6 are shown. Both cases exhibit a similar behavior: there is a significant evacuation of the magnetic concentration due to the strong downflow and an increase of the magnetic field strength from a few hundred G to kG values in the process. There is a persistent downflow that reaches 5 km/s (in the vertical direction) at $\tau_{500} = 1$ and a decrease in density with a corresponding shift in the height of $\tau_{500} = 1$. In both cases, the shift in $\tau_{500} = 1$ reaches 150 km and the magnetic field strength increases to 2000 G at that depth. The height of formation of the Fe I 630.25 nm line shifts to deeper layers as the magnetic field strength increases. In the last instant, the Fe I 630.25 nm line probes layers with kG fields and vertical velocity of 5 km/s, in both cases.

5.3.3 Comparison with synthetic Hinode observations

The intensity contrast is considerably reduced at Hinode spatial resolution as can be seen in Fig. 5.2 (note that the color scales are adjusted). The maps of longitudinal apparent

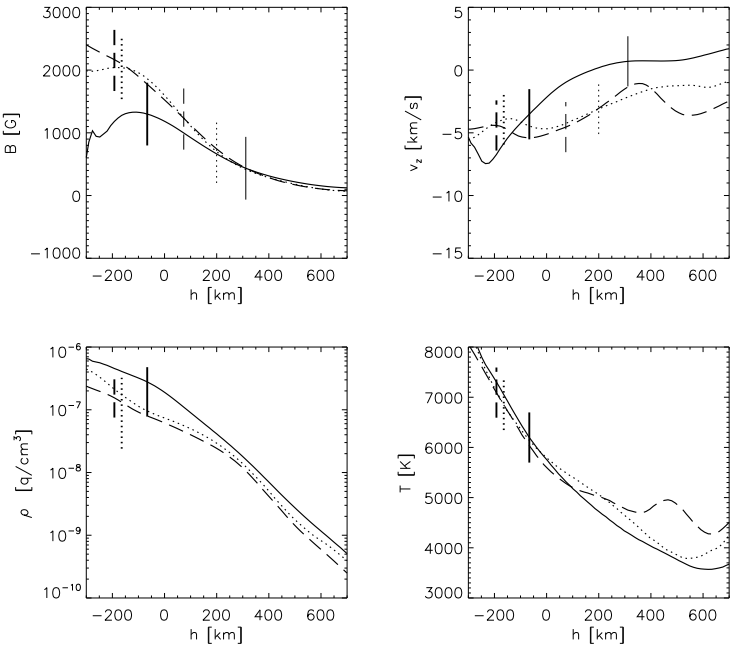

Figure 5.8: The same as Fig. 5.5 but for case III. Atmospheres marked by vertical lines in Fig. 5.6 are represented by solid, dotted and dashed curves for $t = 280, 380, 420$ *s*, respectively.

magnetic flux density are shown for the comparison with the magnetograms at the original resolution. Fine structures in both maps, continuum and magnetograms, are lost due to smearing. The bright points that correspond to cases II and III are barely discernable.

5.3.3.1 Cases I

In order to compare case I with the results of Shimizu et al. (2008), we calculate the parameter they refer to as *signal excess* (SE). It is defined as the Stokes *V* profile integrated over the spectral range of 250 – 400 mÅ redward from the nominal line center. This wavelength range corresponds to downflows of 7 – 14 km/s, so that high values of SE indicate the presence of hight-speed downflows. The red contour at the right-hand side of Fig. 5.2 outlines a region with SE of 0.01 pm, which is a factor of 10 higher than in the surroundings. It fits the location and time of the strong downflows visible at the original resolution (left hand-side of Fig. 5.2). Both, synthesized (here) and observed (Shimizu et al. 2008) SE occur simultaneously with the appearance of the bright point and the intensification of the magnetic field. There is, however, a difference in the duration of

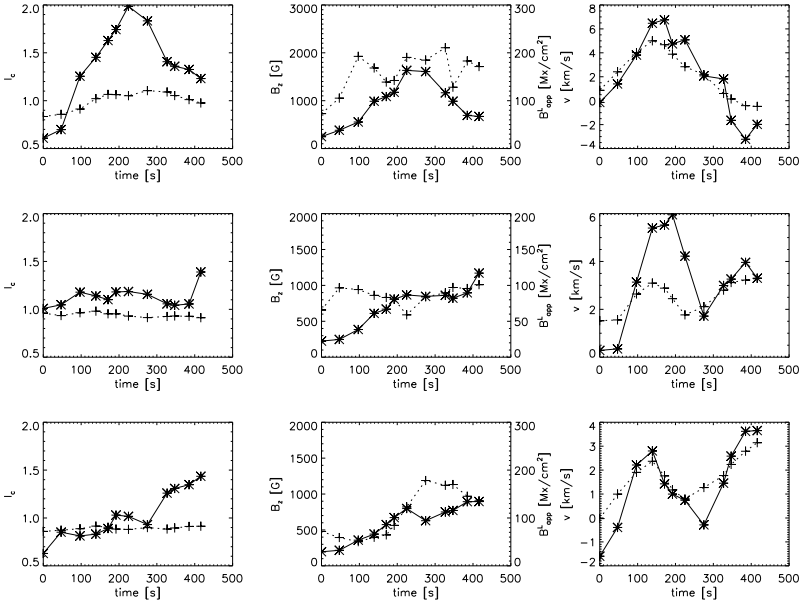

Figure 5.9: Temporal change of normalized intensity (left), magnetic field strength (middle) and vertical velocity (right) for cases I (top row), II (middle row) and III (bottom row) at original (stars/solid line) and Hinode resolution (crosses/dashed line). Vertical component of magnetic field and velocity at $\log \tau_{500} = -2$ (for original resolution) are each plotted together with the longitudinal apparent magnetic flux density and velocity retrieved from Stokes V profiles (Hinode resolution), respectively.

the events. While the event described by Shimizu et al. (2008) (Fig. 8) lasts at least 6 minutes, the event seen in simulations endures for less than 4 minutes.

Figure 5.9 compares the observable parameters with the corresponding values at original resolution. The locations taken for the plots are marked by yellow crosses in Fig. 5.2. The pixels are selected such that regions of downflow and upflow are covered, as well as the evolution of the bright point. The plots show the temporal change of normalized intensity, longitudinal apparent flux density (Lites et al. 2008), and velocity. The velocities are zero-crossing velocity retrieved from Stokes V profiles of the Fe I 630.25 nm line, so that a direct comparison with the results of Nagata et al. (2008) can be made. Overplotted (stars/solid lines) are the normalized intensity at the original resolution, the vertical component of magnetic field and velocity at $\log \tau_{500} = -2$.

The comparison shows that the correlation between the parameters at original and reduced resolution is not so good. This is a consequence of different effects. Firstly, since the formation region of the Fe I 630 nm lines extends over a large part of the atmosphere, there is smearing along the line of sight and the resulting profiles carry information from different layers with different values of the physical parameters. Secondly, the smearing due to spatial resolution affects every pixel differently depending on its neighboring pixels. The profiles could be more asymmetric and broader due to averaging over inhomogeneous regions and the amplitude of Stokes V can be affected. Figure 5.10 shows examples of Stokes I and V profile at original and reduced resolution at $t = 0$, 140 and 420 s. The profiles show stronger asymmetries and higher Doppler shifts at original resolution. The amplitudes of Stokes V profiles at Hinode resolution are reduced by a factor of 10. They are of the same order of magnitude as the observed ones (Nagata et al. (2008), Fig. 2). Both, synthesized and observed Stokes I profiles show an extended red wing at the phase with strong downflow.

Figure 5.9 shows that intensity contrast is significantly reduced by spatial smearing. At $t = 230$ s, the contrast drops from 100% at original resolution to below 30% at the reduced resolution. The velocity determined from Stokes V profiles is at most times somewhat lower then the velocities at $\log \tau_{500} = -2$. However, the general trends of the parameters are preserved. For both, simulation and observation (Nagata et al. 2008), the intensity reaches its maximum approximately 100 s later than velocity. This is consistent with the idea that the enhanced brightness results from the evacuation due to the downflow. When the velocity changes sign, the brightness starts to fade in both cases. The maximum brightness of the simulated and observed bright points are similar, while simulated velocities are somewhat smaller. They reach approximately 5 km/s (downflow) and 0.5 km/s (upflow), while values up to 6 km/s and 2 km/s, respectively, are observed. The magnetic field strength obtained by Nagata et al. (2008), by inversions, increases from a few hundred to 2000 G in approximately 200 s, which is in agreement with simulations.

5.3.3.2 Cases II and III

The middle and bottom rows in Figure 5.9 show the temporal evolution for cases II and III, respectively. We find a simultaneous increase in all parameters (continuum intensity, apparent flux density and zero-crossing velocity). In both cases, the downflow is suppressed at $t = 280$ s possibly because of the evolution of the surrounding granules. The velocity at $\log \tau_{500} = -2$ reaches 6 and 4 km/s for case II and III, respectively. As the

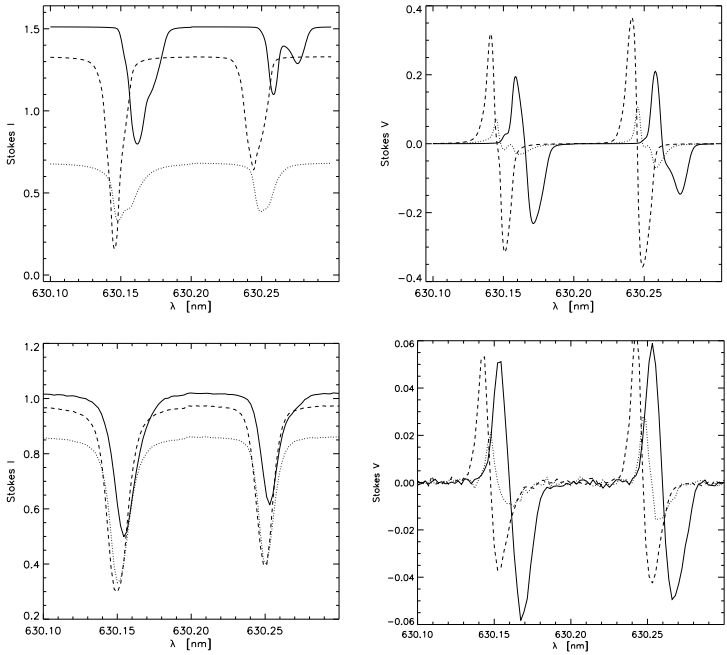

Figure 5.10: Synthetic Stokes I (left) and V (right) profiles at original (upper row) and Hinode resolution (lower row) for the times $t = 0, 140$ and 420 s marked by dotted, solid and dashed, respectively. The intensity is normalized to the mean of the full snapshot domain.

magnetic field strength increases, the intensity follows and the intensity contrast reaches 50% with respect to the mean at original resolution, in both cases.

The influence of spatial smearing is on the whole similar, although a few differences relative to case I are noteworthy. Firstly, due to the small size of the features, the correlation of the magnetic and brightness signals is largely destroyed. Although the magnetic signals are comparable to the values in case I, the brightness is lower so that the features are inconspicuous in continuum images. The increase in magnetic flux density is followed by just a small fluctuation in intensity. Secondly, although the magnetic field strengths and diameters of the features are comparable for cases II and III at original resolution, the structure of case II shows lower magnetic flux density. Thirdly, the signature of the strong downflow in case II is lost due to spatial smearing.

5.4 Summary

Our case study of three examples of magnetic field intensification has shown that in all three cases, the field is advected to the junction of several granules. There, it is confined by converging granular flows, which, in some cases, form a vortex. Owing to the presence of the magnetic field, the thermal effect induces evacuation of flux concentration. The downflow velocities reach maximum values of 5-10 km at $\tau_{500} = 1$. The magnetic features formed have diameters of $0.1'' - 0.2''$. In the case of the biggest feature, an upflow develops approximately 200 s after the formation of the flux concentration.

We show the evolution of flux concentrations at original resolution as well as the effects of smearing to reduced spatial resolution. In the case of small features, Hinode/SP would miss the bright point formation and, in some cases, also the high velocity downflows that develop in the process. On the other hand, the signatures of the evolution of large features are detectable even after the spatial smearing. We show that this case can be quantitatively compared with Hinode/SP observation (Nagata et al. 2008, Shimizu et al. 2008) and shows a very similar evolution.

6 Signatures of Magnetic Reconnection in the Photosphere

6.1 Introduction

Magnetic reconnection is a process by which the magnetic field topology is changed and the released magnetic energy is converted into thermal (Joule heating) and kinetic (oppositely directed jets) energy. It produces diverse signatures which depend on the location where the reconnection occurs. Tsuneta (1996) reports an event, observed in soft X ray images, during which antiparallel coronal magnetic fields from two separate active regions, located in opposite hemispheres, reconnect and form new transequatorial coronal loops. When reconnection happens in the transition region, small flare-like brightening are visible in EUV (Innes et al. 2009, Madjarska et al. 2004). The presence of bi-directional plasma jets is observed in FUV lines (Innes et al. 1997), revealing explosive events in the solar transition region. High-resolution movies of jet-like features were recorded in different spectral ranges (Cirtain et al. 2007, Shibata et al. 2007) with Hinode showing an enhanced emission in regions with an inverse Y shape. This seems to be a result of the emergence of magnetic flux from below the surface and its interaction with the preexisting field (Moreno-Insertis et al. 2008). Rezaei et al. (2009) show two examples of events with different levels of enhanced chromospheric emission, which they attribute to different geometrical heights in the photosphere at which the reconnection happens.

Theoretical studies of magnetic reconnection have been carried out by 2D or 3D numerical models with simple arbitrary initial configuration of the field that makes identification of the phases and changes in topology easier to follow (for example, Archontis et al. (2005), Aulanier et al. (2006), Wilmot-Smith & de Moortel (2007), Parnell et al. (2008)). The situation is far more complicated in realistic 3D MHD simulations.

Magnetic reconnection is an inseparable part of the flux cancellation process (Zwaan 1987) in the solar photosphere. When two magnetic patches of opposite polarity are pushed toward each another by the convective motions, the field reconnects, either below or above the surface. In the case of flux reconnection above the surface, flux removal from the surface is completed by the retraction of the formed inverse U-loop. The MURaM simulations, with an initial checker-board pattern of positive and negative vertical magnetic field, show that opposite polarity patches reconnect and the flux is removed from the observable layers of the Sun (Cameron et al. 2007). Regions where the flux cancels show a transformation of the initial upward and downward directed field into U-loop and inverse U-loop topology due to reconnection. It has been found that most of the reconnection occurs in the upper photosphere, where strong flux concentrations of oppo-

site polarity get into contact as they expand with height and move along the intergranular lanes. Most of the reconnected field around and below $\langle\tau_{500}\rangle = 1$ takes the form of the inverse U-loops. Less frequently, U-loop topology is found in the upper photosphere[1] since the rising U-loops leave the computational domain.

In this chapter we study an example of the flux cancellation from the MURaM mixed polarity run and examine whether some of the features of the process can be detected in spectropolarimetric observations.

6.2 An example from simulations

Figure 6.1 shows the evolution of the vertical magnetic field at the solar surface on a region of $3'' \times 4''$. The region contains mixed polarities, with reconnection occurring at several locations: (1) at $[1.5'', 2.5'']$ where positive polarity field is advected along two intergranular lanes towards the negative polarity and where a persistent strong downflow coincides with the polarity inversion; (2) at $[1'', 1.7'']$ where weak negative polarity cancels at the edge of the positive polarity patch and a strong upflow appears; (3) at $[1.7'', 1.2'']$ where negative polarity approaches and interacts with positive polarity. Figures 6.2 and 6.3 show the vertical magnetic field and temperature, respectively, at approximately 600 km above the solar surface in the same region. These figures show that owing to the expansion with height, strong field concentrations of opposite polarity are in contact with each other over large stretches in the upper photosphere. As they are transported towards each other by convective flows, the gradient of the magnetic field at the contact surface increases and the Joule heating becomes significant so that the temperature increases. Thus, thin regions with temperatures higher than 8000 K outline the sharp polarity inversion locations. These structures look like a 'textbook' current sheet with reconnection (e.g. Choudhuri (1998)): opposite polarities are pushed towards each other from the sides, a current sheet forms between them where the field is being dissipated, with vertical outflows present below and above the current sheet. In the MURaM simulations, the upflow is less frequently observed since the reconnection usually happens in the upper photosphere, near the upper boundary of the simulation domain. Figure 6.3 shows two examples of such upflows. At $t = 207$ s and $t = 225$ s, upflows of 4 and 9 km/s are visible at approximately 400 and 600 km above the solar surface, respectively. At this location, the lower layers show mixed polarity and a temperature increase. Thus, the reconnection in this case might be happening near or below the surface. A similar event is visible at $t = 386 - 431$ s.

Figure 6.4 shows the evolution of magnetic field lines in the reconnection event at $[1.7'', 1.2'']$. Note that the line of sight is directed roughly in the negative direction along the y axes in Figure 6.1. The opposite polarities are already connected at $t = 0$ s by an inverse U-loop whose apex is near the top boundary of the simulation domain. As the loop retracts, the antiparallel fields are pressed against each other to form a thin sheet of electrical current at the interface. Joule heating sets in and the local temperature of the plasma increases. The current sheet that initially appeared at the top of the simulation domain, expands downwards and at $t = 416$ s its endpoints bifurcate to form an inverted Y shape, commonly observed in numerical models of reconnection. At $t = 538$ s the loops have retracted almost completely.

[1] *http://www.mps.mpg.de/projects/solar-mhd/muram_site/results.html*

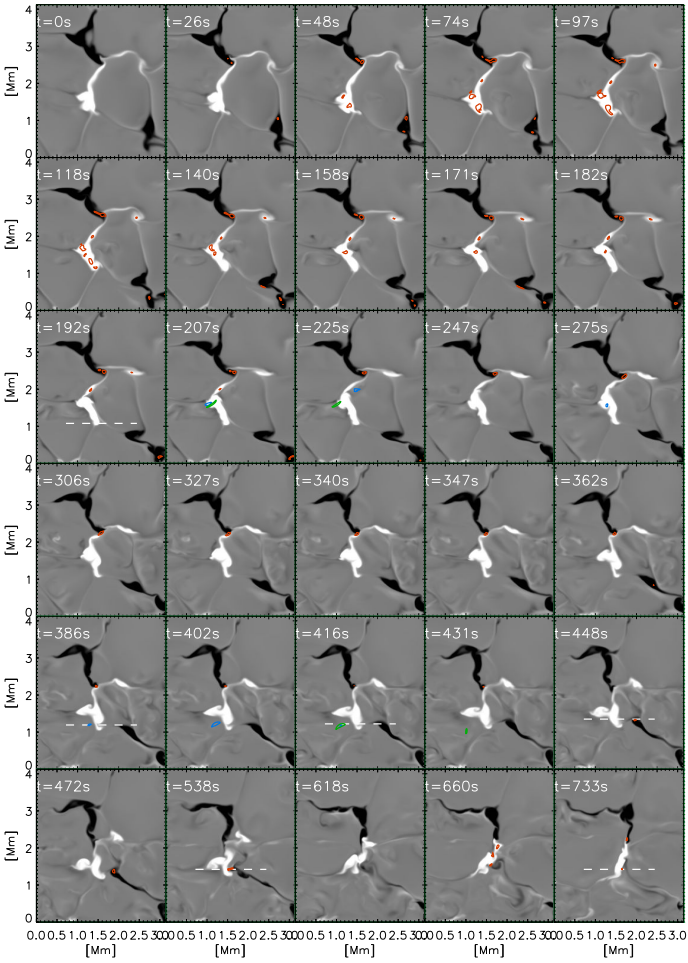

Figure 6.1: Time series of flux-cancellation events. The vertical magnetic field at ~ 80 km above $\langle\tau_{500}\rangle$=1 is plotted. Red and blue contours mark dowflow of 5 km/s at ~ 80 km and upflow of 4 km/s at ~ 400 km above solar surface ($\langle\tau_{500}\rangle$=1), respectively. Green contours outline regions where upflow exceeds 9 km/s at ~ 600 km above the solar surface. White dashed lines show the position of the cuts plotted in Fig. 6.5. The grey scale is saturated at ±1000 G.

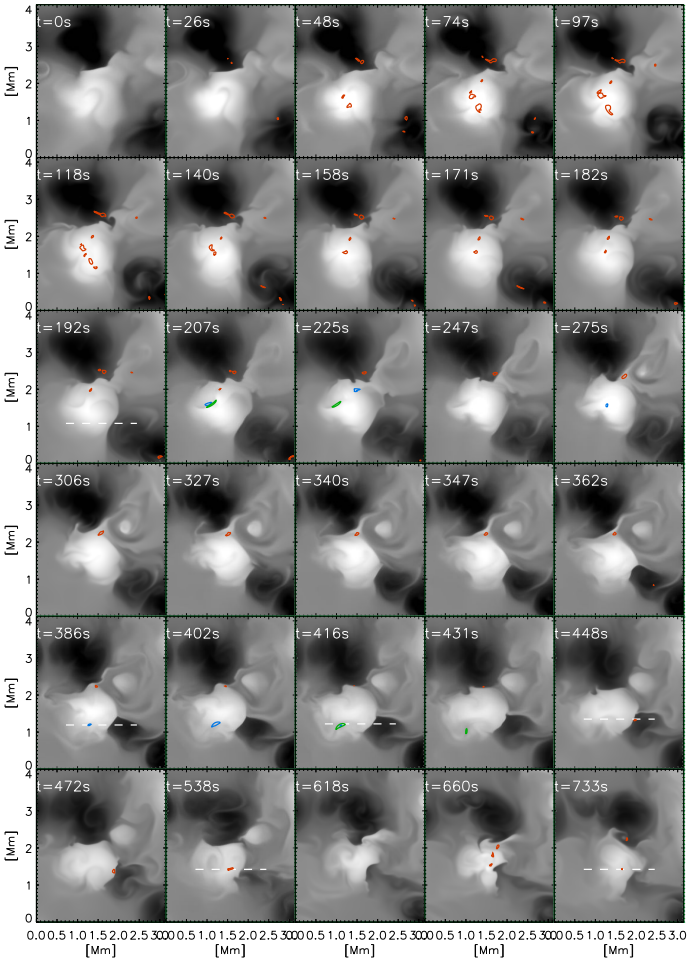

Figure 6.2: Time series of flux-cancellation events. The vertical magnetic field at ~ 600 km above $\langle\tau_{500}\rangle$=1 is plotted. Red and blue contours mark dowflow of 5 km/s at ~ 80 km and upflow of 4 km/s at ~ 400 km above solar surface ($\langle\tau_{500}\rangle$=1), respectively. Green contours outline regions where upflow exceeds 9 km/s at ~ 600 km above the solar surface. White dashed lines show the position of the cuts plotted in Fig. 6.5. The grey scale is saturated at ±200 G.

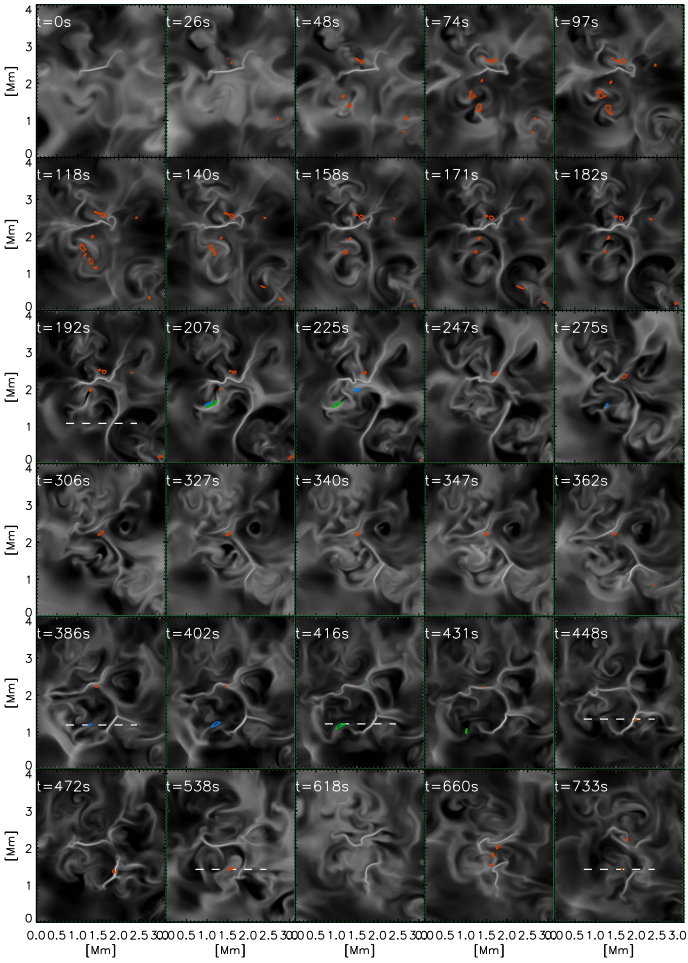

Figure 6.3: Time series of flux-cancellation events. Temperature at ∼ 600 km above $\langle\tau_{500}\rangle$=1 is plotted. Red and blue contours mark dowflow of 5 km/s at ∼ 80 km and upflow of 4 km/s at ∼ 400 km above solar surface ($\langle\tau_{500}\rangle$=1), respectively. Green contours outline regions where upflow exceeds 9 km/s at ∼ 600 km above the solar surface. White dashed lines show the position of the cuts plotted in Fig. 6.5. The grey scale goes from 3500 K to 8000 K.

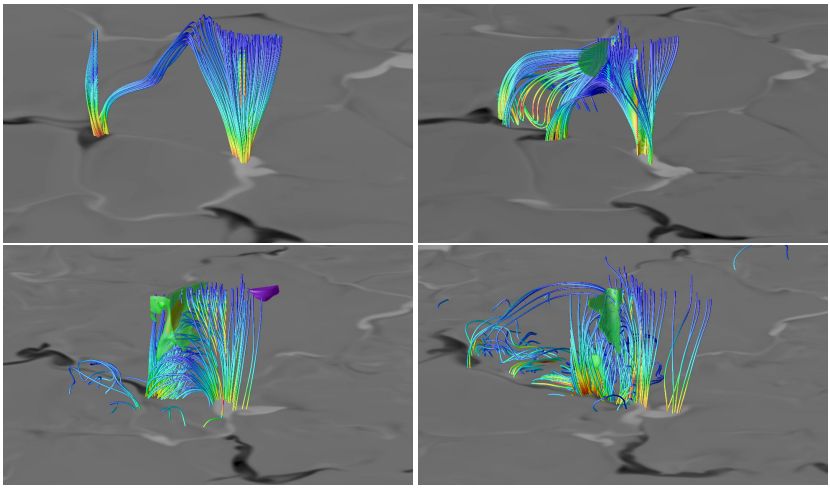

Figure 6.4: Evolution of magnetic field lines for a reconnection event in the upper photosphere at $[1.7'', 1.2'']$. The panels show a loop that is being retracted with time ($t = 0, 192, 416, 538$ s). Color coding along the field lines show the field strength change. The horizontal plane shows the vertical field at $\sim \langle \tau_{500} \rangle = 1$. The green translucent surface indicates the temperature isosurface at T= 5777 K. The red surface ($t = 416$ s) inside the green translucent surface marks the vertical component of velocity of 10 km/s directed downwards. The purple surface ($t = 416$ s) shows the position of the upflow of 9 km/s.

Vertical cuts, approximately along the loop, are shown in Fig. 6.5. The plots show two flux concentrations fanning out with height, moving closer to each other with time. The temperature increase coincides with the minima of the magnetic field strength (|B|). Owing to the sharply bent magnetic field lines, a downflow of $\sim$ 10 km/s is triggered by the magnetic tension force. It is located at the top of the simulation domain at $t = 192$ s. At a later time ($t = 386$ s), a weaker downflow reaches down to $\log \tau_{500} = 0$ inside the negative concentration and accelerates with time. A strong upflow appears on the other side of the positive flux concentration, following the increase of temperature in the same region. The upflow appearance is possibly connected with the presence of negative polarity field below the 'canopy' of the positive flux concentration.

6.3 Signature in the Stokes profiles of Fe I 630 nm lines

In this section we examine Stokes profiles of Fe I 630 nm lines in order to identify observable signatures of the reconnection process. As an example, we show the flip of the polarity seen in Stokes V profiles along the cuts shown in Fig. 6.5 at $t = 448$ s and $t = 538$ s. Figures 6.6 and 6.7 show the height profiles of temperature, vertical component of magnetic field and velocity, together with the emergent Stokes I and V profiles and contribution functions (CF) to the line depressions. The positions of the chosen lines

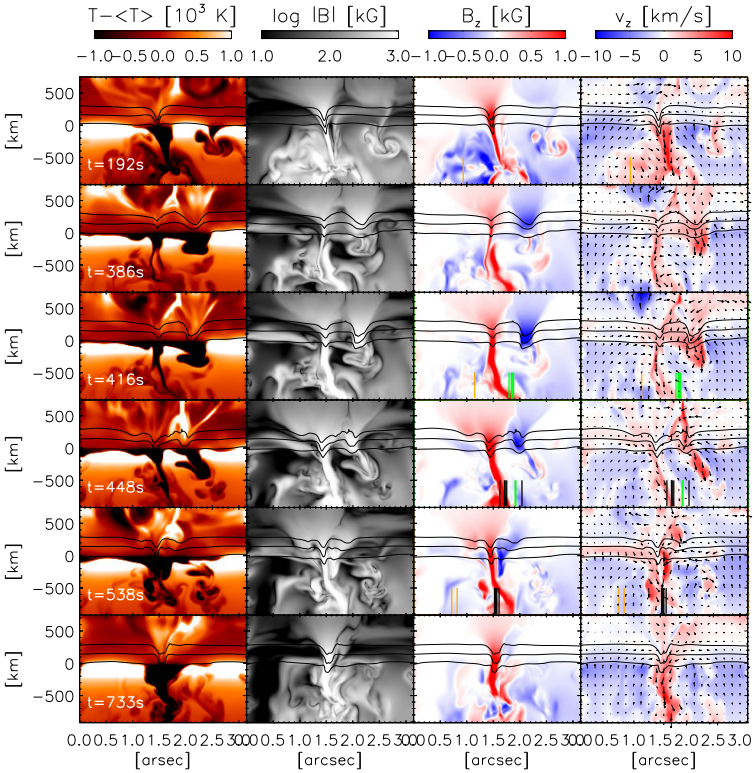

Figure 6.5: Vertical cuts through the regions marked by dashed lines in Figures 6.1, 6.2 and 6.3. *From left to right*: Temperature, magnetic field strength, vertical component of magnetic field and vertical component of velocity with overplotted velocity field in the $x-z$ plane. The black horizontal lines mark the position of the $\log \tau_{500} = 0, -1, -2$ levels. The vertical lines mark the position of the pixels chosen to be studied in detail in Figures: 6.8 (orange), 6.9 (green), 6.6 and 6.7 (black).

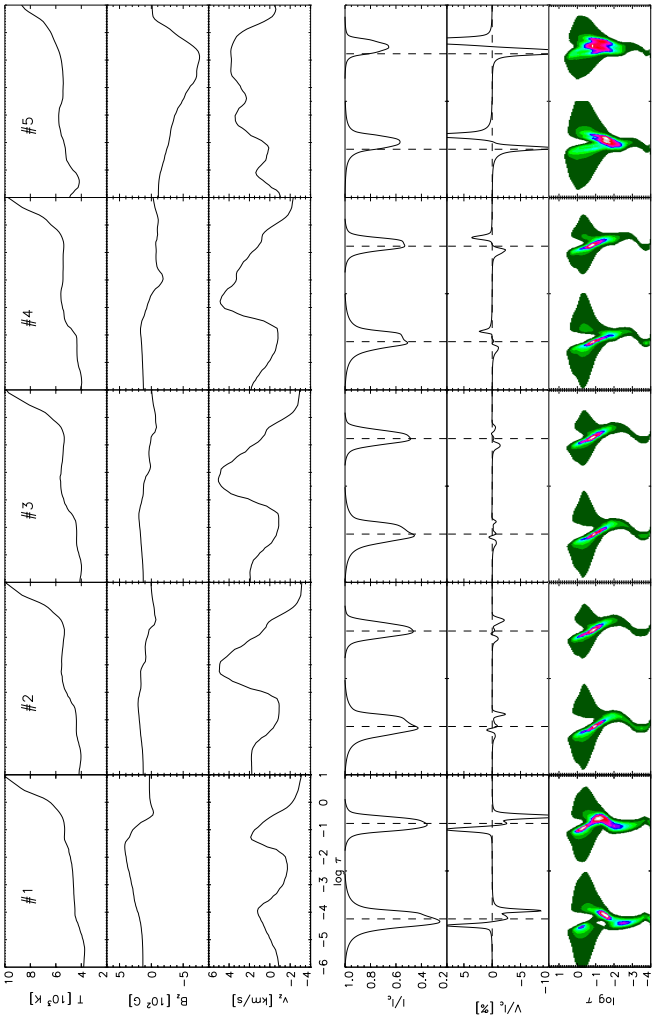

Figure 6.6: *From top to bottom:* Temperature, vertical component of magnetic field, vertical component of velocity, synthesized Stokes I and V profiles along the cut at $t = 448$ s shown in Fig. 6.5. Their position is marked by black vertical lines (from left to right).

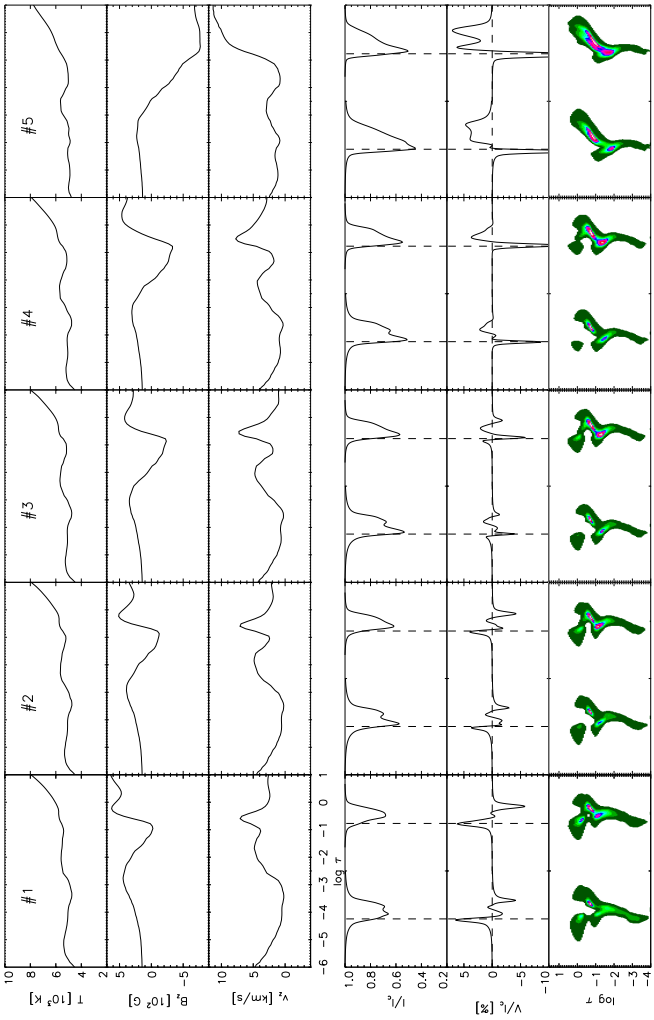

Figure 6.7: *From top to bottom*: Temperature, vertical component of magnetic field, vertical component of velocity, synthesized Stokes I and V profiles along the cut at $t = 538$ s shown in Fig. 6.5. Their position is marked by black vertical lines (from left to right).

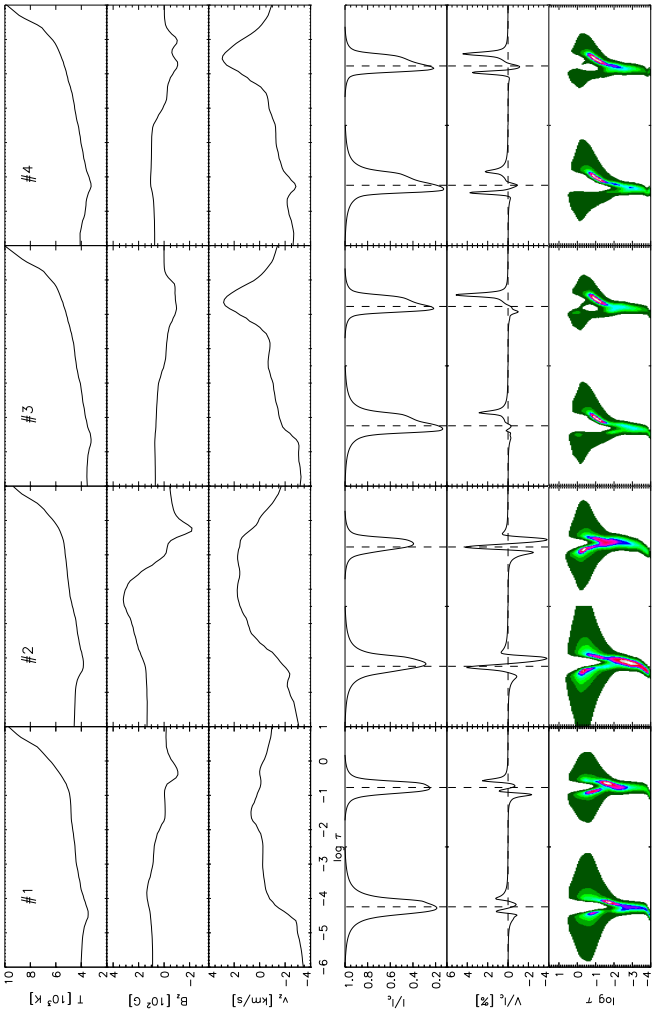

Figure 6.8: *From top to bottom:* Temperature, vertical component of magnetic field, vertical component of velocity, synthesized Stokes I and V profiles along the cuts at $t = 192,416,538$ s shown in Fig. 6.5. Their position is marked by orange vertical lines (from top to bottom).

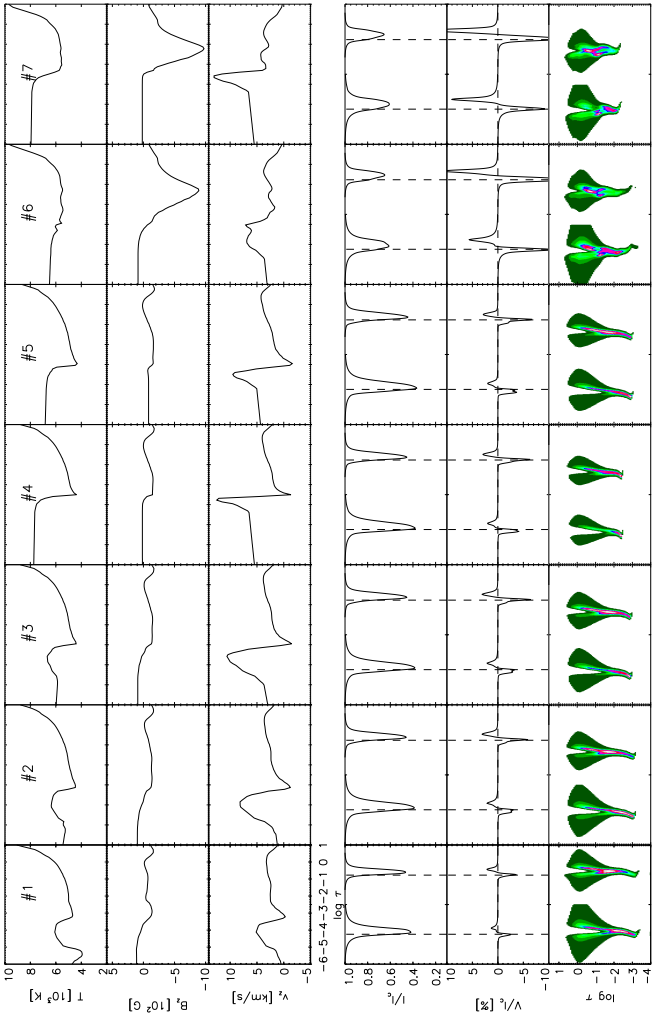

Figure 6.9: *From top to bottom:* Temperature, vertical component of magnetic field, vertical component of velocity, synthesized Stokes I and V profiles along the cuts at $t = 416,448$ s shown in Fig. 6.5. Their position is marked by green vertical lines (from top to bottom).

of sight are marked by black vertical lines in Fig. 6.5.

The Stokes *V* profiles change gradually along the cuts from the 'normal' to 'abnormal' as the field strength decreases and changes sign, and then to 'normal' again. 'Normal' Stokes V profiles possess two lobes with amplitudes of opposite sign. Profiles which strongly deviate from this shape are called 'abnormal'. Such 'abnormal' shapes result from the gradients of the components of magnetic field and velocity along the line of sight (LOS) (Illing et al. 1975, Auer & Heasley 1978, Solanki & Pahlke 1988). A temperature reversal alone is also capable of producing abnormal V profiles with multiple lobes (Steiner 2000). Stokes V profiles with emission cores have been proposed by Sanchez Almeida (1997) to explain apparent reversed chromospheric polarity in sunspots. In our cases, all physical parameters display abrupt changes along the LOS, so it is difficult to say which effect is responsible for the 'abnormal' shap of the profiles. The profiles in the atmospheres ♯1 in both figures show reversals that might be connected to the temperature increase, but strong dowflows and reversal in magnetic field profiles could also produce a similar effect. The multilobed Stokes V profiles appear where the field is mostly horizontal (as in Fig. 6.6) or changes the sign (twice) along the LOS (as in Fig. 6.7). The CFs are highly asymmetric except in atmosphere ♯5 (first column from the right) in Fig. 6.6, where there are no gradients in velocity, just a constant strong downflow along the LOS which shifts the lines towards longer wavelengths. The height of formation depends on absolute temperature and the temperature gradient, but also on the velocity profiles. The strong dowflow tends to shift the height of formation downwards.

The Stokes V profiles ♯2 and ♯3 in Fig. 6.6 are a product of the specific height profiles of the physical parameters. The vertical component of the magnetic field shows gradients along the LOS, with the upper and lower layers having opposite polarity with the field strength of up to 100 G. At intermediate optical depths $-2 > \log\tau > -1$, the vertical magnetic field is small (~ few G) and the temperature is enhanced. A similar configuration of the magnetic component along the LOS is assumed by the Rezaei et al. (2007a) in order to describe the opposite Stokes *V* polarity observed in Fe I 630.1 nm and 630.2 nm lines. However, they employ a much stronger magnetic field (with the positive polarity reaching 1500 G) and a bi-polar velocity profile (with an upflow reaching 4 km/s in the higher layers). Stratifications that somewhat resemble their assumptions can be found at $x = 0.5'' - 1.''$ in Fig. 6.5, in the regions where strong upflow appears. Some of the representative pixels, marked by the orange vertical lines, are shown in Fig. 6.8. These atmospheres exhibit a strong downflow in lower and upflow in the higher layers, and their maxima are approximately at the same optical depths as assumed by Rezaei et al. (2007a). The vertical magnetic field shows a polarity change at $-2 > \log\tau > -1$, but a case with kG field in the higher layers could not be found. As a result, we find profiles that have a different number of lobes in Fe I 630 nm lines (♯1 and ♯2 in Fig. 6.8), but no profiles with evident opposite polarity as reported by Rezaei et al. (2007a).

The Stokes profiles ♯3 (shown in the third column) in Fig. 6.8 are a particular case of abnormal profiles called one-lobed profiles - i.e. consisting of one prominent lobe, with the other one not present or very small. The literature offers different scenarios as explanation. Grossmann-Doerth et al. (2000) show that the profiles averaged over the rays passing through a magnetopause of an upward expanding magnetic flux tube can be one-lobed. Steiner (2000) suggested that a suitable change of temperature across a magnetopause can also give rise to various kinds of abnormal Stokes V profiles, including

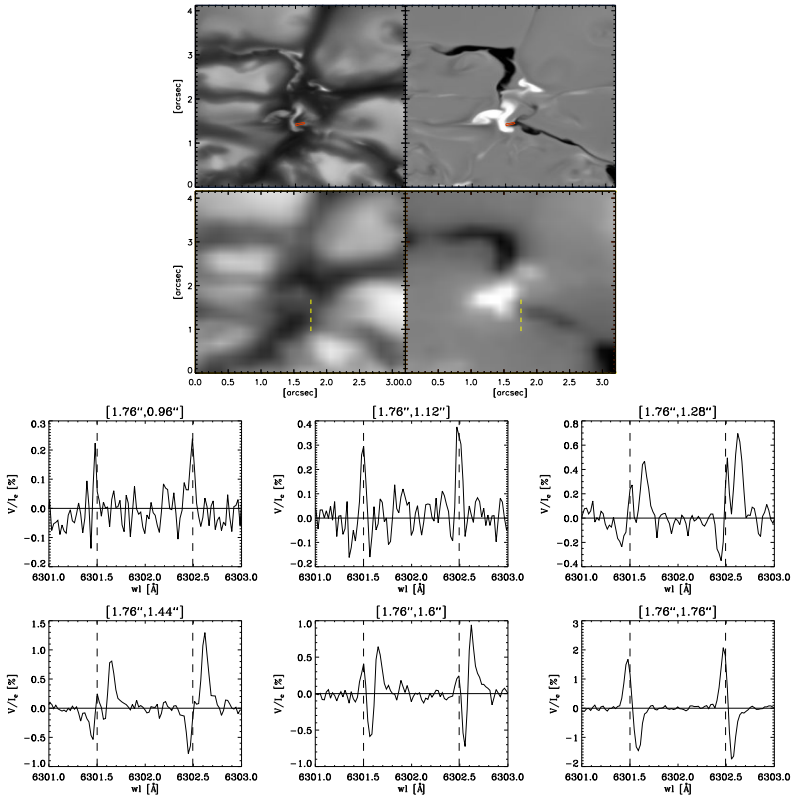

Figure 6.10: Synthesized intensity map and magnetogram from simulations, at t = 538 s. Stokes V profiles along the yellow line are shown below.

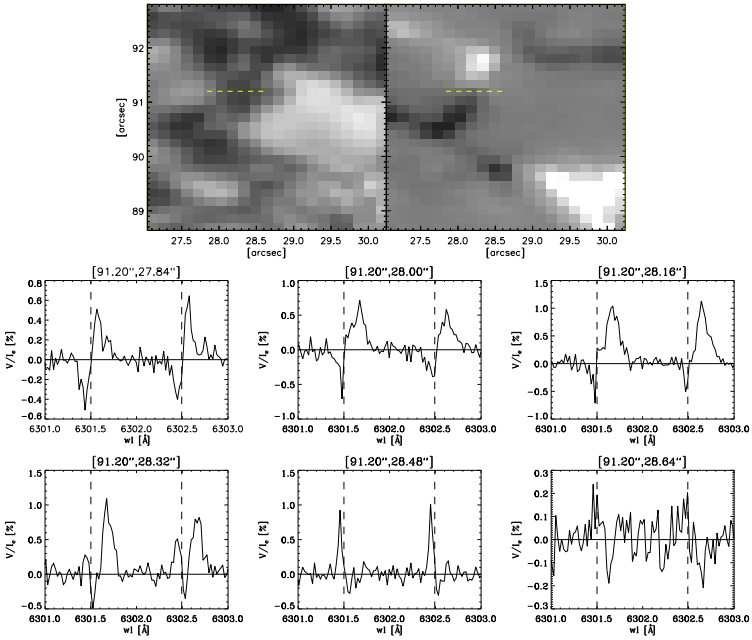

Figure 6.11: Intensity map and magnetogram observed with Hinode/SP. The maps are taken from the data set I described in Chapter 4. Stokes V profiles along the yellow line are shown below.

the one-lobed. Ploner et al. (2001) found in their 2D numerical simulations that one-lobed Stokes V profiles appear in two cases: they can form close to the magnetic concentrations where the gradients in magnetic field and velocity, caused by a magnetic interface, are present; or they can form in regions with multiple polarity reversals along the LOS, where the field is nearly horizontal and its inclination varies. The formation of profiles ♯3 in Fig. 6.8 corresponds to the former case.

Finally, Fig. 6.9 shows what happens with Stokes I and V profiles of the Fe I 630 nm lines in regions where the current sheet is formed. The CFs show a cut-off at optical depths where temperature suddenly increases by more than 2000 K. The iron atoms are ionized in these layers, so the lines do not see the strong downflow at the base of the current sheet. The Stokes I profiles are almost symmetric and redshifted, while the Stokes V profiles are 'normal', two-lobed profiles.

6.3.1 Comparison with Hinode/SP observations

Following the procedure described in the previous chapters, we degrade the synthesized Stokes profiles to the spatial and spectral resolution of the Hinode/SP, add noise of 10^{-3} I_c,

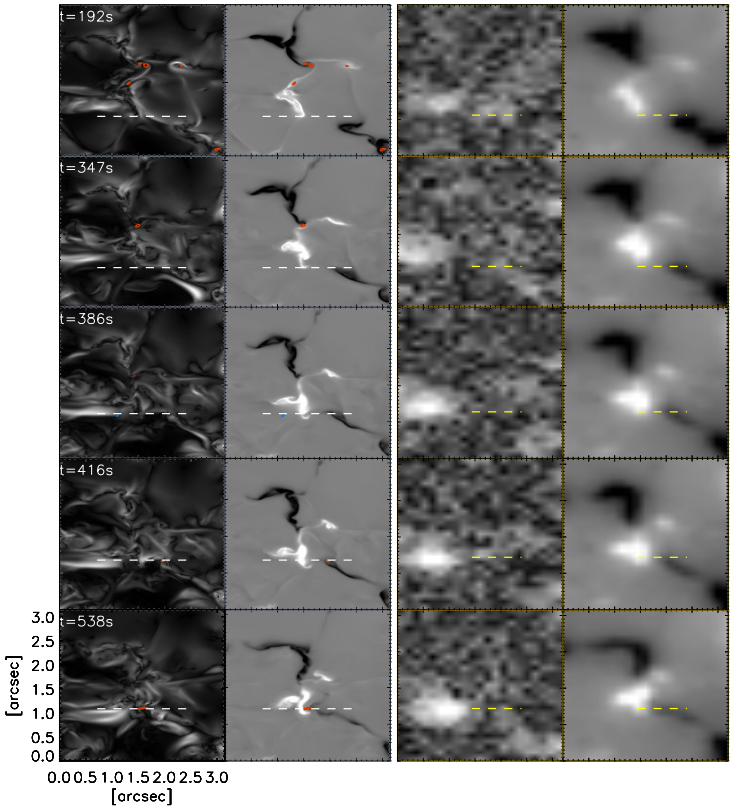

Figure 6.12: Transversal (B^T_{app}) and longitudinal (B^L_{app}) apparent magnetic flux density maps derived from synthesized Stokes profiles at original (left panels) and Hinode (right panels) spatial resolution. Horizontal lines are plotted for easer comparison.

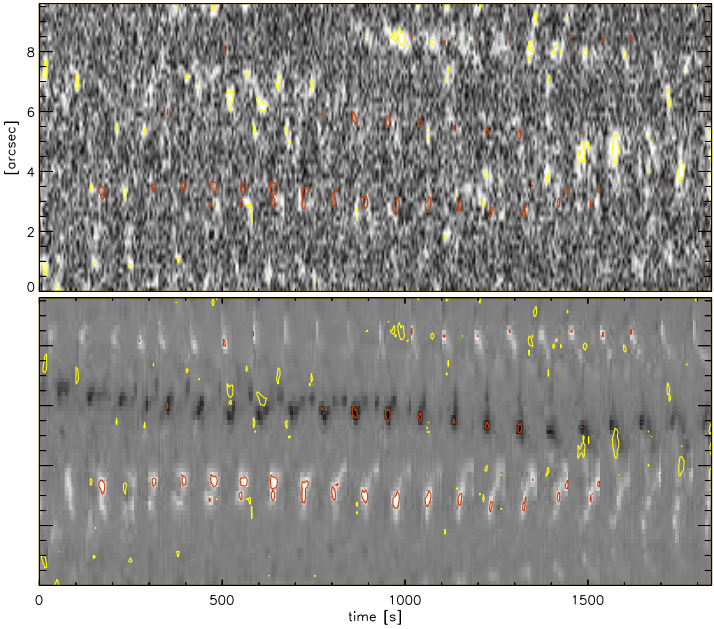

Figure 6.13: Longitudinal (lower panel) and transversal (upper panel) apparent magnetic flux density maps of the region scanned by the Hinode/SP on March 23 2008, at 10:34 UT. Yellow and red contours mark the region with $B^T_{app} \geq 150$ Mx/cm^2 and $B^L_{app} \geq 150$ Mx/cm^2, respectively.

and calculate the proxies: the longitudinal (B^L_{app}) and transversal (B^T_{app}) apparent magnetic flux densities.

After smearing, the Stokes V profiles do not show as much structure as at original resolution. In the region where the opposite polarities meet they look rather like Stokes Q profiles ('Q-like'), which are commonly observed at such sites (Rüedi et al. 1992, Sigwarth et al. 1999, Sánchez Almeida & Lites 2000, Sigwarth 2001, Khomenko et al. 2003). Figure 6.10 shows representative profiles along the 'neutral line'. Figure 6.11 shows a similar case in observations, a small region from the data set I in Chapter 4 extracted in order to compare the synthesized and observed Stokes V profiles. The figures show similar 'Q-like', as well as one-lobed profiles.

What about the linear polarization signals? Could we detect the loops retracting with time towards lower layers? Figure 6.12 shows the maps of B^L_{app} and B^T_{app} derived from the synthesized Stokes profiles at the original and reduced resolution. The B^T_{app} maps display a strong horizontal field concentration at [0.5″, 1″] during the whole period. This loop is also visible in the magnetic field strength maps in Fig. 6.5. Since it extends into the range of the optical depth where the Fe I 630 nm lines form, its presence produces significant

linear polarization signal, visible even after spatial smearing. The retracting loop, on the other hand, traverses the optical depth range probed by the lines only in the short period when higher B^T_{app} signal is visible (t = 416 s). However, the signal is smeared out and lost in the noise in the Hinode/SP simulated case.

The retracting loops, appearing in the process of flux cancellation, could explain some of the transient horizontal fields visible by Hinode/SP. Figure 6.13 presents a case which indicates such a scenario. The data set used here has been taken on March 23 2008, at 10:34UT. A region of $2.9'' \times 81.9''$ is scanned in the normal mode (exposure time of 4.8 s) with a time cadence of 86.4 s. The figure shows the evolution of B^L_{app} and B^T_{app} in the region that contains two strong vertical field concentrations approaching each other. At the moment when they are approximately $1''$ apart, a patch of horizontal field appears ($t \approx 1500$ s). Although it is uncertain without the larger field of view, the chromospheric field proxy and the velocity field whether the flux cancellation really occurs in this case, it is a likely explanation of this observation.

6.4 Signature in the intensity profiles of Fe II lines

As shown in Section 1.3, the Fe I 630 nm lines are not able to detect a presence of the current sheets formed in the upper photosphere. Here we test how strongly the Fe II 5197.58 Å and Fe II 4923.92 Å lines react to the heating associated with the formation of the current sheets. Bruls & Solanki (1993) found these lines to be sensitive to temperature changes above $\log \tau_{500} = -2$. In an attempt to put constraints on the temperature profiles in magnetic concentrations in plage and network regions, they found that, in some of the proposed model atmospheres with a chromospheric temperature rise, these lines show inversions in the line cores, also in NLTE. Figure 6.14 shows the same behavior in the simulated atmospheres that contain current sheet region presented in Fig. 6.9.

The contribution functions show that the negative contribution (i.e. emission) originates in the uppermost layers, where the temperature reversal occurs. The intensity of the emission peak increases as the temperature increases. The effect is more pronounced in the Fe II 4923.92 Å line, which forms higher up. The emission peaks are redshifted by amounts that correspond to velocities at the base of the current sheet (0.17Å $\approx$ 10 km/s).

In general, emission in the cores and inner wings is seen only in the strong chromospheric lines observed with high spatial and temporal resolution in the quiet Sun or in magnetic regions. In the quiet Sun, this is commonly associated with the dissipation of acoustic waves (Carlsson & Stein 1997). Upward travelling waves excited by the convective motions steepen into shocks which cause heating of chromospheric layers. The emission peaks are blueshifted with respect to the line core (Pietarila et al. 2007, Beck et al. 2008). In magnetic regions the emission is more symmetric. Examples of purely redshifted reversals are not so common. Rezaei et al. (2007c) observed Ca II H profiles with more pronounced red emission peak at a flux cancellation site. Sainz Dalda & López Ariste (2007) found redshifted emission in Ca II 849.8 and 854.2 nm line profiles, observed in a region which they suggest to be a site of magnetic reconnection due to loops emerging into the chromosphere. The observed profiles show features very similar to the ones shown here in the synthesized profiles of the Fe II 4923.92 Å line. The cores of the Ca II 849.8 and 854.2 lines, observed by Sainz Dalda & López Ariste (2007), are

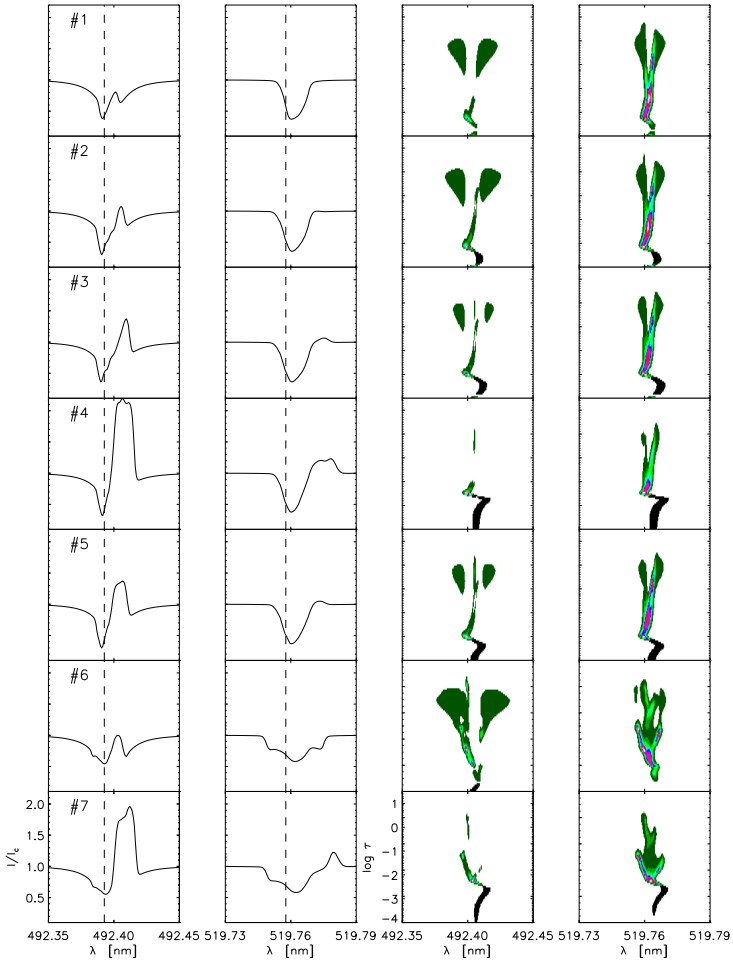

Figure 6.14: The intensity profiles (left) of the Fe II 4923.92 Å and 5197.58 Å, and the corresponding contribution functions (right) to the line depression along the same lines of sight as show in Fig. 6.9. The Fe II 4923.92 Å line is shown in the first and third column. The contribution functions show the negative contribution (i.e. emission) marked in black.

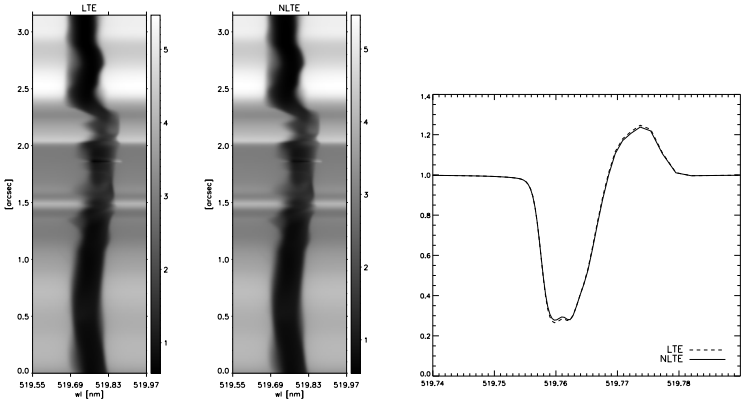

Figure 6.15: On the left, the synthesized slit spectra of Fe II 5197.58 Å line with and without the assumption of LTE, along the cut at $t = 416$ s shown in Fig. 6.5. On the right, a comparison of the profiles calculated with and without assumption of LTE in the atmosphere ($y = 1.85''$) that contains the current sheet.

blueshifted and a small emission peak appears in the red wing of the lines (more pronounced in Ca II 854.2 nm). Similar features in Ca II 854.2 nm line profiles are found also by Uitenbroek et al. (2006) in a region between magnetic field patches of opposite polarity, but they gave a different explanation for the appearance of such profiles. Taking the center of gravity method, they retrieved a positive (upward directed) LOS velocity from these profiles and interpreted it to mark the location of an upstream footpoint of a siphon-driven flow from a patch of weaker positive polarity to the stronger field of opposite polarity.

Observations obtained in the Ca II 854.2 nm line by Tritschler et al. (2008) suggest the presence of a current sheet above the sunspot's umbra due to a brightening in the line core. They find 400 km to be a lower boundary and 800 km to be an upper boundary of the current sheet. These heights are retrieved by associating the wavelengths exhibiting the enhanced brightness to the specific heights. The relation of wavelength to formation height is retrieved from the line intensity contribution function calculated in a 1D sunspot model atmosphere. The results presented in this chapter show that this may not be the correct way to retrieve the location of the current sheet, since the presence of a strong downflow may significantly change the contribution of different atmospheric layers.

The Fe II 5197.58 Å and 4923.92 Å lines, shown in Fig. 6.14 have been synthesized under the assumption of the LTE. Would their behavior be different if non-LTE effects were taken into account? Bruls & Solanki (1993) treated these lines in non-LTE and concluded that Fe II 5197.58 Å is not strongly affected. The source function of Fe II 4923.92 Å, on the other hand, deviates from LTE in the line center formation regions, which are, in the quiet Sun atmosphere they used, situated at optical depths $\log \tau_{500} > -4$. In our case, these are the layers where current sheets are formed. In the same layers, the density is also significantly increased, so the collisions could actu-

ally couple the level populations to the local temperature and hence bring the formation of Fe II 4923.92 Å line close to LTE. This, however, should be tested. Here, we have synthesized only Fe II 5197.58 Å in non-LTE by using RH code (Uitenbroek 2001) and a 35-level model atom[2]. Figure 6.15 shows the slit spectra along the cut at $t = 416$ s from Fig. 6.5. The positions where the line is redshifted correspond to the locations with strong downflow (roughly $y = 1.5'' - 2.5''$). The increase in continuum intensity follows the increase in temperature at the $\log \tau_{500} = 0$ level. Hence, the bright stripe at $y = 1.5''$ is located where the $\log \tau_{500} = 0$ level shifts downwards, in the magnetic concentration with positive polarity. Also, there is an increase in continuum intensity for $y > 2.0''$ where the concentration with negative polarity begins and the $\log \tau_{500} = 0$ levels changes abruptly. The current sheet location covers a few pixels around $y = 1.85''$ that exhibit emission in the red. The plot on the right shows the profiles at one of these pixels. The profiles calculated in LTE and NLTE are plotted together. There is almost no difference. The emission peak appears in both cases with the same intensity. The Fe II 5197.58 Å source function follows the Planck function almost perfectly, in agreement with the results of Bruls & Solanki (1993).

6.4.1 Simulating observations with the Swedish Solar Telescope (SST)

To check if the signature would survive spatial smearing we simulate observations with the Swedish Solar Telescope (SST) by applying an appropriate PSF on the synthesized data. For this, we use a theoretical PSF that consists of a diffraction core and a seeing halo, which has the form of a Lorentzian (Nordlund 1984). This PSF is commonly used for the comparison with the ground based observations (Schüssler et al. 2003, Leenaarts & Wedemeyer-Böhm 2005, Langangen et al. 2007). The PSF has two free parameters: the width of the Lorentzian (b) and the fraction of the Lorentzian component compared with the Airy core (a). Different combinations of these parameters - a wider Lorentzians with a smaller fraction or a narrower Lorentzian with a larger fraction act in a similar fashion. Figure 6.16 shows the Modulation Transfer Function (MTF) of two combinations of these parameters which affect the contrast by different amounts. The aperture of SST is 1 m, which, operating at 500 nm, provides a spatial resolution of $\sim 0.103''$ (equivalent to $\sim$ 75 km on the solar surface). Thus, the cut-off is at $1/0.103''$ and higher spatial wave numbers are not transmitted by the system. Applying just the Airy function on the synthesized data would lower the original granulation contrast of 14% to 11.2%. Adding the Lorentzian with parameters $a = 0.001$ and $b = 1000$ km decreases it to 7.1% and the Lorentzian with parameters $a = 0.01$ and $b = 500$ km decreases it to 4.8%.

Figure 6.17 shows the effect that spatial smearing has on the observed spectra. Two-dimensional maps showing the intensity in the red wings of the lines (wavelengths that correspond roughly to a downflow velocity of 10 km/s) are displayed after applications of different PSFs. At the original resolution, the location of current sheets is clearly visible in the maps. A decrease in the spatial resolution produces a decrease in the contrast of these regions with respect to their surroundings. The effect is more pronounced for the Fe II 5197.58 Å line. Representative profiles for each case are given in Fig. 6.18. The signature

[2]Courtesy of J. H. M. J. Bruls. The iron model atom is tailored so that it represents the essential non-LTE effects influencing the formation of this line. It consists of 18 Fe I terms, 16 Fe II terms and the Fe III ground state, and their radiative transitions.

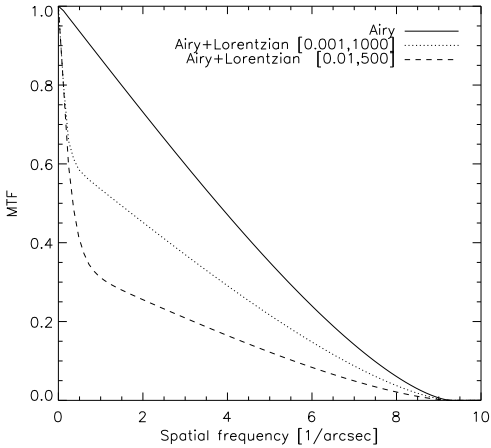

Figure 6.16: The change of the Modulation Transfer Function when the effects of the terrestrial atmosphere are taken into account: SST telescope aperture ('Airy'), plus the Lorentzian with $a = 0.001$ and $b = 1000$ km, or plus the Lorentzian with $a = 0.01$ and $b = 500$ km.

in the Fe II 5197.58 Å line is significantly reduced already in the diffraction-limited case. A very small peak in the red high wing is visible, but it disappears completely as the resolution decreases. The core of the line is shifted bluewards and the line profile becomes more symmetric. In the case of Fe II 4923.92 Å line, the intensity reversal remains visible in some cases (the upper right panel in Fig. 6.18) even when the smearing is most severe.

Finally, we took a spectrogram taken with the TRI-Port Polarimetric Echelle- Littrow (TRIPPEL)[3] spectrograph mounted on the SST to estimate the granulation contrast reachable by observations. Figure 6.19 shows the observed spectral range that contains the Fe II 4923.92 Å line, corrected for the dark currents, flat fields and smile deformation of the spectra[4]. Taking a small spectral range that does not contain any spectral lines gives the granulation contrast of 6.7%. Thus, applying the Lorentzian with $a = 0.001$ and $b = 1000$ km would be sufficient. In the lower panel of the Fig. 6.19, the spectra averaged along the slit are show together with the Fourier transform spectrograph (FTS) atlas (Brault & Neckel 1987). Note that the result shown is just preliminary, hence the discrepancies in the continuum level and line depths in the observed spectra with respect to the one from the Atlas. A careful treatment of the observed spectra is necessary (i.e. accounting for the light scattered in the spectrograph) for further analysis. Overplotted in green in Figure 6.19 are the profiles of Fe II 4923.92 Å and its neighboring Fe I lines

[3]TRIPPEL is a Littrow spectrograph using a 79 grooves/mm Echelle grating with a blaze angle of 63.43°. The effective theoretical spectral resolution, R= 234000, which gives spectral resolving power of 21 mÅ at 500 nm.

[4]Courtesy of T. Riethmüller.

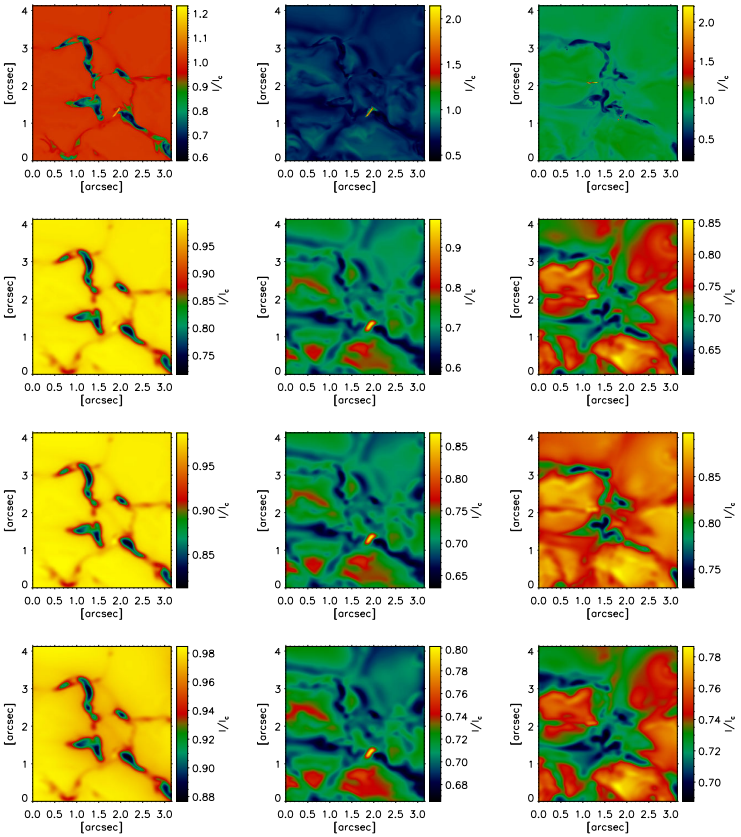

Figure 6.17: 2D intensity maps at the wavelengths in the red wings of Fe II 5197.58 Å line (left column) and Fe II 4923.92 Å at t = 416 s (middle column) and t = 538 s (right column). Change of the intensity profiles when the effects of the terrestrial atmosphere are taken into account: original (first row), SST telescope aperture (second row), plus the Lorentzian with a = 0.001 and b = 1000 km (third row), or plus the Lorentzian with a = 0.01 and b = 500 km (fourth row).

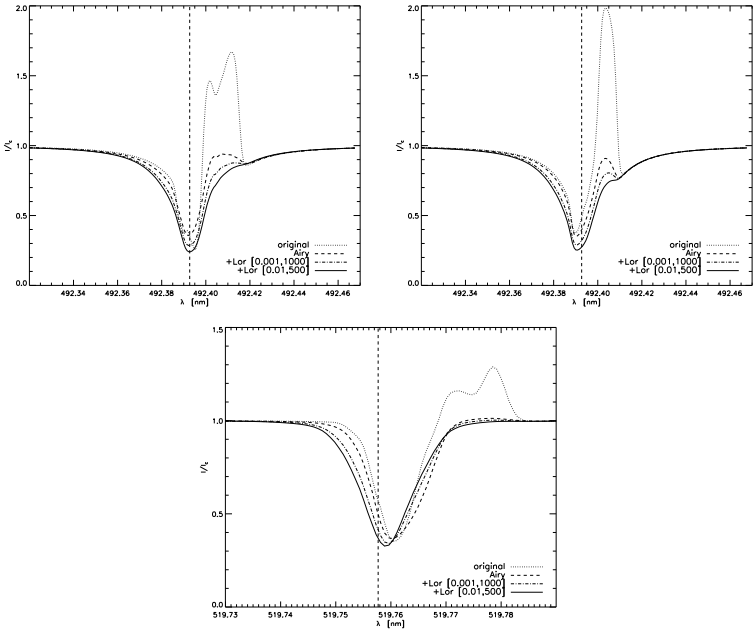

Figure 6.18: The change of the intensity profiles of the Fe II 5197.58 Å (lower panel) and Fe II 4923.92 Å (upper panels) when the effects of the terrestrial atmosphere are taken into account: SST telescope aperture ('Airy'), Lorentzian with $a = 0.001$ and $b = 1000$ km, and Lorentzian with $a = 0.01$ and $b = 500$ km. Representative profiles from the corresponding maps shown in Fig. 6.17.

(listed in Chapter 2) in one of the atmospheres that contains a current sheet (at $t = 538$ s). The signature that we might be looking for is a small reversal visible in the red wing of the Fe II 4923.92 Å. A similar feature appears also in the neighboring Fe I 4920.50 Å line. As shown in Chapter 2, this line forms roughly at the same height as Fe II 4923.92 Å, near the upper boundary of the simulation domain. Synthesized in LTE, the line sees the temperature reversal and velocity at the base of the current sheet. However, it is not certain if the NLTE effect would not change the result considerably.

6.5 Conclusions

In this chapter an example of flux cancellation from the MURaM simulations has been analyzed. The event involves the formation of a current sheet (where magnetic energy is dissipated and the temperature increases steeply), followed by the retraction of the inverse U loops that connect magnetic concentrations with opposite polarity.

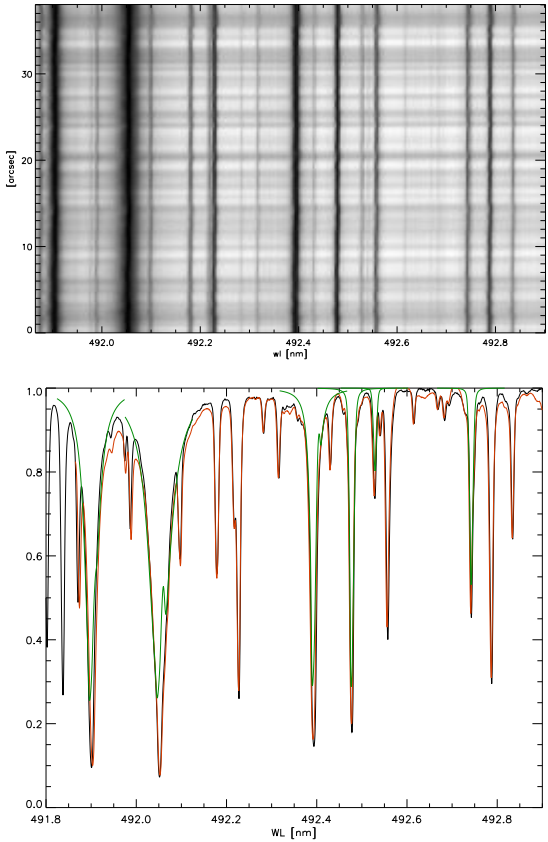

Figure 6.19: Upper panel shows the spectral range in the vicinity of Fe II 4923.92 Å recorded with the TRIPPEL spectrograph mounted on SST. The lower panel shows a comparison of the observed line profiles averaged along the slit (red line) with the synthesized profiles (green line). The PSF including a Lorentzian with $a = 0.001$ and $b = 1000$ km is applied to the synthesized maps. The representative line of sight at $t = 538$ s shown in Fig. 6.18 (rightmost panel) is taken. The black line shows the FTS atlas profiles.

The spectropolarimetric signatures in the Fe I 630 nm lines have been considered. At the original resolution, the Stokes V profiles exhibit various abnormal shapes at locations where the magnetic field changes polarity. After spatial smearing to Hinode/SP resolution, they are transformed into 'Q-shaped' profiles, commonly observed in mixed polarity regions. The linear polarization signals increase at the original resolution as the loops pass through the height where Fe I 630 nm lines are formed. The signal is smeared out and lost in the noise at Hinode/SP spatial resolution. No Stokes V profiles that show opposite polarity in Fe I 630.1 nm relative to Fe I 630.2 nm line are found in simulations, although the height profiles of the physical parameters resemble that assumed by Rezaei et al. (2007c).

Due to their low formation height, the Fe I 630 nm lines do not reflect the presence of the current sheets in the layers $\log \tau_{500} > -2$. However, their presence is revealed in Fe II 5197.58 Å and 4923.92 Å in the form of an emission peak in the red wings of these lines. It appears due to an abrupt increase of the temperature with height. The position of the peaks is correlated with the velocity field at the base of the current sheets. When spatial smearing is applied, the signature is reduced and transformed into an intensity reversal in the red wing of the line (for Fe II 4923.92 Å), or is removed completely (in case of Fe II 5197.58 Å). Preliminary comparison of the spectral range that contains Fe II 4923.92 Å, synthesized in LTE, with the observations carried out with TRIPPEL spectrograph mounted on the SST, imply that the detection of the effect could be posible. The study of the quiet Sun magnetic field topology based on Hinode observations, on the other hand, shows that the null points are mainly located in the photosphere (Régnier et al. 2008). This leads to the conclusion, that the sites where the signature might appear could be ubiquitous and we should detect at least some percentage.

7 Outlook

The observations recorded with the spectropolarimeter onboard Hinode satellite have revealed a wide range of information about the structure of the photospheric magnetic field (Tsuneta 2008, de Wijn et al. 2009). In this thesis, it has been shown that the 3D radiative MHD simulations carried out with the MURaM code quantitatively reproduce some of these observations. However, the Hinode/SP pixel size ($\approx$ 120 km) is still far from the grid cell size of the 3D radiative MHD simulations ($\approx$ 5 km), or the scales of magnetic structures in the photosphere ($\approx$ 20 km) (Pietarila et al. 2008, Pietarila Graham et al. 2009). With a resolution of $\approx$ 40 km at 220 nm, the Sunrise mission[1] will get closer to these values. By employing instruments IMaX[2] and SUFI[3] onboard Sunrise, the work presented in this thesis could be tested and extended:

(1) With a proper consideration of the effects of the optical system, the properties of the observed and synthesized granulation contrast as a function of heliocentric position could be obtained (as done by Wedemeyer-Böhm & Rouppe van der Voort (2009) for the case of the Broadband Filter Imager (BFI) onboard Hinode).

(2) A quantitative comparison of local dynamo simulations with the IMaX observations could be performed by taking spatial and spectral resolution and noise into account. The information about the mean magnetic field strength and the spatial distribution of magnetic field on the smallest scales could be retrieved.

(3) IMaX should provide a long observational time series of $50'' \times 50''$ regions with a high temporal cadence. This would enable a statistical study of the magnetic field intensification and the formation of bright points. The occurrence and properties of upflows developed during these events could be obtained.

(4) The retraction of the inverse U-loops during flux cancellation events might be visible owing to the wide FOV and high temporal resolution of IMaX. However, it is unclear to what extent the chosen spectral line, Fe I 525.02 nm, which is highly temperature sensitive, will respond to such an event. Simultaneous observations with the SUFI filter in Ca II H line at 396.8 nm could trace the presence of current sheets.

The work on magnetic reconnection in the photosphere will be extended by analyzing data obtained with the TRIPPEL spectrograph attached to the SST. The data consist of

[1]The Sunrise is a 1m balloon-borne optical solar telescope with a set of instruments for the visible and UV. It is planned to fly in on circumpolar trajectory in order to provide uninterrupted time series of diffraction limited images and magnetograms of the Sun (Gandorfer et al. 2004).

[2]Imaging Magnetograph Experiment (IMaX) will provide high-cadence 2D maps of the complete magnetic vector and the line-of-sight velocity with a high spatial resolution. The narrowband filtergrams will be taken at 5 wavelength positions in the Fe I 525.02 nm line.

[3]SUNRISE Filter Imager (SUFI) will take images of the solar surface in 5 distinct wavelength bands in the UV with the FOV of $35'' \times 17''$.

spectrograms taken simultaneously in the spectral ranges containing the Fe II 4923.92 Å and Mg I b2 517.27 nm lines. Both lines are sensitive to temperature variations at optical depths $\log \tau > -2$ (Bruls & Solanki 1993, Briand & Solanki 1995). Also, the information about the photospheric magnetic field is simultaneously obtained by the polarization signal in the Fe I 630.25 nm line. The scans are taken across the region where a bipolar magnetic structure emerges and also in the vicinity of a sunspot moat. Both locations have potential suitability for the detection of magnetic reconnection events (Guglielmino et al. 2008, Bellot Rubio & Beck 2005). The potential of the Ca II 854.2 nm line and the IBIS instrument (Cauzzi et al. 2008) should be considered for the detection of current sheets in the chromosphere. Alternatively, this line can also be observed with the CRISP Imaging Spectropolarimeter at the SST (Scharmer et al. 2008, de La Cruz Rodriguez & van Noort 2008).

A The Solar Cycle Variation of the Mn I 539.4 nm line

A.1 Introduction

Solar irradiance measurements show variation on time scales from minutes to decades. For variations on time scales of a day to the solar-cycle, different causes have been proposed: changes of internal thermal structure of the Sun, subsurface fields or changes of the magnetic field on the solar surface (see Solanki et al. 2005, for a review). The third explanation has found considerable support. In particular the SATIRE model, where SATIRE stands for Spectral And Total Irradiance REconstruction, has been successfully used to describe variability of total irradiance changes during the last 3 cycles, so that at least 90% of the variable TSI (Total Solar Irradiance) can be assigned to the changes of surface magnetism (Krivova et al. 2003, Wenzler et al. 2005, 2006). Since in its current form the SATIRE model contains a free parameter, it can be argued that the case for a solar surface cause of TSI is not entirely clear cut. It is therefore important to reproduce also spectral features. This has been done for the VIRGO (Variability of IRradiance & Gravity Oscillations; Fröhlich et al. 1995) color channels by Krivova et al. (2003), UV irradiance (Krivova et al. 2006) and for spectral irradiance over a broad wavelength range on solar rotation time scales (Unruh et al. 2008). In this section, we will use this model to describe solar cycle variability of Mn I 539.47 nm and two neighboring neutral iron lines, which provides additional constraints to the model. Modelling the solar cycle variation of spectral lines is of particular importance since spectral lines are estimated to contribute 50 – 75% of the TSI variations over the solar cycle (Mitchell & Livingston 1991, Unruh et al. 1999).

The Mn I 539.47 nm line is interesting for several reasons. The hyperfine broadening, due to the interaction of the electronic shell with the nuclear spin, makes it insensitive to non-thermal motions in the photosphere (Elste & Teske 1978, Elste 1986). This was recently confirmed by Vitas et al. (2009) on the basis of realistic 3D MHD simulations. They showed that as opposed to the narrow Fe I 539.52 nm line, the Mn I 539.47 nm line is not smeared by convective motions. Thus the line becomes stronger in sunspots and weaker in plage and network, as shown by observations (Vince et al. 2005a,b, Malanushenko et al. 2004). So although it is formed in the photosphere (Gurtovenko & Kostyk 1989, Vitas 2005), the 'Sun-as-a-star' observations (Livingston & Wallace 1987, Livingston 1992) exhibit a significant cyclic dependence, not typical of the other photospheric lines that were recorded in parallel. A time series analysis shows that around solar activity maximum even variations on the solar rotation time scale can be found (Danilovic et al. 2005).

The other explanation of this chromospheric-like behavior is proposed by Doyle et al. (2001). They found that optical pumping by Mg II k, could be the reason why this Mn line mimics the change seen in Mg II k. On the other hand, the analysis of Vitas & Vince (2007) shows that the Mn I 539.47 nm line is insensitive to the photons emitted in the cores of Mg II h & k.

The more probable explanation is that the high correlation between the Mn I 539.47 nm line and chromospheric proxies may be a consequence of the common source of change in both cases: bright magnetic elements - faculae and network (Danilovic & Vince 2005). Here, we try to confirm this hypothesis by using the SATIRE model to, for the first time, reconstruct the cyclic behavior of the Mn I 539.47 line. As an additional test of the method we analyze the spectral range in the vicinity of this line, which contains 2 Fe I lines, recorded in the 'Sun-as-a-Star' observations obtained by W. Livingston.

The structure of the section is as follows: the observational data set and modelling technique are described in Sect. A.2. The disk-averaged line synthesis is treated in Sect. A.3.1. The calculated center-to-limb variations of the line profiles are given in Sect. A.3.1. Results for different observational phases (before and after 1992) as well as for three solar cycles are discussed in Sect. A.3.3. Concluding remarks are given in Sect. A.4.

A.2 Observational data and modelling technique

A.2.1 Data

The observational data modelled here were obtained with the Kitt Peak McMath telescope 13.5 m scanning spectrometer in double pass mode (Brault et al. 1971). The sunlight was delivered to the spectrograph without any prefocusing. There a 0.5x10 mm entrance slit formed a pinhole image of the Sun on the grating (camera obscura principle). This specific instrumental set gave the disk integrated or 'Sun-as-a-star' spectrum.

The 2 Å wide spectral range around the Mn I 539.47 nm line was observed in 5th order of the grating which gave the spectral resolution of around 106000. Line intensities and equivalent widths were automatically extracted using the data reduction program developed by J. Brault at Kitt Peak (Brault et al. 1971). For the continuum normalization the data point at 539.491 nm is used because the comparison with the Kitt Peak spectral atlas of Wallace et al. (2007) shows that it is entirely free of telluric blends, whereas most other (pseudo-)continuum wavelengths are affected. The intensity values at this wavelength are normalized to unity. This might be slightly too high, as a comparison with FTS spectra shows (Fig. A.3). However, tests have shown that any small error introduced by this normalization does not affect the results in any significant way. A quadratic fit to the cores of each of the lines is made and the line's central depth is defined as the difference between the minimum of the fit and normalized continuum value. Equivalent width is calculated within given wavelength ranges (shown later in Fig. A.3).

A first set of observations with an unchanged setup was taken from 1979 to 1992, with recordings being made a few times per month. In 1992 a new larger grating with dimensions 42×32 cm^2 was installed, compared with 25×15 cm^2 for the grating mounted prior to 1992. This instrumental change had a measurable effect on the data. Before the

change, part of the solar limb fell outside the grating, whereas with the new grating, the full solar disk was sampled. This introduced a 'jump' in the measured equivalent width (EW) and central depth (CD) of lines obtained before and after 1992. After mounting experimental period with the new grating lasted till 1996 when the system was fixed and observations are performed regularly again. However, constant re-alignment of the system between 1996 and 1998 led to an increased variance in the parameters of the recorded spectral lines. As a result, we analyzed and modelled observations recorded on 465 days from January 1979 till September 1992 and on 187 days in the period from September 1998 till May 2004. Between September 1992 and September 1998, observations were obtained on 45 days. These were not taken into account in the work described here.

A.2.2 SATIRE Model

The SATIRE (Spectral And Total Irradiance REconstruction) model described by Fligge et al. (2000) and Krivova et al. (2003) assumes that solar irradiance change can be explained by evolution of the solar surface magnetic field. The model categorizes all surface features in four groups based on their brightness and magnetic flux density. The area with brightness below a given threshold is identified as area covered by sunspots. These are further partitioned into umbrae and penumbrae depending on the brightness level. Facular regions are classified as areas that have magnetic flux density above a threshold, which are not sunspots and pores. The areas that do not fulfill any of these criteria are classified as quiet Sun. For the feature identification, in the period from 1978 to 2003, full-disk magnetograms and continuum images recorded with the 512 channel magnetograph and the spectromagnetograph, mounted on the Kitt Peak Vacuum Tower Telescope, are used. Detailed description of data calibration is given in Wenzler et al. (2004, 2006).

Since the spatial resolution of maps is of the order of a few arcsec, the model takes into account the fact that magnetic elements in faculae are not fully resolved by introducing a filling factor. It increases linearly with magnetic flux density and reaches unity at a magnetogram signal of B_{sat}. For $B > B_{sat}$ the filling factor remains constant at 1. B_{sat} is the only free parameter in the SATIRE model. The value of $B_{sat} = 320\,G$ used here is the same as in Wenzler et al. (2006), which gave the best match to the total solar irradiance change during solar cycles 21-23.

The stratification of physical parameters with depth is assumed to remain unchanged over the solar cycle and is represented by one dimensional model atmospheres (Unruh et al. 1999). Kurucz' standard solar atmosphere is used for the quiet Sun and stellar models with gravitational acceleration of log g= 4.5 m/s^2 and effective temperature of 4500 K and 5400 K are used for umbrae and penumbrae respectively. The model atmosphere for the faculae is the FALP from Fontenla et al. (1999), but without the chromospheric temperature increase and with a slightly smaller temperature gradient in the lower atmospheric layers. These changes provide a good agreement of synthesized and observed facular contrast in the optical range.

A.2.3 Spectral line calculations

The KP spectra containing the Mn I 539.47 nm line also include two Fe I lines. These lines exhibit smaller variations over the solar cycle, allowing them to be partially used to

Table A.1: Line characteristics: wavelength, transition, oscillator strength and excitation energy.

line	transition	log gf	χ [eV]
Fe I 539.3167 nm	$z^5D_3 - e^5D_4$	−0.762	3.24
Mn I 539.4677 nm	$a^6S_{5/2} - z^8P^0_{7/2}$	−3.453	0.0
Fe I 539.5215 nm	$z^5G_2 - g^5F_1$	−1.763	4.44

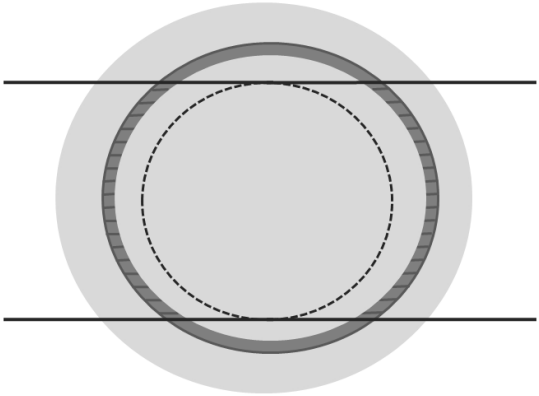

Figure A.1: Illustration of flux calculations for the period before 1993 when the old grating was used. The two horizontal lines bound the part of the disk that illuminates the grating. The dashed circle correspond to $\mu = \mu_{cut}$.

check for changes in instrumentation etc. The main characteristics of all three lines, taken from the VALD database (Kupka et al. 1999), are given in Table A.1.

The procedure of calculating disk-integrated flux in this spectral range is as follows: Time independent emergent intensities of the Mn I line and the neighboring Fe I lines are calculated in LTE for each model atmosphere for various heliocentric angles using the SPINOR code (Frutiger et al. 2000). No magnetic field is introduced in the calculations. The hyperfine structure of the Mn I line is included as blends with displacements calculated using the hyperfine constants from Davis et al. (1971) and Brodzinski et al. (1987) and relative intensities of the components from Condon & Shortley (1963). Components that are closely spaced with respect to the total splitting have been combined to reduce the computing effort. Emergent intensities, output from SPINOR, are then combined with the relative contributions of different features for different heliocentric angles.

Prior to 1993, the incomplete sampling of the solar disk by the grating had to be taken into account. Figure A.1 illustrates the simple method that we applied. We assume that

Table A.2: Fitted values of oscillator strengths and macroturbulence for disk center. The rightmost column lists the height of formation of the line cores in the quiet Sun atmosphere.

line	log gf (fitted)	v_{macro} [km/s]	fh [km]
Fe I 539.3167 nm	−0.723	1.389	397
Mn I 539.4677 nm	−3.471	0.922	197
Fe I 539.5215 nm	−1.649	0.916	111

the part of the image of the solar disk bounded by the two horizontal lines covers the grating while the rest is lost due to the size of the grating. Let μ_{cut} be the cosine of the a priori unknown heliocentric angle for which the disk image fully covers the grating. Flux coming from, for example, the region shaded dark gray in the figure, which corresponds to $\mu < \mu_{cut}$, is partially lost. For each of these 2 degrees wide regions we introduce coefficients proportional to the annular surfaces that lie in between the horizonal lines (shaded with small horizontal lines). The radiative flux coming from the whole annulus is multiplied by this coefficient. The coefficients are normalized such that the sum over all coefficients for every region at $\mu < \mu_{cut}$ is unity. In this way, we do not specify which specific parts of the solar disk (heliographic latitudes and longitudes) are sampled and which are not. This treatment is appropriate since, due to the McMath telescope being fed by a heliostat, the grating received light from different parts of the solar disk during the day. Finally, the total flux at each wavelength position is obtained by summing up the fluxes multiplied by the corresponding coefficients from all heliocentric angles.

A.3 Results

Before computing the time series of the line depths and equivalent widths of the disk-integrated profiles of the 2 Fe I lines and the Mn line, we first need to make sure that the lines are computed properly, i.e. the measured profiles of line intensity are accurately reproduced. We first compute the lines at disk center, determine their contribution functions and log $gf\epsilon$ values (gf is the oscillator strength times the statistical weight of the lower level of the transition and ϵ is the abundance). In the second step we compare their center-to-limb change (CLV) with measurements, and finally, we compute the time series of the flux computed with the SATIRE model.

A.3.1 Line profiles at disk center

Employing elemental abundances from the literature and the quiet Sun model atmosphere, we reproduce the FTS atlas profiles (Wallace et al. 2007), recorded in quiet Sun at the disk center by allowing the oscillator strengths and macroturbulence broadening velocity to vary. A Gaussian profile is chosen for the macroturbulence. The best fit values are given in Table A.2. The chosen abundances of Mn and Fe, which are kept constant, are $\log \epsilon_{Mn} = 3.39$ and $\log \epsilon_{Fe} = 7.5$ (Bergemann & Gehren 2007, Shchukina & Trujillo Bueno 2001). For the case of the strong Fe I 539.32 nm line, we introduced a damping

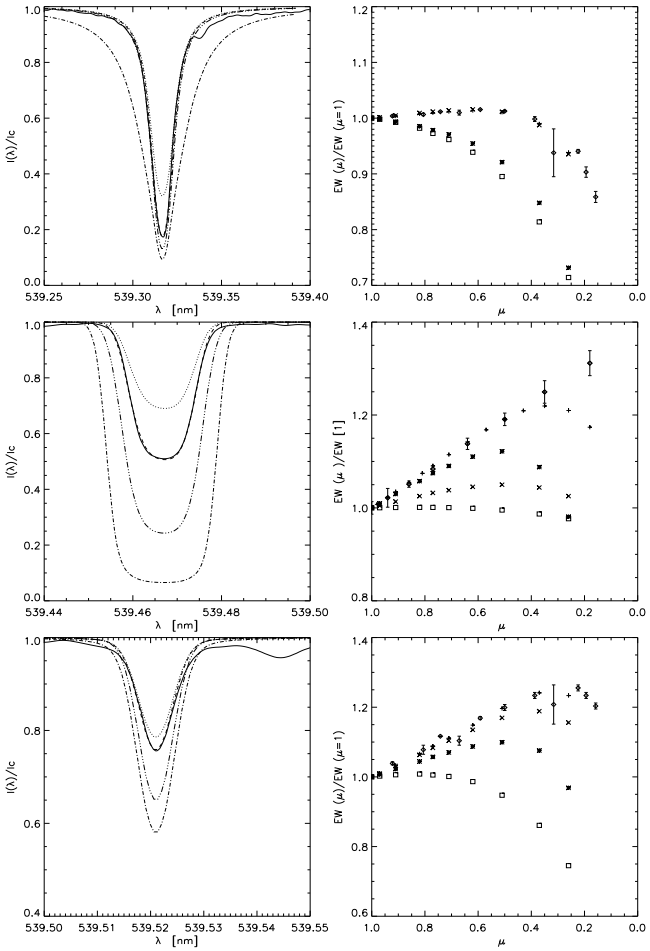

Figure A.2: *Left-hand side*: Profiles of Fe I 539.32 nm, Mn I 539.47 nm and Fe I 539.52 nm lines at the disk center, from top to bottom respectively. The profiles are computed in the following model atmospheres: quiet Sun (dashed), faculae (dotted), penumbrae (double-dot-dashed) and umbrae (dashed-dotted). FTS atlas profiles are overplotted (solid curves). *Right-hand side*: Center-to-limb variation of EW of the lines. Symbols distinguish between EW resulting from different model atmospheres: quiet Sun (plus signs), faculae (asterisks), penumbrae (crosses) and umbrae (squares). Diamonds with error bars are values observed in the quiet Sun.

enhancement factor of 3 to fit the line wings. The fitted $\log gf$ values differ from the ones taken from the VALD (Table A.1) by about 0.1 dex or less. The computed and measured line profiles agree rather well (except in the wings where these lines are influenced by blends), as can be seen from Fig. A.2 (left panel; compare the solid with the dashed line). The best fit oscillator strengths and macroturbulence values are retained when line profiles are subsequently calculated in all other model atmospheres. The results are shown in the same figure. All three lines display qualitatively the same dependence on temperature. They become stronger in umbrae and penumbrae and weaker in faculae. The magnitude of the temperature dependance is quite different, however, with the Mn line showing by far the largest temperature sensitivity, both in line depth and equivalent width. Resulting formation heights (fh) of the line cores in the quiet Sun model atmosphere, as deduced from line depression contribution functions (Magain 1986, Grossmann-Doerth et al. 1988), are given in Table A.2. The strong Fe I 539.32 nm line is thus formed significantly higher than its neighbors. The obtained heights of formation are in agreement with the previously determined values (Balthasar 1988, Gurtovenko & Kostyk 1989, Vitas 2005).

A.3.2 Center-to-limb variation

In a next step we computed the center-to-limb behavior of the three lines and compared it with center-to-limb observations. A lack of recording of these lines at different limb distances forced us to use the only two data sets available for these lines: Rodriguez Hidalgo et al. (1994) and Balthasar (1988) for Mn and Fe lines, respectively. Calculated and observed equivalent width change from disk center to the limb are shown in Fig. A.2 (right-hand panels).

The variations in the center-to-limb behavior of the lines reflect their different sensitivities to the physical parameters and velocity fields. The later is the important difference between Fe and Mn lines. As shown by Asplund et al. (2000), in order to reproduce the observed Fe line profiles at various heliocentric angles, one has to take into account a more realistic representation of the solar atmosphere, which includes surface convection and hence gives proper line broadening due to small and large scale velocity fields. Since we use one-dimensional plane-parallel models, we follow the classical method and introduce a microturbulence that increases with heliocentric angle. In this way the larger non-thermal broadening towards the limb, produced by the large horizontal velocities in the granulation, is mimicked. The values that give the best match to observations are of the same order as found by Holweger et al. (1978). For the strong Fe line, it increases from 0.1 km/s to 1 km/s, while for the weak Fe I 539.52 nm line, it grows from 1.5 km/s to 2.4 km/s (we assumed a linear increase with μ). These values are determined for quiet Sun and then maintained for the other model atmospheres.

The Mn line is, in contrast, intrinsically broad and hence all broadenings caused by velocity fields are negligible. The synthesized center-to-limb change for this line in the quiet Sun model atmosphere is in agreement with observations without any additional microturbulence change.

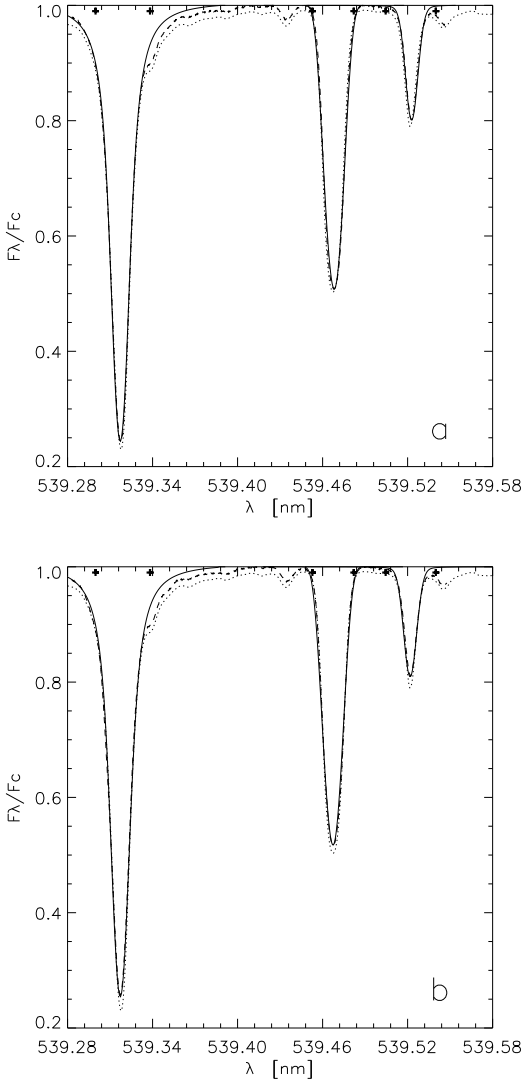

Figure A.3: Synthesized line profiles (solid) and the same spectral range observed (dashed) on May 19th 1999 (upper) and May 8th 1986 (lower). The disk-averaged FTS atlas is overplotted in both panels (dotted). Crosses mark the wavelength ranges used for the calculation of the line equivalent widths.

Table A.3: Combined macroturbulence and instrumental broadening velocity needed too reproduce the line profiles in periods before and after the change of grating, respectively.

line	before [km/s]	after [km/s]
Fe I 539.32 nm	2.04	1.69
Mn I 539.47 nm	2.86	2.68
Fe I 539.52 nm	2.04	1.87

Table A.4: Correlation coefficients for line parameters.

	before 1993		after 1993		total	
line	EW	CD	EW	CD	EW	CD
Fe I 539.32 nm	-0.09	0.19	-0.03	0.28	-0.39	0.91
Mn I 539.47 nm	0.86	0.81	0.70	0.79	0.94	0.96
Fe I 539.52 nm	0.34	0.19	0.31	0.14	0.88	0.93

A.3.3 Time series comparison

Figure A.3 shows the whole observed spectral range, obtained during two representative, 'quiet' days in the period before and after the change of grating. The disk-averaged FTS atlas (Neckel 1999) is overplotted, so that the change of the line profiles due to the grating change is evident. The central depths of all three lines are noticeably smaller before the grating change. The remaining difference between the atlas and observations taken after the grating is changed is due to the continuum normalization. Crosses mark the spectral ranges used for EW calculation. They are chosen such that the calculated EW match the EW observed in periods of quiet Sun after 1998. They are kept unchanged for the whole time interval modelled.

Observations taken during the days with the lowest solar activity, in the period before the change of grating (May 1986), are used for finding μ_{cut}. Comparison of the synthesized and the observed equivalent widths gave a value of 0.7 for μ_{cut}. For the period after the change of the grating we set $\mu_{cut} = 0$.

All synthesized profiles are then convolved with Gaussian profiles so that the instrumental broadening, broadening due to rotation and convective velocity fields are taken into account. These effects are thus approximated by a macroturbulence velocity, in addition of the microturbulence, which is employed unchanged from the values deduced in Sect. A.3.2. The broadenings applied to the line profiles were adjusted for each line separately, in order to reproduce the observed line central depths taken at low solar activity. The resulting Gaussian halfwidths are given in Table A.3. The line broadening were determined separately for the periods before and after the grating change, with values for the latter period being smaller. Several factors can play a role here. Firstly, the change of grating and set-up produces a change of the instrumental broadening. Secondly, by excluding the outer parts of the disk, the influence of the parts of the solar disk that produce more shifted line profiles due to the rotation is changed. Thirdly, prior to the grating change less of the regions close to the limb, which experience larger broadening due to

convection, were sampled. Obviously this effect is smaller than the other two. As a result of the superposition of these effects, the lines show on average a 20% larger broadening before 1993 (implying a roughly 10% higher broadening velocity). Finally, errors introduced into the disk-averaged profiles due to the simplicity of our modelling, cannot be ruled out, but cannot be estimated either. The LTE assumption also introduces errors.

Figure A.4 shows the observed and modelled change of the equivalent widths and central depths of the 3 lines over nearly 3 solar cycles. Vertical lines enclose the period during which the set-up of the telescope was frequently changed. The modelled values of the Fe I 539.52 nm line equivalent widths were systematically lower because of the small blend in its vicinity (see Fig. A.3), so we corrected them by adding a constant of 0.7 *m*Å.

The most conspicuous thing visible in Fig. A.4 is that the shift introduced by the change in the grating is relatively well modelled by the simple technique that we have applied. With a single free parameter μ_{cut}, we were able to produce the offset in 3 parameters, the EWs of the three lines.

Another feature in Fig. A.4 is the larger observed variability of the Mn I line than the Fe I lines. The variability of the Mn I 539.47 nm line is well reproduced, showing correct magnitude of the dips of both EW and CD during periods of high activity. The modelled EW and CD of the weak Fe I 539.52 nm line show only a weak change over the solar cycle and match the observations relatively well. The modelled variations are smaller than the scatter of the data. The strong Fe I line, on the other hand, shows significantly higher modelled change then is observed. This could be a consequence of the LTE assumption that we have made, which couples the source function to the temperature. Due to the greater formation height of this line (see Table A.2), it samples a considerably larger temperature difference between the quiet Sun and the facular model atmosphere (of around 500 K). In LTE this largely compensates for the relative temperature insensitivity of this line. The overestimate of the Fe I 539.32 nm line variability suggests that one of the assumptions made by the model is not met. Given the strength of the line and its high formation height, the departures from LTE might be the main cause.

Table A.4 contains correlation coefficients between observed and computed EW and CD of each of the three lines. Correlation coefficient are given for the periods before and after the grating change and also for the whole period of the observations, but always excluding the interval September 1992 - September 1998. In total, observations and simulations overlap for only 293 days, 184 and 109 days before and after the change of grating, respectively. The values for the Fe lines are significantly lower than for the Mn line. In the case of the weak Fe line, this is mainly a consequence of the scatter in the observational values. In the case of the strong Fe line, as mentioned before, the modelling fails to describe the temporal variations of the line properly. All three lines show better correlation with observations taken before 1992 than after. One reason is that the observational values obtained after 1993 have intrinsically larger scattering (Livingston et al. 2007). The lower correlation coefficient values for equivalent width, evident for all the lines, may be a consequence of the higher error in EW data due to nonuniformity in the gratings scan (Livingston & Wallace 1987). The values for the total period from 1979 till 2003, also given in the table, are significantly higher as a consequence of fitting the jump in EW and CD by employing suitable values for μ_{cut} and broadenings. Only for Fe I 539.32 nm line, whose CD displays practically no jump, the correlation coefficient is smaller and even negative. The correlation coefficients for the 1979-2003 period basically

confirm that the model successfully reproduces the influence of the grating change.

A.4 Conclusions

We model the change of the disk-integrated Mn I 539.47 nm line and two neighboring Fe I lines, from 1979 to 2004 by using the SATIRE model. This model has so far reproduced variations of total and spectral irradiance on time scales of days to multiple solar cycles. However, it has never been tested on individual spectral lines. Such a test is of particular interest because of the evidence that spectral lines are the dominant contributors to total solar irradiance variations over the solar cycle (Mitchell & Livingston 1991, Unruh et al. 1999). The reconstructed time series of line central depth and equivalent width agree quite well with the corresponding parameters of the Mn I 539.47 nm line and of the weak Fe I 539.52 nm line, but overestimates the variations of the strong Fe I 539.32 nm line profile, in particular in equivalent width. Reproducing the large solar cycle variation of the Mn I line with the SATIRE model in the present form (the single free parameter determined by Wenzler et al. (2006) from reproducing the TSI composite of Fröhlich (2006) is employed unchanged here) is a success for the model and strengthens the assumption underlying it, namely that TSI and SSI changes (in the optical wavelengths range) due to the magnetic field evolution at the solar surface. Our findings also imply that SATIRE might overestimate the solar cycle change in case of stronger lines that are formed higher up, which could explain why the SATIRE model reconstruction shows higher variability with respect to the SORCE/SIM measurements (Unruh et al. 2008) in some spectral ranges.

We found a high correlation and a good agreement of the magnitude of solar cycle variations between the observed and reconstructed change of the Mn I line parameters. This implies that the solar cycle variations of the line *can* be modelled by taking into account just changes of the surface distribution of the solar magnetic features. Since the solar disk coverage by faculae increases from the minimum to the maximum of the solar cycle, the disk integrated line, in the 'Sun-as-a-star' spectrum, becomes weaker during the solar cycle maximum. This explains why this manganese line mimics the behavior of Ca II K and Mg II k lines which are well known plage/faculae indicators. The influence of sunspots is negligible. No additional temperature change in the quiet Sun component is necessary. The optical pumping hypothesis is thus not required. Although energetic transfer between Mn I and Mg II might be present, it does not appear to be significant for the cyclic change of the Mn I 539.47 nm line.

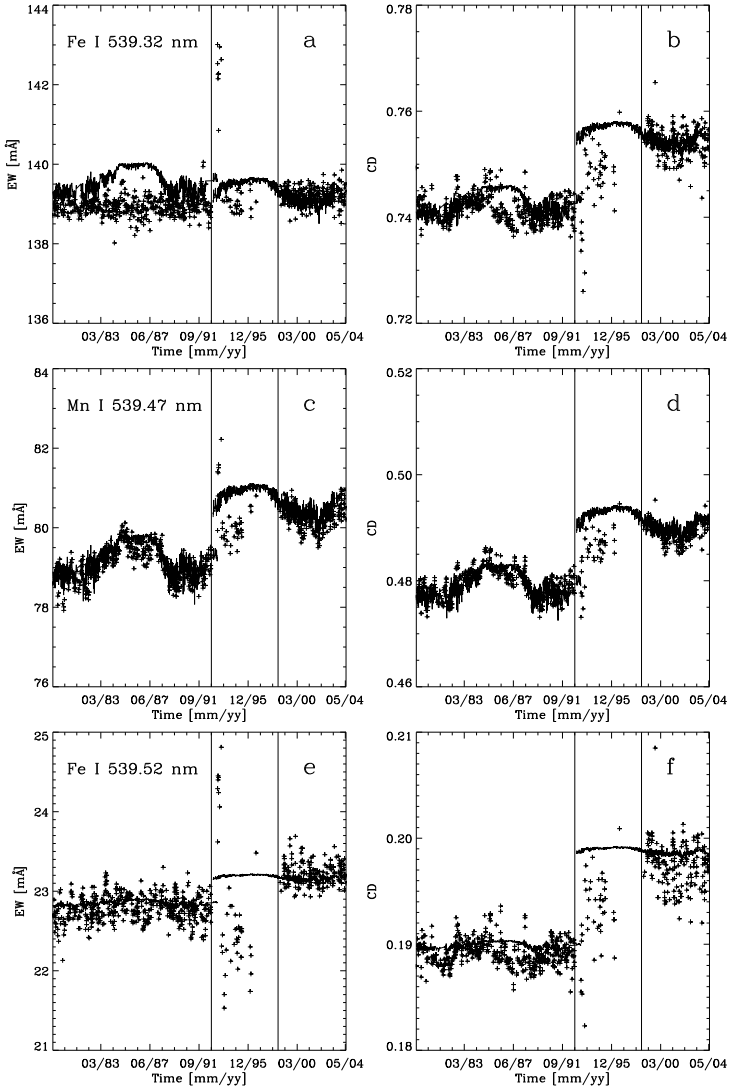

Figure A.4: Equivalent widths (left) and central depths (right) of the Fe I 539.32 nm (top), Mn I 539.47 nm (middle) and Fe I 539.52 nm line (bottom) extracted from KPNO observations (crosses) and calculated using our model (solid line). Experimental period is bounded by vertical lines. Modelled EW values for Fe I 539.52 nm line are shifted for 0.7 mÅ.

Bibliography

Altrock, R. C. 1976, Sol. Phys., 47, 517

Asensio Ramos, A., Martínez González, M. J., López Ariste, A., Trujillo Bueno, J., & Collados, M. 2007, ApJ, 659, 829

Asplund, M., Ludwig, H.-G., Nordlund, Å., & Stein, R. F. 2000, A&A, 359, 669

Archontis, V., Moreno-Insertis, F., Galsgaard, K., & Hood, A. W. 2005, ApJ, 635, 1299

Auer, L. H., House, L. L., & Heasley, J. N. 1977, Sol. Phys., 55, 47

Auer, L. H., & Heasley, J. N. 1978, A&A, 64, 67

Aulanier, G., Pariat, E., Démoulin, P., & Devore, C. R. 2006, Sol. Phys., 238, 347

Bahng, J., & Schwarzschild, M. 1961, ApJ, 134, 337

Balthasar, H. 1988, A&AS, 72, 473

Barklem, P. S., & O'Mara, B. J. 1997, MNRAS, 290, 102

Barklem, P. S., O'Mara, B. J., & Ross, J. E. 1998, MNRAS, 296, 1057

Batchelor, G. K. 1950, Proceedings of the Royal Society of London. Series A, Mathematical and Physical Sciences, 201, 405

Beck, C., Schmidt, W., Rezaei, R., & Rammacher, W. 2008, A&A, 479, 213

Bello González, N., Okunev, O., & Kneer, F. 2008, A&A, 490, L23

Bellot Rubio, L. R., & Collados, M. 2003, A&A, 406, 357

Bellot Rubio, L. R., & Beck, C. 2005, ApJ, 626, L125

Bellot Rubio, L. R., Ruiz Cobo, B., & Collados, M. 1998, ApJ, 506, 805

Bellot Rubio, L. R., Rodríguez Hidalgo, I., Collados, M., Khomenko, E., & Ruiz Cobo, B. 2001, ApJ, 560, 1010

Bercik, D. J., Nordlund, A., & Stein, R. F. 2003, GONG+ 2002. Local and Global Helioseismology: the Present and Future, 517, 201

Berdyugina, S. V., & Fluri, D. M. 2004, A&A, 417, 775

Berdyugina, S. V., Frutiger, C., Solanki, S. K., & Livingstone, W. 2000, A&A, 364, L101

Bergemann, M., & Gehren, T. 2007, A&A, 473, 291

Berger, T. E., & Title, A. M. 2001, ApJ, 553, 449

Berger, T. E., Loefdahl, M. G., Shine, R. S., & Title, A. M. 1998, ApJ, 495, 973

Bonet, J. A., Márquez, I., Sánchez Almeida, J., Cabello, I., & Domingo, V. 2008, ApJ, 687, L131

Boreman, G. D. 2001, Modulation Transfer Function in Optical and Electro-Optical Systems (Bellingham (SPIE))

Borrero, J. M., Solanki, S. K., Lagg, A., Socas-Navarro, H., & Lites, B. 2006, A&A, 450, 383

Brault, J. W., & Neckel, H. 1987, Spectral Atlas of Solar Absolute Diskaveraged and Disk-Center Intensity from 3290 to 12510 Å, ftp://ftp.hs.unihamburg.de/pub/outgoing/FTS-Atlas

Brault, J. W., Slaughter, C. D., Pierce, A. K., & Aikens, R. S. 1971, Sol. Phys., 18, 366

Briand, C., & Solanki, S. K. 1995, A&A, 299, 596

Brodzinski, T., Kronfeldt, H.-D., Kropp, J.-R., & Winkler, R. 1987, Zeitschrift fur Physik D Atoms Molecules Clusters, 7, 161

Bruls, J. H. M. J., & Solanki, S. K. 1993, A&A, 273, 293

Cameron, R., Vögler, A., & Schüssler, M. 2007, IAU Symposium, 239, 475

Carlsson, M. 1986, Uppsala Astronomical Observatory Reports, 33

Carlsson, M., & Stein, R. F. 1997, ApJ, 481, 500

Carlsson, M., Stein, R. F., Nordlund, Å., & Scharmer, G. B. 2004, ApJ, 610, L137

Cattaneo, F. 1999, ApJ, 515, L39

Cattaneo, F., Emonet, T., & Weiss, N. 2003, ApJ, 588, 1183

Cauzzi, G., et al. 2008, A&A, 480, 515

Centeno, R., et al. 2007, ApJ, 666, L137

Cheung, C.M.M. 2006, PhD Thesis, University of Göttingen, Germany, http://www.solarsystem-school.de/alumni/cheung.pdf

Cheung, M. C. M., Schüssler, M., Tarbell, T. D., & Title, A. M. 2008, ApJ, 687, 1373

Cheung, M. C. M., Schüssler, M., & Moreno-Insertis, F. 2007, A&A, 467, 703

Choudhuri, A. R. 1998, The physics of fluids and plasmas : an introduction for astrophysicists / Arnab Rai Choudhuri. New York : Cambridge University Press, 1998. QB466.F58 C46 1998

Cirtain, J. W., et al. 2007, Science, 318, 1580

Condon, E. U. & Shortley, G. H. 1963, The Theory of Atomic Spectra, University Press, Cambridge, p. 242

Culhane, J. L., et al. 2006, Proceedings of the SPIE, 6266, 62660T

Danilovic, S. & Vince, I. 2005, Mem. Soc. Astron. Ital., 76, 949

Danilovic, S., Vince, I., Vitas, N., & Jovanovic, P. 2005, Serbian Astronomical Journal, 170, 79

Danilovic, S., Gandorfer, A., Lagg, A., Schüssler, M., Solanki, S. K., Vögler, A., Katsukawa, Y., & Tsuneta, S. 2008, A&A, 484, L17

Davis, S. J., Wright, J. J., & Balling, L. C. 1971, PhysRev A, 3, 1220

de La Cruz Rodriguez, J., & van Noort, M. 2008, 12th European Solar Physics Meeting, Freiburg, Germany, held September, 8-12, 2008. Online at http://espm.kis.uni-freiburg.de/, p.2.77, 12, 2

del Toro Iniesta, J. C. 2003, Introduction to Spectropolarimetry, by Jose Carlos del Toro Iniesta, pp. 244. ISBN 0521818273. Cambridge, UK: Cambridge University Press

de Wijn, A. G., Stenflo, J. O., Solanki, S. K., & Tsuneta, S. 2009, Space Science Reviews, 144, 275

Deubner, F. L., & Mattig, W. 1975, A&A, 45, 167

Domínguez Cerdeña, I., Sánchez Almeida, J., & Kneer, F. 2003, A&A, 407, 741

Doyle, J. G., Jevremovic, D., Short, C. I., Hauschildt, P. H., Livingston, W., & Vince I. 2001, A&A, 369, L13

Dunn, R. B., & Zirker, J. B. 1973, SoPh., 33, 281

Durrant, C. J., Mattig, W., Nesis, A., & Schmidt, W. 1983, A&A, 123, 319

Edmonds, F. N., Jr., & Hinkle, K. H. 1977, Sol. Phys., 51, 273

Elste, G. 1986, Sol. Phys., 107, 47

Elste, G., & Teske, R. G. 1978, Sol. Phys., 59, 275

Emonet, T., & Cattaneo, F. 2001, ApJ, 560, L197

Fligge, M., Solanki, S. K., & Unruh, Y. C. 2000, A&A, 353, 380

Fontenla, J., White, O. R., Fox, P. A., Avrett, E. H., & Kurucz, R. L. 1999, ApJ, 518, 480

Fröhlich, C. 2006, Space Science Reviews, 125, 53

Fröhlich, C., et al. 1995, Sol. Phys., 162, 101

Frutiger, C., & Solanki, S. K. 2001, A&A, 369, 646

Frutiger, C., Solanki, S. K., Fligge, M., & Bruls, J. H. M. J. 2000, A&A, 358, 1109

Frutiger, C., Solanki, S. K., & Mathys, G. 2005, A&A, 444, 549

Gandorfer, A. M., Solanki, S. K., Schüssler, M., Curdt, W., Lites, B. W., Martínez Pillet, V., Schmidt, W., & Title, A. M. 2004, Edited by Oschmann, Jacobus M., Jr. Proceedings of the SPIE, 5489, 732

Golub, L., et al. 2007, Sol. Phys., 243, 63

Gray, D. F., & Livingston, W. C. 1997, ApJ, 474, 802

Grossmann-Doerth, U., Larsson, B., & Solanki, S. K. 1988, A&A, 204, 266

Grossmann-Doerth, U., Schuessler, M., & Steiner, O. 1998, A&A, 337, 928

Grossmann-Doerth, U., Schüssler, M., Sigwarth, M., & Steiner, O. 2000, A&A, 357, 351

Guglielmino, S. L., Zuccarello, F., Romano, P., & Bellot Rubio, L. R. 2008, ApJ, 688, L111

Gurtovenko, E. A. & Kostyk, R. I. 1989, Fraunhofer Spectrum and System of Solar Oscillator Strengths, Naukova dumka, Kiev

Hagenaar, H. J. 2001, ApJ, 555, 448

Harvey, K. L. 1993, Ph.D. Thesis, Utrecht University

Harvey, J. W., Branston, D., Henney, C. J., & Keller, C. U. 2007, ApJ, 659, L177

Holweger, H., Gehlsen, M., & Ruland, F. 1978, A&A, 70, 537

Ishikawa, R., & Tsuneta, S. 2009, A&A, 495, 607

Ishikawa, R., et al. 2007, A&A, 472, 911

Ishikawa, R., et al. 2008, A&A, 481, L25

Ichimoto, K., et al. 2008, Sol. Phys., 249, 233

Illing, R. M. E., Landman, D. A., & Mickey, D. L. 1975, A&A, 41, 183

Innes, D. E., Inhester, B., Axford, W. I., & Willhelm, K. 1997, Nature, 386, 811

Innes, D. E., Genetelli, A., Attie, R., & Potts, H. E. 2009, A&A, 495, 319

Innes, D. E., Inhester, B., Axford, W. I., & Willhelm, K. 1997, Nature, 386, 811

Jeong, J., & Hussain, F. 1995, Journal of Fluid Mechanics, 285, 69

Keller, C. U., Schüssler, M., Vögler, A., & Zakharov, V. 2004, ApJ, 607, L59

Khomenko, E., & Collados, M. 2007, ApJ, 659, 1726

Khomenko, E. V., Collados, M., Solanki, S. K., Lagg, A., & Trujillo Bueno, J. 2003, A&A, 408, 1115

Khomenko, E. V., Martínez González, M. J., Collados, M., Vögler, A., Solanki, S. K., Ruiz Cobo, B., & Beck, C. 2005, A&A, 436, L27

Khomenko, E. V., Shelyag, S., Solanki, S. K., Vögler, A. 2005, A&A, 442, 1059

Kosugi, T., et al. 2007, Sol. Phys., 243, 3

Krivova, N. A., Solanki, S. K., Fligge, M., & Unruh, Y. C. 2003, A&A, 399, L1

Krivova, N. A., Solanki, S. K., & Floyd, L. 2006, A&A, 452, 631

Kupka, F., Piskunov, N., Ryabchikova, T. A., Stempels, H. C., & Weiss, W. W. 1999, A&AS, 138, 119

Landi Degl'Innocenti, E. 1992, in Solar Observations: Techniques and Interpretation, ed. F. Sanchez, M. Collados, & M. Vazquez, Cambridge: Cambridge University Press, 73

Langangen, Ø., Carlsson, M., Rouppe van der Voort, L., & Stein, R. F. 2007, ApJ, 655, 615

Leenaarts, J., & Wedemeyer-Böhm, S. 2005, A&A, 431, 687

Levy, M. 1971, A&A, 14, 15

Lin, H. 1995, ApJ, 446, 421

Lin, H., & Rimmele, T. 1999, ApJ, 514, 448

Lites, B. W. 2002, ApJ, 573, 431

Lites, B. W., Rutten, R. J., & Berger, T. E. 1999, ApJ, 517, 1013

Lites, B. W., Elmore, D. F., & Streander, K. V. 2001, in: ASP conf. ser., Vol 236, Advanced Solar Polarimetry – Theory, Observation, and Instrumentation, ed. M. Sigwarth, 33

Lites, B. W., et al. 2008, ApJ, 672, 1237

Livingston, W., & Harvey, J. 1971, Solar Magnetic Fields, IAU Symposium no. 43, 1970, ed. Robert Howard., 51

Livingston W. 1992, in Proceedings of the Workshop on the Solar Electromagnetic Radiation Study for Solar Cycle 22 (ed. R.F. Donnelly), 11

Livingston, W. & Wallace, L. 1987, ApJ, 314, 808

Livingston, W., Wallace, L., White, O. R., & Giampapa, M. S. 2007, ApJ, 657, 1137

López Ariste, A., Tomczyk, S., & Casini, R. 2002, ApJ, 580, 519

Madjarska, M. S., Doyle, J. G., & van Driel-Gesztelyi, L. 2004, ApJ, 603, L57

Magain, P. 1986, A&A, 163, 135

Malanushenko, O., Jones, H. P., & Livingston, W. 2004, Multi-Wavelength Investigations of Solar Activity, 223, 645

Martin, S. F. 1988, Sol. Phys., 117, 243

Martínez González, M. J., Collados, M., & Ruiz Cobo, B. 2006, A&A, 456, 1159

Martínez González, M. J., Collados, M., Ruiz Cobo, B., & Solanki, S. K. 2007, A&A, 469, L39

Martínez González, M. J., Collados, M., Ruiz Cobo, B., & Beck, C. 2008, A&A, 477, 953

Mathew, S. K., et al. 2003, A&A, 410, 695

Mitchell, W. E., Jr., & Livingston, W. C. 1991, ApJ, 372, 336

Moreno-Insertis, F., Galsgaard, K., & Ugarte-Urra, I. 2008, ApJ, 673, L211

Muller, R. 1983, Sol. Phys., 85, 113

Muller, R., & Roudier, T. 1992, Sol. Phys., 141, 27

Nagata, S., et al. 2008, ApJl, 677, L145

Neckel H. 1999, Sol. Phys., 184, 421

Nordlund, A. 1982, A&A, 107, 1

Nordlund, A. 1983, Solar and Stellar Magnetic Fields: Origins and Coronal Effects, 102, 79

Nordlund, A. 1984, Small-Scale Dynamical Processes in Quiet Stellar Atmospheres, 174

Nordlund, Å. 1986, Small Scale Magnetic Flux Concentrations in the Solar Photosphere, 83

Orozco Suárez, D., Bellot Rubio, L. R., & del Toro Iniesta, J. C. 2007, ApJ, 662, L31

Orozco Suárez, D., et al. 2007, ApJ, 670, L61

Orozco Suárez, D., et al. 2007, PASJ, 59, 837

Orozco Suárez, D., Bellot Rubio, L. R., del Toro Iniesta, J. C., & Tsuneta, S. 2008, A&A, 481, L33

Ossendrijver, M. 2003, A&AR, 11, 287

Parker, E. N. 1963, ApJ, 138, 552

Parker, E. N. 1975, Sol. Phys., 40, 291

Parker, E. N. 1978, ApJ, 221, 368

Parnell, C. E., Haynes, A. L., & Galsgaard, K. 2008, ApJ, 675, 1656

Penza, V., Pietropaolo, E., & Livingston, W. 2006, A&A, 454, 349

Petrovay, K., & Szakaly, G. 1993, A&A, 274, 543

Pietarila, A., Socas-Navarro, H., & Bogdan, T. 2007, ApJ, 663, 1386

Pietarila, J. G., Danilovic, S., & Schüssler, M. 2008, 12th European Solar Physics Meeting, Freiburg, Germany, held September, 8-12, 2008. Online at http://espm.kis.uni-freiburg.de/, p.3.13, 12, 3

Pietarila Graham, J., Danilovic, S., & Schüssler, M. 2009, ApJ, 693, 1728

Piskunov, N. E., Kupka, F., Ryabchikova, T. A., Weiss, W. W., & Jeffery, C. S. 1995, A&AS, 112, 525

Ploner, S. R. O., Schüssler, M., Solanki, S. K., & Gadun, A. S. 2001, Advanced Solar Polarimetry – Theory, Observation, and Instrumentation, 236, 363

Ploner, S. R. O., Schussler, M., Solanki, S. K., Sheminova, V. A., Gadun, A. S., & Frutiger, C. 2001, Advanced Solar Polarimetry – Theory, Observation, and Instrumentation, 236, 371

Pravdyuk, L. M., Karpinskij, V. N., & Andrejko, A. V. 1974, Solnechnye Dann. Bull. Akad. Nauk SSSR, 1974, 70

Press, W. H., Teukolsky, S. A., Vetterling, W. T., & Flannery, B. P. 1992, Cambridge: University Press, 1992, 2nd ed.

Rachkovsky, D. N. 1962, Izv. Krymskoi Astrofiz. Obs., 27, 148

Rachkovsky, D. N. 1967, Izv. Krymskoi Astrofiz. Obs., 37, 56

Rees, D. E., Durrant, C. J., & Murphy, G. A. 1989, ApJ, 339, 1093

Régnier, S., Parnell, C. E., & Haynes, A. L. 2008, A&A, 484, L47

Rempel, M., Schüssler, M., & Knölker, M. 2009, ApJ, 691, 640

Rezaei, R., Schlichenmaier, R., Schmidt, W., & Steiner, O. 2007, A&A, 469, L9

Rezaei, R., Schlichenmaier, R., Schmidt, W., & Beck, C. 2009, Astronomical Society of the Pacific Conference Series, 405, 195

Rezaei, R., Schlichenmaier, R., Beck, C. A. R., Bruls, J. H. M. J., & Schmidt, W. 2007, A&A, 466, 1131

Riethmüller, T. L., Solanki, S. K., & Lagg, A. 2008, ApJ, 678, L157

Rodriguez Hidalgo, I., Collados, M., & Vazquez, M. 1994, A&A, 283, 263

Roudier, T., Malherbe, J. M., November, L., Vigneau, J., Coupinot, G., Lafon, M., & Muller, R. 1997, A&A, 320, 605

Rybák, J., Kučera, A., Wöhl, H., Wedemeyer-Böhm, S., & Steiner, O. 2006, Solar MHD Theory and Observations: A High Spatial Resolution Perspective , 354, 77

Rüedi, I., Solanki, S. K., Livingston, W., & Stenflo, J. O. 1992, A&A, 263, 323

Sainz Dalda, A., & López Ariste, A. 2007, A&A, 469, 721

Sánchez Almeida, J. 2008, Ap&SS, 156

Sanchez Almeida, J. 1997, A&A, 324, 763

Sánchez Almeida, J., & Lites, B. W. 2000, ApJ, 532, 1215

Sánchez Almeida, J., Emonet, T., & Cattaneo, F. 2003, ApJ, 585, 536

Sánchez Cuberes, M., Bonet, J. A., Vázquez, M., & Wittmann, A. D. 2000, ApJ, 538, 940

Scharmer, G. B., et al. 2008, ApJ, 689, L69

Schmidt, W., Deubner, F.-L., Mattig, W., & Mehltretter, J. P. 1979, A&A, 75, 223

Schüssler, M. 1990, Solar Photosphere: Structure, Convection, and Magnetic Fields, 138, 161

Schüssler, M., Vögler, A. 2006, ApJ, 641, L73

Schüssler, M., Vögler, A. 2008, A&A, 481, L5

Schüssler, M., Shelyag, S., Berdyugina, S., Vögler, A., & Solanki, S. K. 2003, ApJ, 597, L173

Shchukina, N., & Trujillo Bueno, J. 2001, ApJ, 550, 970

Shelyag S. 2004, PhD Thesis, University of Göttingen, Germany, http://www.solar-system-school.de/alumni/shelyag.pdf

Shelyag, S., Schüssler, M., Solanki, S. K., Berdyugina, S. V., Vögler, A. 2004, A&A, 427, 335

Shibata, K., et al. 2007, Science, 318, 1591

Shimizu, T., et al. 2008, ApJ, 680, 1467

Sigwarth, M. 2001, ApJ, 563, 1031

Sigwarth, M., Balasubramaniam, K. S., Knölker, M., & Schmidt, W. 1999, A&A, 349, 941

Simon, G. W., & Leighton, R. B. 1964, ApJ, 140, 1120

Socas-Navarro, H., & Manso Sainz, R. 2005, ApJ, 620, L71

Socas-Navarro, H., & Sánchez Almeida, J. 2002, ApJ, 565, 1323

Socas-Navarro, H., & Sánchez Almeida, J. 2003, ApJ, 593, 581

Solanki, S. K. 1986, A&A, 168, 311

Solanki, S. K. 1987, Ph.D. Thesis, ETH, Zürich

Solanki, S. K., & Pahlke, K. D. 1988, A&A, 201, 143

Solanki, S. K., & Bruls, J. H. M. J. 1994, A&A, 286, 269

Solanki, S. K., Krivova, N. A., & Wenzler, T. 2005, Advances in Space Research, 35, 376

Solanki, S. K., Inhester, B., & Schüssler, M. 2006, Reports on Progress in Physics, 69, 563

Spruit, H. C. 1976, Sol. Phys., 50, 269

Spruit, H. C., & Zweibel, E. G. 1979, Sol. Phys., 62, 15

Spruit, H. C., Title, A. M., & van Ballegooijen, A. A. 1987, Sol. Phys., 110, 115

Stein, R. F., & Nordlund, A. 1998, ApJ, 499, 914

Stein, R. F., & Nordlund, Å. 2000, Sol. Phys., 192, 91

Stein, R. F., & Nordlund, Å. 2006, ApJ, 642, 1246

Steiner, O. 1999, Third Advances in Solar Physics Euroconference: Magnetic Fields and Oscillations, 184, 38

Steiner, O. 2000, Sol. Phys., 196, 245

Steiner, O., Rezaei, R., Schaffenberger, W., & Wedemeyer-Böhm, S. 2008, ApJ, 680, L85

Stenflo, J. O., Keller, C. U., & Gandorfer, A. 1998, A&A, 329, 319

Suematsu, Y., et al. 2008, Sol. Phys., 249, 197

Thevenin, F. 1989, A&AS, 77, 137

Title, A. M., Tarbell, T. D., Topka, K. P., Ferguson, S. H., Shine, R. A., & SOUP Team 1989, ApJ, 336, 475

Tritschler, A., Uitenbroek, H., & Reardon, K. 2008, ApJ, 686, L45

Trujillo Bueno, J., Asensio Ramos, A., & Shchukina, N. 2006, Astronomical Society of the Pacific Conference Series, 358, 269

Trujillo Bueno, J., Shchukina, N., & Asensio Ramos, A. 2004, Nature, 430, 326

Tsuneta, S. 1996, ApJ, 456, L63

Tsuneta, S. 2008, 37th COSPAR Scientific Assembly, 37, 3234

Tsuneta, S., et al. 2008, Sol. Phys., 249, 167

Tsuneta, S., et al. 2008, ApJ, 688, 1374

Uitenbroek, H. 2001, ApJ, 557, 389

Uitenbroek, H., Balasubramaniam, K. S., & Tritschler, A. 2006, ApJ, 645, 776

Unno, W. 1956, PASJ, 8, 108

Unruh, Y. C., Solanki, S. K., & Fligge, M. 1999, A&A, 345, 635

Unruh, Y. C., Krivova, N. A., Solanki, S. K., Harder, J. W., & Kopp, G. 2008, A&A, 486, 311

Vince, I., Vince, O., Ludmány, A., & Andriyenko, O. 2005, Sol. Phys., 229, 273

Vince, I., Gopasyuk, O., Gopasyuk, S., & Vince, O. 2005, Serbian Astronomical Journal, 170, 115

Vitas, N. 2005, Mem. Soc. Astron. Ital. Suppl., 7, 164

Vitas, N., & Vince, I. 2005, Memorie della Societa Astronomica Italiana, 76, 1064

Vitas, N., & Vince, I. 2007, The Physics of Chromospheric Plasmas, 368, 543

Vitas, N., Viticchiè, B., Rutten, R. J., Vögler, A. 2009, A&A, 499, 301

Vögler, A. 2003, PhD Thesis, University of Göttingen, Germany, http://www.solar-system-school.de/alumni/voegler.pdf

Vögler, A. 2004, A&A, 421, 755

Vögler, A., & Schüssler, M. 2007, A&A, 465, L43

Vögler, A., Bruls, J. H. M. J., & Schüssler, M. 2004, A&A, 421, 741

Vögler, A., Shelyag, S., Schüssler, M., Cattaneo, F., Emonet, T., & Linde, T. 2005, A&A, 429, 335

Wallace, L., Hinkle, K., & Livingston, W. 2007, An Atlas of the Spectrum of the Solar Photosphere from 13,500 to 33,980 cm^{-1} (2942 to 7405 Å), by L. Wallace, K. Hinkle and W. Livingston. Published in 2007.

Webb, A. R., & Roberts, B. 1978, Sol. Phys., 59, 249

Wedemeyer-Böhm, S. 2007, IAU Symposium, 239, 52

Wedemeyer-Böhm, S., & Rouppe van der Voort, L. 2009, A&A, 503, 225

Weiss, N. O. 1966, Royal Society of London Proceedings Series A, 293, 310

Wenzler, T., Solanki, S. K., Krivova, N. A., & Fluri, D. M. 2004, A&A, 427, 1031

Wenzler, T., Solanki, S. K., & Krivova, N. A. 2005, A&A, 432, 1057

Wenzler, T., Solanki, S. K., Krivova, N. A., & Fröhlich, C. 2006, A&A, 460, 583

Wilmot-Smith, A. L., & de Moortel, I. 2007, A&A, 473, 615

Wittmann, A. 1981, A&A, 99, 90

Wittmann, A., & Mehltretter, J. P. 1977, A&A, 61, 75

Zwaan, C. 1987, ARA&A, 25, 83